GEOCHEMISTRY AND CRYSTAL STRUCTURE OF RECRYSTALLIZED DOLOMITES

By

GEORGINA LUKOCZKI

Master of Science in Geology/Geography
University of Szeged
Szeged, Hungary
2009

Submitted to the Faculty of the Arts and Sciences
Graduate College of the Arts and Sciences
Oklahoma State University
in partial fulfillment of
the requirements for
the Degree of
DOCTOR OF PHILOSOPHY
July, 2019

GEOCHEMISTRY AND CRYSTAL STRUCTURE OF RECRYSTALLIZED DOLOMITES

Dissertation Approved:

Jay M. Gregg, Ph.D., Chair

Dissertation Adviser

Michael G. Grammer, Ph.D.

James O. Puckette, Ph.D.

János Haas, Ph.D.

Pankaj Sarin, Ph.D.

ACKNOWLEDGEMENTS

I would like to express my deepest gratitude to my committee chair and advisor, Dr. Jay Gregg for accepting me as his student and for his continuous support throughout my time at Oklahoma State University. Special thanks to my committee member, Dr. János Haas, who has supported me and this research from the earliest stages starting in Hungary. I am deeply grateful for the assistance of my external committee member, Dr. Pankaj Sarin, who fundamentally contributed to this research with his suggestion to use synchrotron X-ray and neutron diffraction to study the crystal structure of recrystallized dolomites, and his assistance with writing successful proposal to collect such data at national laboratories. I thank my committee members, Dr. Michael Grammer and Dr. James Puckette for their continuous support.

I am deeply grateful for the help and support of Dr. Hans Machel. His relentless constructive criticism made me a better researcher. I am indebted to Dr. Cédric John, who welcomed me in his clumped isotope laboratory at Imperial College, London, in the summers of 2017 and 2018. The data collected in his lab proved to be a vital component of this research. Simon Davis and members of Dr. John's research group are acknowledged for their help teaching me how to run my samples, making sure I always had liquid nitrogen available, and for their help running some of my samples on the IBEX. I thank Dr. Sándor Kele for his help with running stable isotope analysis on my samples when I did not have access to any analytical facilities. Dr. Tamás Budai and Dr. Gyula Konrád have always been available to help me with their in-depth knowledge of the Mecsek Mts. and the Villány Hills. I am grateful for their help with field work and for the discussions about regional geology. I greatly appreciate the help of Dr. David Bish and Dan Lowry with the Rietveld refinements.

Use of the Advanced Photon Source at Argonne National Laboratory was supported by the U. S. Department of Energy, Office of Science, Office of Basic Energy Sciences, under Contract No. DE-AC02-06CH11357. I thank Dr. Saul Lapidus for his help with the proposal and analysis. I acknowledge the support of the National Institute of Standards and Technology, U.S. Department of Commerce, in providing the neutron research facilities used in this work. Dr. Craig Brown is acknowledged for his help with the proposal and analysis.

I am grateful for all members of the Boone Pickens School of Geology, faculty, staff and fellow students who made me feel welcome at OSU. Dr. Tao Wu's help in the stable isotope laboratory, Alejandra Torres' and Maria Reistroffer's help with ion milling my samples is much appreciated. I am deeply grateful for Dr. Natascha Riedinger who welcomed me in her lab and has supported me throughout my time at OSU.

This work was supported by the American Association of Petroleum Geologists Grants-in-Aid Program, the Geological Society of America Graduate Student Research Grant Program, the International Association of Sedimentologists Post-Graduate Grant Scheme, and the Hungarian Scientific Research Fund (OTKA K124313). I am grateful for the Davis, Skinner and Martin Families for their generous support. I benefited from fellowships they have graciously provided to the School of Geology.

Name: GEORGINA LUKOCZKI

Date of Degree: JULY, 2019

Title of Study: GEOCHEMISTRY AND CRYSTAL STRUCTURE OF
RECRYSTALLIZED DOLOMITES

Major Field: GEOLOGY

Abstract: Shallow marine to peritidal carbonates of the Triassic Csukma Formation in the Mecsek Mts. and Villány Hills of SW Hungary are made up of dolomites, limestones, and dolomitic limestones that show evidence of a complex diagenetic history. Integration of petrographic, conventional stable oxygen and carbon isotope, clumped isotope, and strontium isotope data with the paleogeography, paleoclimate, and burial history of the region revealed four major diagenetic stages in the Mecsek Mts. Stage 1: Reflux dolomitization of the peritidal carbonates during the Middle Triassic. Stage 2: Recrystallization of the reflux dolomites in intermediate burial setting. Stage 3: High-temperature, fault-controlled dolomitization and renewed recrystallization of the reflux dolomite during the Early Cretaceous by seawater drawn down and circulated through rift-related faults in a deep burial setting. Stage 4: Saddle dolomite cementation related to tectonic expulsion of basinal fluids during the Late Cretaceous and Cenozoic. Due to striking differences in the burial history of the Mecsek Mts. and Villány Hills, evidence of diagenetic phases resulting from deep burial and rift-related faulting, such as high-temperature dolomite recrystallization and considerable saddle dolomite cementation, are missing in the Villány Hills. Here dolomitization likely occurred penecontemporaneously via geothermal convection of normal to slightly modified seawater in a near-surface to shallow burial setting followed by partial recrystallization of the dolomites in an intermediate burial setting with low water to rock ratios.

Geochemical data and unit cell parameters obtained by Rietveld refinement of conventional and synchrotron X-ray and neutron diffraction data collected on recrystallized dolomites of the Csukma Formation suggest that recrystallization with high water to rock ratio versus recrystallization in low water to rock ratio may be reflected in the unit cell dimensions of recrystallized dolomites. Recrystallization processes with low water to rock ratio result in a noticeable trend between crystal size and unit cell parameters that cannot be explained by Ostwald ripening. In samples recrystallized with high water to rock ratios compositionally indistinguishable overgrowth cement on the matrix dolomite may have a significant effect on the overall unit cell dimensions determined from powder diffraction analyses. This study is the first to apply combined synchrotron X-ray diffraction and neutron diffraction to investigate crystal structural changes in sedimentary dolomites due to recrystallization in various diagenetic environments.

PUBLICATION DISSERTATION OPTION

This dissertation has been structured in three sections. An outline is presented here of the dissertation and introduces the scientific questions that were investigated in this research. This section also lists the three manuscripts resulting from this dissertation that are in various stages of the publication process.

Paper I: Multi-phase dolomitization and recrystallization of Middle Triassic shallow marine–peritidal carbonates from the Mecsek Mts. (SW Hungary), as inferred from petrography, carbon, oxygen, strontium and clumped isotope data. Marine and Petroleum Geology, 101, pp. 440–458. https://doi.org/10.1016/j.marpetgeo.2018.12.004.

Paper II: Early dolomitization and partial burial recrystallization: A case study of Middle Triassic peritidal dolomites in the Villány Hills (SW Hungary) using petrography, carbon, oxygen, strontium and clumped isotope data.

Paper III: Interpretation of Recrystallization Processes of Sedimentary Dolomites as Deduced from Crystal Structural and Geochemical Data.

SUMMARY OF PROBLEM

Dolomite is a common rock-forming mineral of both academic and industrial interest primarily due to the excellent hydrocarbon and potable water reservoir potential of dolomite rocks. Dolomites commonly recrystallize, which may alter their crystal structural, chemical, and reservoir properties (Mazzullo, 1992; Sun, 1995). A better understanding of recrystallization is needed to accurately interpret the genesis, alteration, and reservoir potential of dolomite rocks. Peritidal carbonates of the Middle Triassic Csukma Formation in the Mecsek Mountains and Villány Hills in southwestern Hungary show evidence of multi-phase dolomitization and recrystallization thus providing a suitable succession to study the formation and alteration of various dolomite types.

The central hypothesis of this study is that the geological environment of recrystallization controls the ultimate crystal structure and chemistry of dolomites. Detailed geochemical and diffraction data was collected to characterize recrystallized dolomites. The main objectives of the study are to discriminate and characterize local dolomitization and recrystallization events that affected the Csukma Formation in SW Hungary, and to determine how the geological environment of recrystallization affects the chemical and crystallographic characteristics of dolomites. To this end, a three-stage workflow was followed.

Stage 1: Petrographic and geochemical characterization

The geological environment, in which the dolomites formed or recrystallized, was interpreted based on detailed geochemical information (oxygen, carbon, and strontium isotopes; elemental composition), along with temperatures of formation or recrystallization obtained using clumped isotopes. The samples for geochemical analyses were selected to represent the variability in the petrographic characteristics of the Csukma Formation.

Stage 2: Crystallographic characterization

Diffraction data was collected and analyzed to examine the effect of recrystallization on the crystal structure of dolomites. Samples representing dolomites that formed and recrystallized in a range of geological environments were selected for crystallographic characterization. Conventional X-ray diffraction was used first to select the most suitable samples for high-resolution neutron and synchrotron X-ray diffraction analyses. All diffraction data was analyzed using the Rietveld method (Rietveld, 1969) to obtain high-precision crystal structural data to identify any subtle crystallographic variations that may be present due to differences in the geological environment of recrystallization.

Stage 3: Synthesis

The data collected during Stage 1 and Stage 2 of this research were combined to investigate systematic variations between crystallographic and geochemical characteristics to identify how the geological environment of recrystallization controls the crystal structure and chemistry of dolomites.

FUTURE DIRECTIONS

Application of the methodology of the current study on a large sample suite of dolomites formed and recrystallized in various diagenetic environments and in a wide range of geological ages is needed in order to obtain an in-depth understanding of how the environment of dolomitization and dolomite recrystallization controls the ultimate chemical and crystallographic properties of dolomites. The use of geochemical modeling to further assess the effect of diagenesis on the various geochemical and crystallographic parameters of dolomites would be beneficial to better understand the cause-and-effect relationships in dolomite recrystallization. Furthermore, comparing the results of high-resolution diffraction analysis with observations on the same samples with transmission electron microscopy is needed to better understand how the presence and nature of defective micro- and nanostructures (e.g., Reeder, 1992) affect the average crystal structure observed with diffraction analysis. Moreover, advanced X-ray methods, such as total scattering using the X-ray pair distribution function (e.g., Proffen et al., 2003), anomalous X-ray scattering (e.g., Waseda, 2002) and X-ray absorption spectroscopy (e.g., Yano and Yachandra, 2009) can be used to quantitatively characterize the long- and short-range structure and Ca-Mg ordering in dolomites. The ultimate goal of such research is to develop a generally applicable system of criteria to identify and characterize recrystallized dolomites.

REFERENCES

Mazzullo, S.J., 1992. Geochemical and neomorphic alteration of dolomite: A review. Carbonates and Evaporites, 7(1): 21-37.

Proffen, T., Billinge, S. J. L., Egami, T., and Louca, D., 2003, Structural Analysis of Complex Materials Using the Atomic Pair Distribution Function - A Practical Guide: Zeitschrift für Kristallographie, v. 218, no. 2, p. 132-43.

Reeder, R.J., 1992. Carbonates; growth and alteration microstructures. Reviews in Mineralogy and Geochemistry, 27(1): 380-424.

Rietveld, H., 1969. A profile refinement method for nuclear and magnetic structures. Journal of applied Crystallography, 2(2): 65-71.

Sun, S.Q., 1995. Dolomite reservoirs: porosity evolution and reservoir characteristics. AAPG bulletin, 79(2): 186-204.

Waseda, Y., 2002, Merits of anomalous X-ray scattering and its future prospects, Anomalous X-Ray Scattering for Materials Characterization: Atomic-Scale Structure Determination, Volume 179, p. 199-210.

Yano, J., and Yachandra, V. K., 2009, X-ray absorption spectroscopy: Photosynthesis Research, v. 102, no. 2-3, p. 241-254.

TABLE OF CONTENTS

Chapter Page

LIST OF TABLES

CHAPTER I

CHAPTER II

CHAPTER III

Table Page

LIST OF FIGURES

CHAPTER I

Figure 6: Petrographic features representing a variety in saddle dolomite cements as found across the studied sedimentary succession. The numbers indicate paragenetic sequence within a given sample and do not correlate across samples. **(a)** Saddle dolomite cement with inclusion-rich zones (sd1) or clear (sd2) overgrowth filling a vug in coarse crystalline planar-s to nonplanar-a matrix dolomite (md). Final cement in the pore is calcite (cal). Plane-polarized light. (Location GF-1) **(b)** CL image of (a). The first saddle dolomite (sd1) with dull, mottled CL is cross-cut (arrow) and overgrown by a later saddle dolomite phase (sd2) with duller CL. The calcite (cal) displays complex bright and dull orange CL zonation. **(c)** Saddle dolomite cement (sd) filling a vug in very fine crystalline matrix dolomite (md). **(d)** CL image of (c). The saddle dolomite cement displays bright red concentric CL zonation. The final dolomite phase is nonluminescent. (Location GF-1) **(e)** Fracture-filling saddle dolomite cement. (Location VP-2) **(f)** CL image of (e). The saddle dolomite cement displays simple concentric and oscillatory concentric zonation. Non-luminescent matrix dolomite (md) is overgrown by non-luminescent to bright red planar-c dolomite cement (cd). The first generation of saddle dolomite (sd1) shows bright red simple concentric zoning. The inclusion-rich zones, best visible in (e), have mottled CL appearance. The second generation of saddle dolomite (sd2) shows oscillatory zoning of mainly non- and minor red-growth bands, capped by a brightly luminescent inclusion-rich layer (yellow arrows). Sd3 shows zonation pattern similar to sd2 but with lower intensity. The final saddle dolomite cement (sd4) is non-luminescent. Small remaining pore space was filled by dull orange luminescing calcite (cal). **(g)** Fracture-filling saddle dolomite and fractured coarse crystalline, nonplanar-a dolomite matrix dolomite (md). (Location VA) **(h)** CL image of (g). The first phase of the saddle dolomite (sd1) is

LIST OF FIGURES

CHAPTER II

(arrows). Polished core slab. (Location MGY-1) **(b)** Very fine to medium crystalline planar-s dolomite with recognizable laminated sedimentary fabric. Plane-polarized light. (Location MGY-1) **(c)** Aphanocrystalline and very fine crystalline dolomite with well-preserved stromatolite fabric. Fenestral pores are filled (replaced?) by coarse crystalline, planar-s dolomite. Plane-polarized light. (Location MGY-1) **(d)** Same as in (c) in CL. The aphanocrystalline to very fine crystalline dolomite is bright red, whereas the dolomites filling the fenestral pores are very dull, brighter towards the center of larger pores where the dolomite displays simple concentric zonation (arrows). **(e)** Pisolitic dolomite made up of very fine crystalline dolomite with excellent fabric preservation. The pisolitic grains occur in sedimentary layers with peloidal–fenestral fabric. Fenestral pores are filled (replaced?) by coarse crystalline, planar-s dolomite. Plane-polarized light. (Location MGY-1) **(f)** Fine to medium crystalline planar-s dolomite with poorly preserved sedimentary fabric. The fine crystalline ghosts suggest ooid grainstone or packstone precursor. Plane-polarized light. (Location MK-3) **(g)** Very fine to medium crystalline dolomite with poorly preserved bioclastic packstone or wackestone fabric. Large bioclast was likely a green algae fragment (arrow). Plane-polarized light. (Location V-6) **(h)** Coarse crystalline, planar-e to planar-s dolomite with cloudy core–clear rim appearance. In the clear(er) rims, solid inclusions are arranged along mostly planar growth zones. Plane-polarized light. (Location MK-3) **(i)** Same as in (h) in CL. The cloudy cores display red mottled CL, whereas the rims are mostly non-luminescent with brighter orange zones and patches. **(j)** Very fine to fine crystalline planar-s dolomite with very poor fabric preservation. Stylolite seam (arrows) is barely discernible. Plane-polarized light. (Location MK-3) **(k)** Intraclastic–peloidal/pisolitic dolograinstone

LIST OF FIGURES

CHAPTER III

CHAPTER I

MULTI-PHASE DOLOMITIZATION AND RECRYSTALLIZATION OF MIDDLE TRIASSIC SHALLOW MARINE–PERITIDAL CARBONATES FROM THE MECSEK MTS. (SW HUNGARY), AS INFERRED FROM PETROGRAPHY, CARBON, OXYGEN, STRONTIUM AND CLUMPED ISOTOPE DATA

Abstract

Shallow marine to peritidal carbonates of the Triassic Csukma Formation in the Mecsek Mts. of SW Hungary are made up of dolomites, limestones and dolomitic limestones that show evidence of a complex diagenetic history. Integration of petrographic, conventional stable oxygen and carbon isotope, clumped isotope, and strontium isotope data with the paleogeography, paleoclimate, and burial history of the region revealed four major diagenetic stages. Stage 1: The peritidal carbonates were dolomitized penecontemporaneously during the Middle Triassic by refluxing evaporatively concentrated brines. Stage 2: Increasing burial during the Late Triassic–Jurassic resulted in recrystallization of the Kán Dolomite Member in an intermediate burial setting. Stage 3: During the Early Cretaceous seawater was drawn down and circulated through rift-related faults, causing renewed recrystallization of the Kán Dolomite Member as well as dolomitization of the Kozár Limestone Member and the underlying limestones in a deep burial setting, but only in the vicinity of the faults. Stage 4: During the Late Cretaceous and Cenozoic

thrusting resulted in tectonic expulsion of basinal fluids and precipitation of multiple saddle dolomite cement phases near the faults.

The results of this study imply that the clumped isotope method integrated with other geochemical data can successfully be applied to identify the nature and potential sources of extra-formational diagenetic fluids responsible for dolomitization and recrystallization. This study provides conclusive evidence for multi-phase dolomitization and dolomite recrystallization over several millions of years (Middle Triassic through Early Cretaceous) and several thousands of meters of burial in the Csukma Formation in SW Hungary. Furthermore, this study is the first to identify fault-controlled dolomitization by circulating Cretaceous seawater within Triassic carbonates of central Europe, further supporting the viability of the interpretation of dolomitization by seawater initially drawn down and then geothermally circulated through faults in extensional basins.

1.1. Introduction

Dolomite rocks (also known as dolostones) comprise a large portion of the world's hydrocarbon and potable water reservoirs and thus have been the focus of long-term research interest. Dolomitization, which is the process of calcite replacement by dolomite, occurs in a number of geological environments predominantly through the addition of magnesium (Mg^{2+}), introduced by aqueous fluids, to limestone in some form of advection (e.g., Machel, 2004). Most dolomites that formed in near-surface settings are metastable upon formation (commonly referred to as very high magnesium calcites (VHMC) or protodolomites; Machel 2004; Gregg et al. 2015), and transform into more stable dolomite via recrystallization or, albeit rarely, they persist as metastable phases over geological time (e.g., Land, 1980; Mazzullo, 1992; Gregg et al., 2015). During recrystallization the overall mineralogy of the rock does not change; however, a number of chemical, crystallographic and physical properties may be reset (cf. concept of significant vs. insignificant recrystallization; Machel, 1997). Therefore, the chemical and/or physical properties of recrystallized dolomites may no longer reflect the mechanism of dolomitization but represent the geological environment and/or process of recrystallization. Thus, not recognizing recrystallization may cause inaccurate genetic interpretation of dolomitization (Machel, 1997). The nature and extent of recrystallization is controlled by the geological evolution of the area; therefore, precise interpretation of the geological evolution of dolomite geobodies is crucial for reservoir characterization, since recrystallization may significantly alter the porosity and permeability of dolomites (Al-Aasm and Packard 2000; Sun, 1995; Machel, 2004).

Even though numerous case studies demonstrated recrystallization of dolomites of ages ranging from Paleozoic to Holocene, identifying the dolomitizing and recrystallizing fluids and processes remains challenging. Typically, initial dolomitization of peritidal carbonates is interpreted to have occurred via evaporatively concentrated seawater (e.g., Machel, 2004). In some cases, the initial reflux/sabhka dolomitization was interpreted to have been followed by recrystallization in meteoric or mixed meteoric–marine fluids (e.g., Spötl and Burns, 1991; Kupecz and Land, 1994). A second recrystallization event by warm/hot extra-formational fluids is often invoked to explain the current petrographic and/or geochemical signatures (e.g., Spötl and Burns, 1991; Montanez and Read, 1992; Kupecz and Land, 1994; Nader et al., 2004). Even though the dolomitizing capability of mixed meteoric–marine fluids has long been questioned (e.g., Hardie, 1987; Machel, 2004), a few authors have argued that initial partial dolomitization may occur with the aid of such fluids, and complete dolomitization of the investigated rock sequences was later achieved via interaction with warm basinal fluids that also recrystallized the pre-existing dolomites (e.g., Banner et al., 1988; Durocher and Al-Aasm, 1997). Basin-wide burial dolomitization of some Devonian carbonates of Western Canada was locally followed by recrystallization in hydrothermal fluids, also referred to as 'hydrothermal alteration' (e.g., Lonnee and Machel, 2006), related to tectonic expulsion (e.g., Machel et al., 1996) and/or to topographically driven flow (Qing and Mountjoy, 1994). On the other hand, recrystallization has also been identified to occur extremely early and under near-surface conditions. An example is a study of Holocene samples from Belize, which revealed that surface energy-driven recrystallization may occur within a few thousand years in the topmost meter of the sediment (Gregg et al., 1992).

Carbonate clumped isotope (Δ_{47}) thermometry (e.g., Ghosh et al., 2006; Eiler, 2007) is a novel method to investigate the nature and origin of diagenetic fluids. The calibration and limitations of the dolomite clumped isotope thermometer for diagenetic temperatures is now sufficiently well-established (see Bonifacie et al., 2017, and references therein). Comparing temperatures obtained from fluid inclusions and clumped isotopes supports the reliability of the dolomite clumped isotope thermometer (e.g., Millán et al., 2016; Came et al., 2017, Honlet et al., 2018), and over the past decade, an increasing number of studies have demonstrated the usefulness of this method in investigating dolomite diagenesis. A major advantage of this method is to be able to determine the temperature and oxygen isotope composition of the diagenetic fluids where fluid inclusion measurements are not feasible. Such is the case with very fine to fine crystalline dolomites (i.e., dolomicrites), low-temperature cements with single phase fluid inclusions, or where fluid inclusions are not present or their size is too small to observe phase changes. Successful applications of the clumped isotope thermometer include to determine the nature and origin of the dolomitizing (e.g., Ferry et al., 2011), or recrystallizing fluids (e.g., Sena et al., 2014; Loyd et al., 2015), and to reconstruct thermal and fluid flow histories (e.g., MacDonald et al., 2018; Mangenot et al., 2018). The method can provide especially useful insights when applied in combination with other methods (e.g., with U-Pb dating, Lawson et al., 2018).

Shallow marine–peritidal carbonates of the Csukma Formation in the Mecsek Mts. of SW Hungary (Figs. 1, 2) are made up of varied dolomites, limestones and dolomitic limestones, and show evidence of a complex diagenetic history. The peritidal inner ramp succession is completely dolomitized, whereas the extent of dolomitization of the middle ramp shoal deposits varies from none to complete. Even though the Csukma Formation has been characterized in basic sedimentological and stratigraphic studies (e.g., Török, 1998a; Haas et al., 2002), detailed information about their diagenetic evolution, and in particular, their dolomitization history, is lacking.

Very little is known about the Triassic dolomites of southern Hungary (structurally Tisza Mega-Unit, Fig. 1a) in general, in striking contrast to the extensively studied Triassic dolomites in northern Hungary (structurally Alcapa Mega-Unit, Fig. 1a) (see review of the dolomitization processes in Haas et al., 2017). In northern Hungary, the Triassic succession is of Alpine character, i.e., similar to the Triassic formations of the Alps, which were deposited in the northwestern part of the Tethys ocean (Feist-Burkhardt et al., 2008; Haas et al., 2017). In southern Hungary, however, the Triassic succession is similar to the epicontinental deposits of the Germanic Basin (Török, 2000a). In the southwestern part of this region, Török (2000b) studied the origin of dolomitic mottles and of saddle dolomite cements in the Middle Triassic Zuhánya Limestone Formation (Fig. 2) in the Villány Hills (Tisza Mega-Unit, Villány-Bihor Unit) (VH in Fig. 1a). Dolomite in the mottles was interpreted to have been formed from marine-derived pore waters during burial in a partly closed diagenetic system fairly soon after deposition and at relatively shallow depths, whereas the saddle dolomite cements likely precipitated during maximum burial of the succession in the Cretaceous (Török, 2000b). Another study of note is by Garaguly et al. (2018), who investigated the dolomitization of the Middle Triassic Szeged Dolomite Formation (time-equivalent to the Csukma Formation) within the Békés-Codru Unit of the Tisza Mega-Unit in southeast Hungary (Fig. 1a). These authors found that the Szeged

Dolomite was formed as a result of early reflux dolomitization, later altered by hydrothermal recrystallization.

The present paper provides a detailed interpretation of the various dolomitization and recrystallization processes that affected the Middle Triassic Csukma Formation on the basis of detailed petrographic and geochemical investigation. In addition, our study demonstrates that integration of clumped isotope data with other geochemical information can help discriminate various diagenetic fluids and processes that are otherwise difficult to distinguish, such as meteoric alteration versus burial dolomitization/recrystallization, two processes that can lead to similar petrographic features and isotopic composition of the resulting dolomite.

1.2. Materials and methods

A total of 160 thin sections were prepared from samples collected from seven locations in the Mecsek Mts. (two boreholes and five outcrops). The sampling locations are shown in Figure 1b and listed in Table 1. The thin sections were investigated in normal transmitted light on an Olympus-BX51 microscope for their petrographic features. The crystal size categories were assigned based on the scale published by Folk (1959). Dolomite textures were classified using the system of Sibley and Gregg (1987) as modified by Wright (2001) (see Machel, 2004). Selected thin sections were stained in a solution of Alizarin red-S and potassium ferricyanide to distinguish calcite, Fe-calcite, dolomite, Fe-dolomite/ankerite, using the method of Dickson (1966).

Cathodoluminescence (CL) microscopy was performed on 83 polished thin sections using a MAAS-Nuclide ELM-3 cold-cathode luminoscope at the Department of Physical and Applied Geology, Eötvös Loránd University, and using a CITL MK5-1 cold-cathode optical cathodoluminescence system at the Boone Pickens School of Geology, Oklahoma State

University, with operating conditions of 8–12 keV and 0.5–0.7 mA. The samples for CL study were selected based on their dolomite texture types and cement contents.

Stable isotope measurements ($\delta^{18}O$, $\delta^{13}C$) were performed on 101 micro-drilled calcite and dolomite powder samples (five calcite cement, 17 limestone, 14 saddle dolomite, 65 matrix dolomite samples, which represent the various dolomite types and cement phases). Analyses were performed at three laboratories. At the Institute for Geological and Geochemical Research, Hungarian Academy of Sciences and at Oklahoma State University the measurements were performed on a Finnigan Delta Plus XP Isotope ratio mass-spectrometer (IRMS), and a setup of a Thermo Delta Plus IRMS coupled to a Gas Bench II was used by Pegasus Technical Services Inc. (Cincinnati, OH, USA). All laboratories used both international (NBS-18, NBS-19) and internal laboratory standards. Reproducibility in all laboratories was better than ±0.1‰; however, differences measured on replicates of the same samples in the various laboratories were not consistent and therefore did not allow for correction of values across the various laboratories. Nevertheless, the data can be interpreted in a meaningful way because the differences between the various phases exceed the differences found by inter-lab comparison of the data. Mean values of the measurements are reported relative to the Vienna Pee Dee Belemnite standard (V-PDB ‰).

Strontium isotope composition ($^{87}Sr/^{86}Sr$) was analyzed on 10 dolomite samples (eight replacive dolomite samples, two saddle dolomite cement samples), and on two limestone samples, at the University of Kansas Radiogenic Isotope Laboratory using a VG Sector thermal ionization mass spectrometer with ±0.000014 error at a 95% confidence interval, and at the Canadian Centre for Isotopic Microanalysis at the University of Alberta using a VG 354 thermal ionization mass spectrometer with analytical precision better than 0.000024 (2σ). Systematic differences in the results across these two laboratories were corrected.

In this study, the temperatures of crystallization were determined only via the clumped isotope method. Fluid inclusion paleothermometry was not feasible due to crystal size limitations in the very fine to fine crystalline dolomites, and due to the small size of the two-phase inclusions in the medium to very coarse crystalline phases.

Carbonate clumped isotopes were measured on seven matrix dolomite samples in the Qatar Stable Isotope Laboratory at Imperial College London on a Thermo Fisher MAT 253 isotope ratio mass spectrometer in dual inlet mode, using the methodology described in Dale et al. (2014). For the evaluation of geological processes, the Δ_{47} values were converted to temperature using the calibration of Davies and John (2018) and are presented in °C. The $\delta^{18}O$ values of the parent fluids were calculated using the calibration of Horita (2014) and the results are reported relative to the Vienna Standard Mean Ocean Water standard (V-SMOW ‰).

1.3. Geological setting

1.3.1. Sedimentology and stratigraphy

The study area is located within the Pannonian Basin, in southwestern Hungary, comprising a part of the Tisza Mega-Unit (herein referred to as Tisza MU) (Bleahu et al., 1994) (Fig. 1a). During the Middle Triassic, the investigated area was located on the northwestern shelf of the Neo-Tethys, around the 30° N latitude, and it was dominated by subtropical trade winds (Török, 2000a; Szulc, 2000; Götz et al., 2003; Feist-Burkhardt et al., 2008). This paleogeographic setting resulted in semiarid to semihumid climates during Late Anisian–Early Ladinian times (Török, 1998a; Viczián, 1995; Haas et al., 2012), and in a sedimentation pattern similar to that in the Germanic Basin (Török, 2000a; Götz and Török, 2008).

The Variscan (late Paleozoic) crystalline basement in the Tisza MU is covered by molasse-type sequences of late Carboniferous to Permian age (Haas and Péró, 2004). During the Early Triassic fluvial and deltaic siliciclastic sedimentation prevailed, which was followed by the formation of carbonate ramp deposits during the Middle Triassic, suggesting a relative sea level rise (Török, 1998a). A relative sea level fall near the end of the Middle Triassic led to the deposition of the shallowing upward succession of the Csukma Formation (Konrád, 1998) (Fig. 2). Fluvial-deltaic sedimentation returned during the Late Triassic, and a more than 1,000 m thick coal-bearing sequence was formed during the Early Jurassic in fluvial, lacustrine and palustrine environments (Némedi Varga, 1998). The coal-bearing sequence is overlain by upper Lower to lower Middle Jurassic pelagic marls, and the early Middle and Late Jurassic is characterized by siliceous and carbonate sedimentation in deep marine setting (Némedi Varga, 1998). During the Early Cretaceous, continental rift-related basaltic igneous activity characterized the studied region (Harangi et al., 1996). These igneous rocks are locally overlain by Lower Cretaceous coarse-grained clastics rocks that derived from the volcanic buildups, as well as carbonate and fine-grained siliciclastic rocks representing shallow to deep marine depositional environments, respectively (Császár, 1998). Paleogene deposits are generally missing in the area except for localized occurrences of continental clastic sediments (Wéber, 1982), and Neogene sediments are also only preserved locally: the lower Miocene sediments are of alluvial fan and fluvial origin, the middle Miocene sediments are open marine limestones and shales, and the upper Miocene–Pliocene is characterized by lake-delta deposits (Magyar et al., 1999).

1.3.2. Geodynamic evolution

The Triassic succession of the Mecsek Mts. was deposited on the northern passive margin of the Neo-Tethys (Haas and Péró, 2004). The opening of the Neo-Tethys in the Middle Triassic was accompanied by complex block movements in the region of the Mecsek Mts. (Konrád, 1998). Unlike in the Southern Alps, the Middle Triassic tectonic activity in the Mecsek Mts. did not result in volcanism (cf., Bellieni et al., 2010; Lukoczki et al., 2015). In connection with the Alpine Tethys rifting, detachment of the Tisza MU from the European platform started in the Late Triassic (Haas and Péró, 2004). Related synsedimentary tectonic movements resulted in the development of a half-graben structure in the area of the Mecsek Mts., which in turn resulted in significant differences in the thickness of the sedimentary successions deposited in different parts of this basin during the Late Triassic and Jurassic (Némedi Varga, 1983). During the Early Cretaceous, the rifting was accompanied by submarine mafic igneous activity (e.g., Harangi et al., 1996; Haas and Péró, 2004). Igneous rocks (alkali basalt, trachybasalt, tephrite and phonolite) from this activity occur extensively in the Eastern Mecsek Mts., whereas in the Western Mecsek Mts. they occur only subordinately (Budai et al., 2014). These igneous rocks can be found in a belt ca. 250 km long and 50 km wide, striking SW–NE within the Tisza MU (Bilik, 1980). The igneous intrusions caused widespread hydrothermal alteration in the host rocks (Jáger, 2015).

Tectonic extension changed to compression/transpression around the middle of the Cretaceous period, and it resulted in stacking of north-vergent nappes (thrust sheets) (Bleahu et al., 1994). This Late Cretaceous tectonic phase formed the most prominent structural pattern of the Mecsek Mts. as found today: the Western Mecsek forms an anticline, whereas the Eastern Mecsek is a syncline.

The Pannonian Basin came into being as a result of a very complex tectonic evolution during the Cenozoic. Csontos et al. (2002) identified five tectonic phases: (i) thrusting and transpression during the latest Paleogene and earliest Miocene, which created the Northern Imbricates wrench zone in the northern part of the Mecsek Mts. (Fig. 1b); (ii) strike-slip faulting and subsidence during the middle Miocene; (iii) around the end of the middle Miocene (end of the Sarmatan/Serravallian) thrusting and folding occurred near the Northern Imbricates and the

Hetvehely zone (Fig. 1b); (iv) transtension during the early Pannonian (Tortonian); and (v) a major inversion created transpressive wedges and resulted in a still ongoing folding and uplift of the Mecsek Mts.

1.4. Results

1.4.1. Petrography

1.4.1.1. Very fine to fine crystalline dolomites

Very fine to fine crystalline dolomites (7 to 65 μm) of the Kán Dolomite Member (Fig. 2) occur at locations GF-1, RV, HR and VP-2 (Fig. 1b). These dolomites are thin bedded or laminated (Fig. 3a), and locally contain mm to cm size rip-up clasts. Teepee structures (10 to 20 cm high) can be recognized in outcrop (Fig. 3b). In exceptional cases, some thin bedded to laminated dolomudstones contain needle-shaped quartz pseudomorphs likely after gypsum (Fig. 3c). The massive dolomudstones typically contain round or elongate moldic pores (range in size from ca. 100 μm up to a few mm) (Fig. 3d), which are either open or are lined or filled with fine crystalline (25 to 50 μm) planar, zoned dolomite cement within a homogenously dull red dolomite matrix (Fig. 3e–f). The final pore-occluding phase in the larger moldic pores generally is blocky calcite (up to a few mm).

1.4.1.2. Medium to very coarse crystalline dolomites

Medium to very coarse crystalline (76 to 395 μm), unimodal to polymodal, planar-s to nonplanar-a dolomites occur at all studied locations. The very fine to fine crystalline dolomudstones (see

Section 4.1.1.) alternate with medium crystalline (76 to 133 µm), planar-s dolomites with poorly preserved ooid-peloidal grainstone/packstone fabrics (Fig. 4a). These tight, medium crystalline, planar-s dolomites are typically comprised of inclusion-rich dolomites with uniformly mottled CL patterns or of dolomites with cloudy cores and clear rims. The cloudy cores have mottled CL appearance, whereas the limpid rims are either zoned or homogeneously dull red (Fig. 4b–c).

The coarse to very coarse crystalline (186 to 395 µm) dolomites occur in irregular bodies near fractured zones within the fine crystalline dolomites at location HR (5 to 10 m thick/wide) and location AT (tens of m), as well as in drill cores of location VP-2 (tens of cm to few m). Poor outcrop conditions make exact determination of the spatial distribution of the coarse to very coarse crystalline dolomite bodies difficult. Similarly, the poor outcrop conditions make it impossible to provide statistically reliable measurements of the fracture orientations. These dolomites are largely fabric-destructive and are either tight or porous. Generally, the tighter dolomites are planar-s to nonplanar-a. The more porous dolomites typically have planar-s textures with intercrystal pores (Fig. 4d). The CL pattern of the coarse crystalline matrix dolomites is variable: they either display homogenous CL (from very dull to bright) or they display a mottled or blotchy appearance. The transition between the various types is sharp or gradual. At location HR (Fig. 1b), small irregular bodies (1 to 2 m thick/wide) of friable dolomite can be found within the massive coarse crystalline dolomite (Fig. 4e). This friable dolomite easily disintegrates between fingers to small crystal clusters, individual crystals or crystal fragments (Fig. 4f).

At location VA (Fig. 1b), a crinoid floatstone fabric is preserved in fine to coarse crystalline dolomites, as recognized by the presence of biomolds and partially preserved crinoid fragments (Fig. 4g), which are either mimetically replaced or are replaced by fine to coarse crystalline dolomite with blotchy CL. The matrix of these dolofloatstones is composed of planar-s dolomite. Parts of the matrix appear coarse crystalline and nearly limpid with a CL pattern of blotchy core overgrown by homogeneous rim, whereas the finer crystalline, more inclusion-rich crystals display homogeneous dull CL (Fig. 4h–i).

1.4.1.3. Limestones and dolomitic limestones

The Kozár Limestone Member, which is coeval with the lower part of the Kán Dolomite Member (Fig. 2), is made up of alternating beds of mudstone, bioclastic-peloidal-ooid grainstone, packstone, and wackestone microfacies. The uppermost part of the Zuhánya Limestone Formation, which underlies both the Kán Dolomite Member and the Kozár Limestone Member (Fig. 2), is made up of similar microfacies and is discernible from the Kozár Limestone Member primarily based on their stratigraphic position and their differing bioclast assemblages. Both limestones are locally partially to completely replaced by dolomite, and the dolomites show similar petrographic features within the two limestones. Dolomite occurs associated with all of the observed limestone microfacies. The Kozár Limestone is partially dolomitized at locations MR and AT (Fig. 1b), and the Zuhánya Limestone is partially dolomitized at location HR (Fig. 1b), where fine to coarse crystalline (20–190 μm) planar-p dolomite crystals are randomly distributed, or they occur along microfractures replacing the limestones (Fig. 5a–b). Some of the dolomite crystals are present as calcite pseudomorphs after dolomite ('dedolomite') (Fig. 5c). In the Zuhánya Limestone, the allochems are always non-mimetically replaced by dolomite (Fig. 5d). At locations AT and HR, where dolomitization is locally more extensive, the dolomites also occur in large (meters to tens of meters), irregular bodies within the limestones. The petrographic features of these dolomites are similar to those occurring in irregular bodies within the fine crystalline dolomites (see Section 4.1.2.).

1.4.1.4. Saddle dolomite cements

An overall small volume of open space filling saddle dolomite occurs in the fine crystalline dolomites, commonly as cement in veins that cross-cut the fine crystalline matrix dolomites. Larger volumes of saddle dolomite cements are associated with the coarse crystalline replacive dolomites. Based on their CL, multiple generations of saddle dolomites are discernible at each location. Complex and unique CL zonation patterns (homogenous, mottled, simple concentric and oscillatory concentric zonation with various CL intensities) (Fig. 6a–h) make correlation of the various saddle dolomite phases difficult even within the same location. Some zones within saddle dolomite cements are selectively replaced by calcite (Fig. 6i).

1.4.1.5. Calcite cements

Various calcite cement phases can be distinguished within the dolomite rocks, based on their petrographic appearance. White to colorless, coarse crystalline (up to few mm), ‘massive’ or blocky calcite (CAL-1 and CAL-2) with dull to bright orange, blotchy CL occludes voids, fills fractures, and forms cement in breccias (Fig. 7a–b). Occasionally, this generation of calcite forms large (up to 2 cm) euhedral scalenohedra (Fig. 7c). Transparent, colorless, coarse crystalline (typically up to ca. 500 μm), blocky calcite fills fractures (Fig. 7d) and it also is present as a final pore-occluding phase in some vugs. This calcite has typically dull or non-luminescent CL (Fig. 7e). Brownish, coarse crystalline (up to few mm), blocky (Fig. 7f–g) or bladed (Fig. 7h) calcite (CAL-3) fills fractures and lines vugs. This calcite is either non-luminescent or displays bright yellow/non-luminescent simple or oscillatory concentric CL zonation (Fig. 7g). Non-luminescent calcite also occurs in stylolites (Fig. 7i).

1.4.2. Isotope geochemistry

1.4.2.1. Carbon and oxygen isotopes

The carbon and oxygen isotope data are plotted in Figure 8 and tabulated in Table 2. Matrix dolomite $\delta^{18}O_{dol}$ values fall in a wide range from –12.6‰ to –2.0‰, whereas their $\delta^{13}C$ values fall within a narrower range from 0.1‰ to 4.2‰. Generally, the fine(r) crystalline dolomites have higher $\delta^{18}O_{dol}$ values whereas the coarse(r) crystalline dolomites have lower $\delta^{18}O_{dol}$ values (Fig. 8). The isotope values of saddle dolomite cements overlap with those of the medium to coarse crystalline matrix dolomites (Fig. 8), the former having $\delta^{18}O_{dol}$ values that range from –15.4‰ to –6.2‰ and $\delta^{13}C$ values that range from –1.0‰ to 3.7‰. The calcite cement $\delta^{18}O_{cal}$ values fall within the interval from –20.5‰ to –6.2‰, and the $\delta^{13}C$ values are within –8.5‰ and –0.3‰. The $\delta^{18}O_{cal}$ values of the limestone matrix range from –9.9‰ to –7.2‰, whereas their corresponding $\delta^{13}C$ values range from –3.3‰ to 2.2‰.

1.4.2.2. Clumped isotopes

Temperatures and $\delta^{18}O_{fluid}$ were determined from carbonate clumped isotope (Δ_{47}) data (Table 2). The Δ_{47} values range from 0.478 to 0.611‰, corresponding to calculated temperatures that range from 50 to 130 °C. Based on the obtained temperatures, two distinct dolomite groups can be distinguished (Fig. 9). The fine crystalline dolomites fall within the range of 50 to 67 °C, whereas the medium to coarse crystalline, planar-s to nonplanar-a dolomites range from 107 to 130 °C. The $\delta^{18}O_{fluid}$ values of the precipitating fluids calculated from the clumped isotope results range from 1.3‰$_{V\text{-}SMOW}$ to 4.3‰$_{V\text{-}SMOW}$. The values of the fine and the medium to coarse crystalline dolomites overlap, but the values of the very fine and fine crystalline dolomites are somewhat higher (2.0 to 3.0‰$_{V\text{-}SMOW}$) than the medium to coarse crystalline dolomites (1.3 to 2.6‰$_{V\text{-}SMOW}$), with the exception of an outlier coarse crystalline dolomite from location VA, which has the highest value (4.3‰$_{\text{V-SMOW}}$) (Fig. 9, Table 2).

1.4.2.3. Strontium isotopes

The ^{87}Sr/^{86}Sr values of all samples fall within a rather narrow range from 0.70780 to 0.70823 (Figs. 10, 11, Table 2). Typically, the lower values represent the medium to coarse crystalline dolomites (0.70797 to 0.70780), while the higher values represent the very fine to fine crystalline dolomites (0.70813 to 0.70819) (Fig. 11). The values of the two limestone matrix samples fall near the middle of the range of the dolomite samples, separating the very fine to fine and the medium to coarse crystalline dolomite values (Fig. 11). However, one saddle dolomite cement from location VA has the highest value observed (Table 2). The matrix dolomite from the same sample with the saddle dolomite cement from this location has the lowest value within the data set (Table 2). Therefore, both the lowest and the highest Sr isotope values were measured from different parts of the same sample (matrix dolomite and saddle dolomite cement, respectively).

1.5. Discussion

Petrographic and geochemical characteristics of the studied sedimentary succession suggest multiple phases of dolomitization, dolomite recrystallization, and cementation processes. The major diagenetic events are summarized in Fig. 12 and are discussed in detail in the following sections. Differentiation of diagenetic environments into near-surface, intermediate, and deep follows the classification of Machel (1999).

1.5.1. Near-surface dolomitization

Sedimentological features of the Kán Dolomite Member such as teepee structures, rip-up clasts, pseudomorphs after gypsum, and laminated dolomudstones (Fig. 3), suggest that this unit was deposited in a peritidal environment, in accordance with earlier sedimentological studies (e.g., Török, 1998a). The molds and pseudomorphs after gypsum suggest that the salinity of the pore water reached gypsum saturation at least periodically. The fluid compositions calculated from the clumped isotope data of the very fine and fine crystalline dolomites (2.0 to 3.0‰$_{\text{V-SMOW}}$) (Fig. 11) correspond closely to values measured in evaporatively concentrated brines from supratidal settings, even though the values represent only the lower end of the range characterizing such fluids (ca. +1‰$_{\text{V-SMOW}}$ to +10‰$_{\text{V-SMOW}}$, typically around +2‰$_{\text{V-SMOW}}$ to +5‰$_{\text{V-SMOW}}$) (e.g., Gat and Levy, 1978; McKenzie, 1981; Major et al., 1992, Machel and Buschkuehle, 2008). Possible explanations of the oxygen isotopic composition calculated for the Kán Dolomite include a less arid climate (cf. Major et al., 1992), and meteoric influx that would have lowered the δ^{18}O of the seawater, as suggested by Korte et al. (2005) to explain the lower δ^{18}O values of Middle Triassic carbonates of the Germanic Basin. A minor meteoric input may also be reflected in the Sr isotope values of the very fine to fine crystalline dolomites (^{87}Sr/^{86}Sr=0.70813 to 0.70819) (Fig. 11), which are slightly elevated with respect to normal marine values of the Middle Triassic Neo-Tethys Ocean (ca. 0.70772 around the Anisian/Ladinian boundary) (Korte et al., 2003) (Fig. 10). Elevated Sr isotope values characterize also the regionally extensive Upper Muschelkalk carbonates (Middle Triassic in the Germanic Basin) (Korte et al., 2003; Adams et al., 2018), which are coeval with the Csukma Formation. Elevated Sr isotope values could have been derived from meteoric influx from exposed Variscan crystalline rocks in the hinterland through riverine discharge into the epicontinental sea of the Germanic Basin (Korte et al., 2003). However, in the Csukma Formation such meteoric influx appears to have been relatively moderate, probably due to the connection of the sedimentary environment to the Neo-Tethys Ocean. Therefore, the estimated fluid composition is in agreement with paleogeographic and paleoclimatic reconstructions (e.g., Szulc, 2000), which claim that the region of the Mecsek Mts. was situated in a transitional position between the Germanic Basin ('Muschelkalk Sea') and the Neo-Tethys at around the 30° paleolatitude, and that semiarid to semihumid climates prevailed during Middle Triassic times.

The two most likely dolomitization models to explain dolomitization of the Kán Dolomite Member are the sabkha and the reflux models, whereby processes of both models may have been involved, albeit to differing degrees.

Sabkha dolomitization generally produces very limited amounts of dolomite in thin beds (e.g., Machel 2004). Therefore, it is highly unlikely that sabkha processes led to complete dolomitization of the Kán Dolomite Member (up to ca. 300 m thickness). However, sabkha dolomitization may have contributed to the early dolomitization of the Kán Dolomite Member by virtue of producing very small amounts of disseminated (proto)dolomite that served as nuclei for subsequent, more extensive dolomitization (cf., Gregg et al., 2015; Kaczmarek et al., 2018).

The bulk of the dolomite of the Kán Dolomite Member likely was produced by reflux dolomitization, a mechanism originally proposed by Adams and Rhodes (1960) and later verified by virtue of case studies and reactive transport modeling as a viable mechanism to generate large volumes of regionally extensive dolomites (e.g., Montanez and Read, 1992; Jones et al., 2003; Machel, 2004). The limited evidence of evaporation (small amounts of gypsum pseudomorphs) suggests that the salinity of the pore water was typically mesohaline (salinity between normal seawater and gypsum saturation) and occasionally hypersaline up to at least gypsum saturation. Brine generation is assumed to have been continuous during the latest Anisian–Ladinian, whereby minor changes in relative sea level led to shifts in the area of brine generation. Dolomitization was penecontemporaneous with deposition and likely restricted to the upper 2 to 3 m of the succession (cf. modelling results of Jones et al., (2003) on the Devonian Grosmont

Formation for analogy). In this manner, dolomitization proceeded bed-by-bed during the estimated relatively long duration of the reflux circulation (latest Anisian through most of the Ladinian), with overall rather low depositional rates (estimated ca. 10 cm/ky based on the thickness and age of the succession).

In contrast, the middle ramp carbonates of the Kozár Limestone Member contain only dolomites with characteristic high temperature textures (fabric destructive, medium to coarse crystalline, planar-s to nonplanar-a dolomites associated with various microfacies) (Fig. 5). The apparent lack of early dolomitization of these middle ramp carbonates can be explained by the interaction of geothermal and reflux circulation similar to the situation modelled by Jones et al. (2004), which showed that reflux circulation is restricted to the inner ramp, whereas the more distal parts of the ramp are dominated by geothermal circulation. It is therefore inferred that the Kozár Limestone Member escaped early dolomitization because the refluxing brines could not reach the middle ramp shoal deposits (Fig. 13a).

1.5.2. Intermediate burial diagenesis

1.5.2.1. First dolomite recrystallization

Dolomites that form in near-surface environments from seawater or evaporitic brines are metastable, and therefore are prone to recrystallization due to increasing temperature and pressure during burial, and/or changing fluid composition (Land, 1985; Gregg and Shelton, 1990; Machel, 2004; Kaczmarek et al., 2018). The dolomites in Kán Dolomite Member fall into this category.

Reflux dolomitization of the Kán Dolomite is inferred from three aspects: the paleogeographic and paleoclimatic setting (peritidal environment and semiarid to semihumid climate), its sedimentological characteristics (e.g., teepee structures, evaporite pseudomorphs), and the $\delta^{18}O_{fluid}$ value of the fluid calculated from the clumped isotope data of the fine crystalline dolomites (2.0 to 3.0‰$_{V-SMOW}$). However, reflux dolomites typically have $\delta^{18}O_{dol}$ values around +4‰$_{V-PDB}$ (e.g., Land, 1985), whereas the $\delta^{18}O_{dol}$ values of the fine crystalline dolomites of the Mecsek Mts. are significantly lower (highest value is –1.9‰$_{V-PDB}$, Fig. 8, Table 2). This discrepancy between the measured and the expected values can be explained by significant recrystallization (*sensu* Machel 1997) of the reflux dolomites with respect to $\delta^{18}O_{dol}$. This notion is further supported by the clumped isotope data, which indicate elevated temperatures (50 to 67 °C) and mesohaline brines (2.0 to 3.0‰$_{V-SMOW}$) (Fig. 9). Such temperatures are too high for near-surface diagenetic settings (except for a few exceptionally hot playa settings) and thus are interpreted to represent an intermediate burial setting, corresponding to 1–2 km burial depth, as estimated from the clumped isotope temperatures using a 25 to 30°C/km geothermal gradient. Based on the burial history of the area (Haas et al., 1995), the Kán Dolomite Member is estimated to have reached this burial depth and temperature range during the Early Jurassic (Fig. 13b). The driving force for recrystallization of the fine crystalline dolomites likely was increased temperature due to burial, possibly aided by a change in fluid composition and an additional temperature rise caused by geothermal circulation of the connate brines. The latter is suggested by the $\delta^{18}O_{dol}$ and Δ_{47} values of the Kán Dolomite, which were reset by water-rock interactions to now represent the environment of recrystallization, i.e., temperatures higher than that during dolomitization and a slightly modified $\delta^{18}O_{fluid}$ composition, while preserving the mesohaline $\delta^{18}O_{fluid}$ signature of the diagenetic fluids (connate brine) (Fig. 8, 9).

Recrystallization by meteoric fluids can also be the cause of the observed negative shift in the $\delta^{18}O_{dol}$ values. However, this process is excluded for the Kán Dolomite Member based on the calculated $\delta^{18}O_{fluid}$ values. Alternatively, the observed negative $\delta^{18}O_{dol}$ values can result from dolomitization during burial (as opposed to recrystallization of near-surface dolomites during burial). However, numerical modelling studies indicate that even though refluxing brines may advect down to significant depths (up to ~2 km, but only in the absence of effective aquitards; Jones et al., 2004), dolomitization is likely restricted to the uppermost part of the carbonate succession (2 to 3 m) because the Mg^{2+} available for dolomitization is rapidly exhausted (Jones et al., 2003). Therefore, we contend that the negative $\delta^{18}O_{dol}$ values of the fine crystalline dolomites are indeed the result of burial recrystallization in mesohaline connate fluids.

1.5.2.2. Gypsum dissolution and dolomite cementation

Synsedimentary gypsum that had formed during periods of increased salinity either was dissolved almost penecontemporaneously during periodic freshening of the pore fluids via latent reflux *sensu* Jones et al. (2003), or via thermally driven circulation during intermediate burial of the mesohaline pore waters that were likewise undersaturated with respect to gypsum. One or both alternatives left behind moldic pores in the fine crystalline dolomites. The available data do not provide sufficient evidence to decide between these two alternatives.

Increasing burial and related stylolitization may have periodically caused the pore fluids to become supersaturated with respect to dolomite due to the newly available Mg^{2+} that was liberated during pressure dissolution of the dolomite (cf., Wanless, 1979). The small amounts of planar dolomite cements that line or fill moldic pores in the fine crystalline dolomites (Fig. 3e–f), and the thin limpid dolomite overgrowth cements observed in the medium crystalline, planar-s dolomites with poorly preserved ooid-peloidal grainstone fabric (Fig. 4a), are thus interpreted to have likely formed as a by-product of pressure solution of the preexisting dolomites. The overlap and the lack of a well-defined boundary in the $\delta^{18}O_{dol}$ values between the very fine to fine crystalline and the medium to very coarse crystalline dolomites (Fig. 8) thereby likely reflects the mixing of the values from two populations of dolomite, which are intergrown and thus cannot be separated via microdrilling: the lower temperature (higher $\delta^{18}O_{dol}$) recrystallized matrix dolomites (see Section 5.2.1) and the higher temperature (lower $\delta^{18}O_{dol}$) cements. Alternatively, dolomite cementation might also have been related to the incursion of fluids with elevated temperature via fractures (see Section 5.3.1.), in which case the two dolomite phases in the powder mixtures would be dolomite cement precipitated from such fracture-related fluids and the earlier recrystallized matrix dolomite. Further investigation using *in situ* secondary ion mass spectrometry (SIMS) is required to distinguish between these alternatives.

1.5.3. Deep burial diagenesis

1.5.3.1. High-temperature fault-controlled dolomitization and second recrystallization event

The irregular bodies of fabric destructive, coarse crystalline, planar-s to nonplanar-a dolomites with saddle dolomite cements that are present within the fine crystalline dolomites (Kán Dolomite) and in the coeval and underlying limestones (Kozár and Zuhánya Limestones, respectively) (Fig. 5–6) are interpreted to have formed in a deep burial setting from ‘hot’ fluids circulating through faults. These coarse crystalline dolomites have very low $\delta^{18}O_{dol}$ values (–15.4‰ $_{V\text{-}PDB}$ to –6.2‰$_{V\text{-}PDB}$) (Fig. 8), and the clumped isotope analysis yielded temperature of 107 to 130 °C for the parent fluid (Fig. 9). These data suggest that interaction of the rocks with these ‘hot’ fluids resulted in recrystallization of the pre-existing fine crystalline dolomites, and in the dolomitization of the previously undolomitized coeval Kozár and the underlying Zuhánya Limestones. Thus, parts of the Kán Dolomite Member appear to have been recrystallized for a second time, this time driven by the fault-derived ‘hot’ fluids.

The formation of some of these coarse crystalline dolomites was previously interpreted to have been related either to the Early Cretaceous submarine mafic igneous activity in the area (Wéber, 1978), or to the Late Cretaceous or Cenozoic thrusting (Nagy, 1968). However, no convincing evidence was provided by these studies to support the hypothesis of igneous activity-related dolomitization. The spatial proximity of mafic igneous intrusions to the coarse crystalline dolomites is no proof of a genetic relationship. Also, the Sr isotope values of the coarse crystalline dolomites are near or higher than that of Mesozoic seawater (Fig. 10), a trend opposite to what is expected from fluids that had interacted with mafic intrusions (cf. Burke et al., 1982; Banner, 1995). Therefore, the formation of the coarse crystalline dolomites from fluids related to Early Cretaceous igneous activity is not substantiated.

We propose that, as suggested by the Sr isotope data, the dolomitizing/recrystallizing agent was seawater, which was drawn down through a fault system that was created during the Early Cretaceous rifting (Fig. 13c). The medium to coarse crystalline dolomites fall into a narrow range and have slightly lower $^{87}Sr/^{86}Sr$ ratios (0.70780 to 0.70797) than that of the very fine to fine crystalline dolomites (0.70813 to 0.70819) and the undolomitized limestones (0.70798 to 0.70802) (Fig. 11, Table 2). This finding suggests that the dolomitizing and/or dolomite recrystallizing fluid had a Sr isotope composition lower than that of the precursor rocks. A candidate for such a fluid is Early Cretaceous seawater (Fig. 10). In this scenario, surface-breaching rift faults that were created related to the opening of the Vahic oceanic basin during the Early Cretaceous (cf., Haas and Péró, 2004) provided conduits for the descending seawater, which was heated either due to the regional geothermal heat or due to more localized heat of nearby igneous intrusions. Thermal convection was thus induced, and the hot fluids ascended along faults, thereby facilitating recrystallization of pre-existing fine crystalline dolomites for a second time in the vicinity of the faults. Where these hot fluids encountered the previously undolomitized middle ramp Kozár Limestone and the underlying Zuhánya Limestone, these limestones underwent extensive, pervasive dolomitization in the vicinity of the faults (Fig. 13c), with the amount of dolomite decreasing with increasing distance from the fluid source. The source of Mg^{2+} for this type of dolomitization thus was Cretaceous seawater, which had not lost its dolomitizing potential while descending [cf., mass balance calculations of Hirani et al. (2018) and reactive transport modelling results of Corbella et al. (2014) for similar scenarios]. The lesser amount of dolomite found in the Kozár Limestone at location MR is interpreted to be the result of its distal position from the major faults (not exposed) that transported the dolomitizing fluids. Based on the Sr isotope composition and the calculated $\delta^{18}O_{fluid}$ values of the studied coarse crystalline dolomites in the Mecsek Mts. (Fig. 11), the diagenetic fluid is interpreted to have been a mixture of the connate fluids and the Early Cretaceous seawater that was drawn down through the faults. Similar scenarios were proposed to explain the dolomitization of Lower Cretaceous carbonates in southern Italy (Rustichelli et al., 2017) and in eastern Spain (Corbella et al., 2014). According to these studies, seawater was likely drawn down and circulated through a fault system that was created during the Cretaceous, thereby dolomitizing the rocks in the vicinity of the faults. Therefore, it seems possible that fault-controlled seawater dolomitization related to the Early Cretaceous rifting in the Tethyan realm was not uncommon. Similarly, Oligo–Miocene seawater drawn down and convected through rift related faults was interpreted to have been the dolomitizing fluid in Oligocene–Miocene carbonates in Borneo (Wilson et al., 2007) and in Eocene carbonates in Egypt (Hollis et al., 2017; Hirani et al., 2018).

1.5.3.2. Geothermal versus hydrothermal processes

By definition, hydrothermal dolomites are formed from fluids that are at least 5 to 10 °C warmer than the host rock (see Machel and Lonnee, 2002). To assess whether a dolomite can be considered hydrothermal or not, it is necessary to determine the temperature of the country rock relative to the diagenetic fluid at the time of dolomite formation. If the temperature of dolomite formation was higher than the maximum burial temperature of the surrounding rocks, then the dolomite was formed hydrothermally. If, however, the temperature of dolomite formation was lower than the maximum burial temperature, then this dolomite may or may not be hydrothermal, depending on when it formed during the burial history (Machel and Lonnee, 2002).

No precise estimates of maximum burial depth and associated maximum burial temperature are available for the Csukma Formation. However, its burial depth can be estimated to have been around 5 km during the Early Cretaceous based on the burial history of the area (Haas et al., 1995). In addition, vitrinite reflectance values available on coal samples from the Lower Jurassic Mecsek Coal Formation (Fig. 2) can be used to estimate the maximum burial temperature of the Csukma Formation. The maximum burial temperature of the Mecsek Coal was determined to be 138 °C (Vető, 1978). The total thickness of the Kantavár and Karolinavölgy Formations (Fig. 2), which are situated between the Mecsek Coal and the Csukma Formations, is up to 720 m (thickness data from Török, 1998b). Using a conservative 25 °C/km geothermal gradient, this additional burial depth would correspond to ca. 156 °C maximum burial temperature of the studied dolomites. Based on clumped isotope measurements, the coarse crystalline dolomites were formed/recrystallized at temperatures 107 to 130 °C. Note, however, that the uncertainty of the methods (clumped isotope and vitrinite reflectance thermometry) together with the uncertainties of the estimates based on the burial history are beyond the 5 to 10 °C temperature range that is needed to differentiate between geothermal and hydrothermal processes. Nevertheless, the temperature of the dolomitizing fluid likely was not significantly, if at all, higher than the temperature of the surrounding rocks, if the dolomitization indeed occurred during the Early Cretaceous when these rocks were deeply buried. Therefore, these dolomites cannot be considered hydrothermal dolomites as defined by Machel and Lonnee (2002). However, in the area of the Northern Imbricates (Fig. 1b), where medium to coarse crystalline, planar-s to nonplanar-a dolomites with varied CL patterns occur (VA location, Figs. 1b, 4), the maximum burial temperature of the Mecsek Coal Formation was determined to be only 55 °C, and the coalification rank of the coal was only lignite before the emplacement of the igneous intrusions, which caused local coking of the lignite (Vető, 1978). Due to the different burial history of the Northern Imbricates compared to other parts of the Mecsek Mts. (Némedi Varga, 1995), the succession at location VA was not buried as deeply as those at the other studied locations. Using the above calculation, the country rock temperature is estimated to have been around 73 °C, whereas the dolomitizing fluid at location VA was determined to be 130 °C based on clumped isotope measurement. Thus, the rocks at location VA were presumably significantly cooler than the dolomitizing fluid. Therefore, the coarse crystalline dolomites of the VA location are hydrothermal in origin as defined by Machel and Lonnee (2002). Furthermore, the $\delta^{18}O_{fluid}$ value calculated for a coarse crystalline dolomite from this location is significantly higher ($4.3‰_{V\text{-}SMOW}$) than that of the other coarse crystalline dolomites at other locations (1.3 to $2.6‰_{V\text{-}SMOW}$) (Fig. 9), which suggests that the dolomitizing fluids at the VA location had a different source compared to the other locations in the Central and Western Mecsek (Fig. 1b), or these dolomites were later recrystallized in fluids related to a Late Cretaceous fluid flow event (see Section 5.3.3).

1.5.3.3. Saddle dolomite cementation

Saddle dolomite filling vugs and fractures within the medium to coarse crystalline, planar-s to nonplanar-a dolomites can be found at several locations (VA, AT, VP-2, HR), whereas saddle dolomite occurs only scarcely in the fine crystalline dolomites filling narrow fractures (e.g., in the VP-2 and GF-1 drill cores). The rather wide ranges in both the $\delta^{18}O_{dol}$ and $\delta^{13}C$ values of the saddle dolomite cements (Fig. 8, Table 2) likely indicate differences in the temperature of precipitation, and a difference in either the origin of the fluids or the fluid-to-rock ratio in the diagenetic system (e.g., Banner and Hanson, 1990). The saddle dolomites identified in the study area likely formed in two different ways: from seawater that was drawn down and circulated through the sequence along normal faults during the Early Cretaceous, and from basinal brines ascending along thrust faults during the Late Cretaceous or Cenozoic. Saddle dolomites with $\delta^{18}O_{dol}$ and $\delta^{13}C$ values close to the values of the country rock (e.g., at locations VP-2 and AT) (Table 2) may indicate a low fluid-to-rock ratio and/or a long residence time of the fluids enabling near isotopic equilibration of the pore fluid with the host rock.

Based on the CL pattern of the saddle dolomites (Fig. 6), those with concentric growth zonation seem to have grown in multiple episodes or from fluids with changing composition. However, microdrilling cannot separate the observed growth zones. Therefore, stable isotope values measured on such samples are averages over the various growth zones. In addition to the concentric growth zonation within one set of saddle dolomite crystals filling a pore/fracture, there are samples with oscillatory zonation, which is a bulk solution disequilibrium phenomenon (Machel, 1990; Machel and Burton, 1991). Furthermore, changes in the chemistry or temperature of the diagenetic fluids along their flow paths may also cause variations in the CL pattern of time-equivalent cement generations (Machel and Burton, 1991). In this light, correlation of the various saddle dolomite types and/or growth zones is not possible within the study area. Again, *in situ* secondary ion mass spectrometric (SIMS) analysis of the isotopic composition of the various saddle dolomite types would help better characterize and correlate these cements.

The Sr isotope ratios of pairs of matrix dolomite and saddle dolomite from the same samples can be used to further characterize the fluid(s) of saddle dolomite formation. Such samples were analyzed from two locations (VA and AT, Fig. 1b) where the dolomites are interpreted to have been dolomitized for the first time by the high-temperature fluids (see Sections 5.3.1. and 5.3.2). In both cases, the Sr isotope ratios of the saddle dolomite cements are higher than that of the matrix dolomite (AT: 0.707940. and 0.70781, VA: 0.70823 and 0.70780, respectively) (Fig. 11), which indicate that the parent fluid of the saddle dolomite cement was more radiogenic (contained more radiogenic Sr) than the fluid that had caused the replacive matrix dolomitization. The more radiogenic Sr isotope composition of the saddle dolomite suggests a ‘basinal’ origin of the precipitating fluids, i.e., fluids that were derived from either the Variscan crystalline basement rocks, or from late Paleozoic–early Mesozoic siliciclastic rocks (see Fig. 2).

The complex zonation and multiple generations of the saddle dolomite cements, therefore, likely reflect multiple episodes of saddle dolomite cementation, including precipitation from fluids derived from Cretaceous seawater, and repeated expulsion of basinal fluids during either the Late Cretaceous thrusting events and/or during the various thrusting events of the Miocene tectonic phases (cf. Csontos et al., 2002), even though correlations of these episodes is not possible from one location to another, as noted earlier. Such basinal fluid flow may have been responsible for resetting the $\delta^{18}O_{fluid}$ value of the dolomite at location VA, which is markedly different from the other studied dolomites. In southeast Hungary (Szeged Basin), hydrothermal alteration/recrystallization of the time-equivalent Szeged Dolomite was interpreted to have been caused by Late Cretaceous metamorphic fluids (Garaguly et al., 2018). Comparison of the Sr isotopic composition of the hydrothermal dolomites in the Szeged Basin with those in the Mecsek Mts. (Sr isotope ratios up to 0.709674 of the saddle dolomites in Szeged Dolomite according to Garaguly et al. (2018), compared to 0.70823 of the saddle dolomite at the VA location in the Mecsek Mts.) reveals that the hydrothermal fluids were of different origin. The Szeged Dolomite is part of the Békés-Codru Unit (nappe system), whereas the Csukma Formation belongs to the Mecsek Unit (nappe system); therefore, differences in the hydrothermal fluid sources are reasonable.

1.5.4. Post-dolomitization diagenesis

Even though only limited data are available to reconstruct the post-dolomitization diagenetic processes that affected the studied successions, an attempt was made to correlate the analyzed calcite cement phases to calcite cementation events known from the literature pertinent to the study area, and to offer a possible explanation leading to the disintegration of some of the dolomites at location HR.

Petrographic and stable isotope data (Figs. 7 and 8) suggest that the late diagenetic calcites found within the studied dolomite successions were formed from fluids of two distinct sources, hydrothermal and meteoric. Based on the paragenetic sequence and the tectonic evolution of the area (Fig. 12), the calcite cementation occurred during uplift following maximum burial, i.e., in a telogenetic setting. Based on the $\delta^{18}O_{cal}$ and $\delta^{13}C$ values, three types of calcite cement can be differentiated, even though two of these are only represented by one sample each (Fig. 8). CAL-1 is a white, 'massive' fracture filling calcite sample from location VA with very low oxygen and relatively high carbon isotope values ($\delta^{18}O_{cal}$ –20.5‰; $\delta^{13}C$ –0.9‰). CAL-2 is a white, blocky calcite cement from a tectonic breccia from location GF-1 with less negative oxygen and similar carbon isotope values ($\delta^{18}O_{cal}$ –12.4‰; $\delta^{13}C$ –0.3‰). CAL-3 are three fracture and vug-filling calcite samples of brownish color from locations HR, RV and VP-2 with distinctly different isotope signature ($\delta^{18}O_{cal}$ –7.8 to –6.2‰; $\delta^{13}C$ –8.5 to –4.8‰) from the other two samples (CAL-1 and CAL-2).

At location VA, dolomitization and saddle dolomite cementation indicate that hydrothermal processes (section 5.3) preceded calcite cementation. While conclusive evidence is not available, it may well be that this calcite formed from the same hydrothermal fluid that had previously formed saddle dolomite at this location, and the fluid had evolved from dolomite formation to calcite formation over time, either due to cooling or to a change in composition (see Fig. 1 in Machel, 2004). Hydrothermal calcite veins are widespread in the Eastern Mecsek Mts. and Mórágy Hills (Fig. 1b) and the origin of these and the calcite vein at location VA (CAL-1) may be similar. The origin of the calcite veins found within Paleozoic crystalline rocks in these areas were linked to hydrothermal processes either related to the Early Cretaceous igneous activity

(Jáger et al., 2012; Dabi et al., 2013) or to hydrothermal fluid circulation during the Late Cretaceous (Poros et al., 2008). Based on the geological evolution of the Northern Imbricates (location VA, Fig.1b), the calcite cementation (CAL-1) was likely related to the Late Cretaceous hydrothermal fluid flow event (fluid flow event 3b of Poros et al., 2008).

On the other hand, the calcite cement from location GF-1 (CAL-2) (Fig. 1b) has an isotopic composition similar to calcite veins that occur in Permian siltstones in the Western Mecsek Mts. ($\delta^{18}O_{cal}$ –16 to –12‰$_{V\text{-}PDB}$, originally reported in V-SMOW, and $\delta^{13}C$ –5.5 to –0.2‰) (Demény and Fórizs, 1996). These calcites in the siltstones were determined to have precipitated from waters of meteoric origin during a period of warm climate before the Pleistocene on the basis of stable isotope and fluid inclusion studies (Demény and Fórizs, 1996). The similarity of the values and geological evolution of the area suggest that the calcite cement at location GF-1 (CAL-2) formed from the same or similar fluid, likely during the major inversion tectonic event during the Pliocene (cf. Csontos et al., 2002).

The $\delta^{18}O_{cal}$ and $\delta^{13}C$ values of the third group of calcite cements (CAL-3) is distinct from the other two and they fall near the more positive end of the range of values measured on speleothems ($\delta^{18}O$ –12.3 to –6.5; $\delta^{13}C$ –12.7 to –7.3) that precipitated during the last glacial period in a cave that formed in the Middle Triassic Lapis Limestone Formation (Fig. 2) in the Western Mecsek Mts. (Koltai et al., 2017). The similarity in the values indicate that the late fracture and vug filling calcites (CAL-3) of the current study likely precipitated from meteoric fluids during the Pleistocene. In addition to the climatic variation, the more positive $\delta^{18}O_{cal}$ and $\delta^{13}C$ values of the CAL-3 calcite cements may reflect the extent of the interaction between the meteoric fluid and the country rock and/or variable mixing proportions of the connate waters with the meteoric fluids.

The incursion of meteoric waters is further suggested by dedolomitization (replacement of dolomite by calcite, see Nader et al., 2008; Hauck et al. 2018) of some non-planar replacive dolomites within the dolomitic limestones (Fig. 5c), as well as by selective replacement of certain, likely originally iron-rich, zones of saddle dolomite cements (Fig. 6i). Calcite filled some stylolitic surfaces in the fine crystalline dolomites that likely opened up due to uplift related unloading. Even though it was not possible to determine the isotope composition of these minor calcite phases, the geological evolution of the area suggest their precipitation with the involvement of meteoric water. The isotope signature of the limestone samples (Fig. 8) may indicate meteoric recrystallization (neomorphism *sensu* Folk, 1965) or burial diagenesis. A detailed evaluation of the diagenetic evolution of the limestones is the subject of a forthcoming paper.

A peculiar feature within the coarse crystalline dolomites at location HR (Fig. 1b) is the occurrence of small (1–2 m thick/wide) irregular bodies of friable (disintegrating), coarse crystalline dolomites (Fig. 4e–f). The stable isotopic composition of these disintegrating dolomites is indistinguishable from that of the massive coarse crystalline dolomite within which they occur. Even though detailed chemical analysis of the disintegrating dolomites in the Mecsek Mts. has not been performed, the stable isotope data suggest that the process leading to the disintegration did not involve chemical alteration of the pre-existing dolomites, although chemical weathering processes cannot be ruled out. A more likely explanation for this phenomenon is 'cryogenic powderization' (repeated freezing-thawing cycles) as suggested by Poros et al. (2013) in the case of the Upper Triassic Fődolomit (Hauptdolomit/Dolomia Principale equivalent) in the Transdanubian Range, Hungary. Further assessment of the origin of the disintegrating dolomites is beyond the scope of the present study.

1.6. Conclusions

The peritidal–shallow marine carbonates of the Csukma Formation of the Mecsek Mts. underwent multiple phases of dolomitization, dolomite recrystallization and cementation. Integration of petrographic and geochemical data with paleogeography (e.g., Török, 1998a; Szulc, 2000) and tectonic evolution (e.g., Csontos et al., 2002; Haas and Péró, 2004) enabled a detailed interpretation of the diagenetic processes that affected the Csukma Formation.

The most important findings of this study are the following:

1. Integration of carbon, oxygen, strontium and clumped isotope data can help discriminate various diagenetic fluids and processes that are otherwise difficult to distinguish.
2. Extensive dolomitization of the Csukma Formation (Kán Dolomite Member) was primarily controlled by its paleogeographic setting (i.e., depositional environment and climatic conditions). The peritidal inner ramp carbonates likely were dolomitized by refluxing evaporatively concentrated brines, in agreement with earlier studies (e.g., Konrád, 1998; Török, 1998a). These reflux dolomites were significantly recrystallized with respect to $\delta^{18}O_{dolomite}$ in the presence of connate brines in an intermediate burial setting.
3. The coarse crystalline dolomites were formed in a deep burial setting as a result of dolomitization and recrystallization by high-temperature fluids. Such fluids were likely derived from Cretaceous seawater that was drawn down and circulated through rift-related faults. This study, therefore, provides a new example for fault-controlled seawater dolomitization occurring in extensional basins.

References

Adams, A., Diamond, L.W. and Aschwanden, L., 2018. Dolomitization by hypersaline reflux into dense groundwaters as revealed by vertical trends in strontium and oxygen isotopes: Upper Muschelkalk, Switzerland. Sedimentology. doi:10.1111/sed.12530

Adams, J.E. and Rhodes, M.L., 1960. Dolomitization by seepage refluxion. AAPG Bulletin, 44(12): 1912–1920.

Al-Aasm, I.S. and Packard, J.J., 2000. Stabilization of early–formed dolomite: a tale of divergence from two Mississippian dolomites. Sedimentary Geology, 131(3–4): 97–108.

Banner, J.L., 1995. Application of the trace element and isotope geochemistry of strontium to studies of carbonate diagenesis. Sedimentology, 42(5): 805–824.

Banner, J.L., Hanson, G. and Meyers, W., 1988. Water-rock interaction history of regionally extensive dolomites of the Burlington-Keokuk Formation (Mississippian): isotopic evidence.

Banner, J.L. and Hanson, G.N., 1990. Calculation of simultaneous isotopic and trace element variations during water-rock interaction with applications to carbonate diagenesis. Geochimica et Cosmochimica Acta, 54(11): 3123–3137.

Bellieni, G., Fioretti, A., Marzoli, A. and Visonà, D., 2010. Permo–Paleogene magmatism in the eastern Alps. Rendiconti Lincei, 21(1): 51–71.

Bilik, I., 1980. Lower Cretaceous submarine (rift) volcanism in South Transdanubia (South Hungary). In: E. Bisztricsány and G. Szeidovitz (Editors), Proceedings of the 17th Assembly of the European Seismological Congress. Akadémiai Kiadó, Budapest.

Bleahu, M., Mantea, G., Bordea, S., Panin, S., Stefanescu, M., Sikic, K., Haas, J., Kovács, S., Péró, C. and Bérczi-Makk, A., 1994. Triassic facies types, evolution and paleogeographic relations of the Tisza Megaunit. Acta Geologica Hungarica, 37(3–4): 187–234.

Bonifacie, M., Calmels, D., Eiler, J.M., Horita, J., Chaduteau, C., Vasconcelos, C., Agrinier, P., Katz, A., Passey, B.H. and Ferry, J.M., 2017. Calibration of the dolomite clumped isotope thermometer from 25 to 350° C, and implications for a universal calibration for all (Ca, Mg, Fe) CO_3 carbonates. Geochimica et Cosmochimica Acta, 200: 255–279.

Budai, T., Haas, J., Konrád, G. and Koroknai, B., 2014. Tisza Mega-unit. In: J. Haas and T. Budai (Editors), Geology of the pre-Cenozoic basement of Hungary. Explanatory notes for "Pre-Cenozoic geological map of Hungary" (1:500 000). Geological and Geophysical Institute of Hungary, Budapest.

Burke, W., Denison, R., Hetherington, E., Koepnick, R., Nelson, H. and Otto, J., 1982. Variation of seawater $^{87}Sr/^{86}Sr$ throughout Phanerozoic time. Geology, 10(10): 516–519.

Came, R.E., Azmy, K., Tripati, A. and Olanipekun, B.J., 2017. Comparison of clumped isotope signatures of dolomite cements to fluid inclusion thermometry in the temperature range of 73–176°C. Geochimica et Cosmochimica Acta, 199: 31–47.

Corbella, M., Gomez-Rivas, E., Martín-Martín, J.D., Stafford, S., Teixell, A., Griera, A., Travé, A., Cardellach, E. and Salas, R., 2014. Insights to controls on dolomitization by means of reactive transport models applied to the Benicàssim case study (Maestrat Basin, eastern Spain). Petroleum Geoscience, 20(1): 41–54.

Császár, G., 1998. Lower and Middle Cretaceous stratigraphy of the Mecsek-Villány unit. In: I. Bérczi and Á. Jámbor (Editors), Stratigraphy of the geological formations of Hungary. MOL-MÁFI, Budapest, pp. 353–370.

Csontos, L., Benkovics, L., Bergerat, F., Mansy, J.L. and Wórum, G., 2002. Tertiary deformation history from seismic section study and fault analysis in a former European Tethyan margin (the Mecsek–Villány area, SW Hungary). Tectonophysics, 357(1): 81–102.

Csontos, L., Nagymarosy, A., Horváth, F. and Kovác, M., 1992. Tertiary evolution of the Intra-Carpathian area: A model. Tectonophysics, 208(1): 221–241.

Dabi, G., Bajnóczi, B., Schubert, F. and M. Tóth, T., 2013. The origin and role of a calcite-filled microcrack generation in a metamorphic crystalline complex: The characterization of a fossilised seismic permeability system. Tectonophysics, 608: 792–803.

Dale, A., John, C.M., Mozley, P.S., Smalley, P.C. and Muggeridge, A.H., 2014. Time-capsule concretions: Unlocking burial diagenetic processes in the Mancos Shale using carbonate clumped isotopes. Earth and Planetary Science Letters, 394(Supplement C): 30–37.

Davies, A.J. and John, C.M., 2018. The clumped (^{13}C–^{18}O) isotope composition of echinoid calcite: further evidence for “vital effects” in the clumped isotope proxy. Geochimica et Cosmochimica Acta. doi: https://doi.org/10.1016/j.gca.2018.07.038

Demény, A., Fórizs, I. and Máthé, Z., 1996. A Preliminary Stable Isotope Study on a Potential Radioactive Waste Repository Site in the Mecsek Mountains, Southern Hungary. Rapid Communications in Mass Spectrometry, 10(11): 1415–1417.

Dickson, J., 1966. Carbonate identification and genesis as revealed by staining. Journal of Sedimentary Research, 36(2).

Durocher, S. and Al–Aasm, I.S., 1997. Dolomitization and neomorphism of Mississippian (Visean) upper Debolt Formation, Blueberry Field, northeastern British Columbia: geologic, petrologic, and chemical evidence. AAPG bulletin, 81(6): 954–977.

Eiler, J.M., 2007. “Clumped-isotope” geochemistry—The study of naturally-occurring, multiply-substituted isotopologues. Earth and Planetary Science Letters, 262(3–4): 309–327.

Feist-Burkhardt, S., Götz, A.E., Szulc, J., Borkhataria, R., Geluk, M., Haas, J., Hornung, J., Jordan, P., Kempf, O. and Michalík, J., 2008. Triassic. The geology of central Europe, 2: 749–821.

Ferry, J.M., Passey, B.H., Vasconcelos, C. and Eiler, J.M., 2011. Formation of dolomite at 40–80 °C in the Latemar carbonate buildup, Dolomites, Italy, from clumped isotope thermometry. Geology, 39(6): 571–574.

Folk, R.L., 1959. Practical petrographic classification of limestones. AAPG Bulletin, 43(1): 1–38.

Folk, R.L., 1965. Some aspects of recrystallization in ancient limestones. In: L.C. Pray and R.C. Murray (Editors), Dolomitization and Limestone Diagenesis. SEPM, Tulsa, pp. 14–48.

Garaguly, I., Varga, A., Raucsik, B., Schubert, F., Czuppon, G. and Frei, R., 2018. Pervasive early diagenetic dolomitization, subsequent hydrothermal alteration, and late stage hydrocarbon accumulation in a Middle Triassic carbonate sequence (Szeged Basin, SE Hungary). Marine and Petroleum Geology, 98: 270–290.

Gat, J.R. and Gat, J.R., 1978. Isotope hydrology of inland sabkhas in the Bardawil area, Sinai. Limnology and Oceanography, 23(5): 841–850.

Ghosh, P., Adkins, J., Affek, H., Balta, B., Guo, W., Schauble, E.A., Schrag, D. and Eiler, J.M., 2006. 13C–18O bonds in carbonate minerals: A new kind of paleothermometer. Geochimica et Cosmochimica Acta, 70(6): 1439–1456.

Götz, A.E., Török, Á., Feist-Burkhardt, S. and Konrád, G., 2003. Palynofacies patterns of Middle Triassic ramp deposits (Mecsek Mts., S Hungary): a powerful tool for high-resolution sequence stratigraphy. Mitt. Ges. Geol. Bergbaustud. Österr, 46: 77–90.

Götz, A.E. and Török, Á., 2008. Correlation of Tethyan and Peri–Tethyan long–term and high–frequency eustatic signals (Anisian, Middle Triassic). Geologica Carpathica, 59(4): 307–317.

Gregg, J.M., Bish, D.L., Kaczmarek, S.E. and Machel, H.G., 2015. Mineralogy, nucleation and growth of dolomite in the laboratory and sedimentary environment: A review. Sedimentology, 62(6): 1749–1769.

Gregg, J.M., Howard, S.A. and Mazzullo, S., 1992. Early diagenetic recrystallization of Holocene (< 3000 years old) peritidal dolomites, Ambergris Cay, Belize. Sedimentology, 39(1): 143–160.

Gregg, J.M. and Shelton, K.L., 1990. Dolomitization and dolomite neomorphism in the back reef facies of the Bonneterre and Davis formations (Cambrian), southeastern Missouri. Journal of Sedimentary Research, 60(4).

Haas, J., 2012. Geology of Hungary. Springer Science & Business Media. 244 p.

Haas, J., Budai, T., Hips, K., Konrád, G. and Török, Á., 2002. Sequence stratigraphy of Triassic facies areas in Hungary. Földtani Közlöny, 132(1): 17–43.

Haas, J., Budai, T. and Raucsik, B., 2012. Climatic controls on sedimentary environments in the Triassic of the Transdanubian Range (Western Hungary). Paleogeography, Paleoclimatology, Paleoecology, 353: 31–44.

Haas, J., Hips, K., Budai, T., Győri, O., Lukoczki, G., Kele, S., Demény, A. and Poros, Z., 2017. Processes and controlling factors of polygenetic dolomite formation in the Transdanubian Range, Hungary: a synopsis. International Journal of Earth Sciences, 106(3): 991–1021.

Haas, J., Kovács, S. and Török, Á., 1995. Early Alpine Shelf Evolution in the Hungarian Segments of the Tethys Margin. Acta Geologica Hungarica, 38(2): 95–110.

Haas, J. and Péró, C., 2004. Mesozoic evolution of the Tisza Mega–unit. International Journal of Earth Sciences, 93(2): 297–313.

Harangi, S., Szabó, C., Józsa, S., Szoldán, Z., Árva-Śos, E., Balla, M. and Kubovics, I., 1996. Mesozoic igneous suites in Hungary: Implications for genesis and tectonic setting in the northwestern part of Tethys. International Geology Review, 38(4): 336–360.

Hardie, L.A., 1987. Dolomitization; a critical view of some current views. Journal of Sedimentary Research, 57(1): 166–183.

Hauck, T.E., Corlett, H.J., Grobe, M., Walton, E.L. and Sansjofre, P., 2018. Meteoric diagenesis and dedolomite fabrics in precursor primary dolomicrite in a mixed carbonate–evaporite system. Sedimentology, 65(6): 1827–1858.

Hirani, J., Bastesen, E., Boyce, A., Corlett, H., Gawthorpe, R., Hollis, C., John, C.M., Robertson, H., Rotevatn, A. and Whitaker, F., 2018. Controls on the formation of stratabound dolostone bodies, Hammam Faraun Fault block, Gulf of Suez. Sedimentology, 65(6): 1973–2002.

Hollis, C., Bastesen, E., Boyce, A., Corlett, H., Gawthorpe, R., Hirani, J., Rotevatn, A. and Whitaker, F., 2017. Fault–controlled dolomitization in a rift basin. Geology, 45(3): 219–222.

Honlet, R., Gasparrini, M., Muchez, P., Swennen, R. and John, Cédric M., 2018. A new approach to geobarometry by combining fluid inclusion and clumped isotope thermometry in hydrothermal carbonates. Terra Nova, 30(3): 199–206.

Horita, J., 2014. Oxygen and carbon isotope fractionation in the system dolomite–water–CO_2 to elevated temperatures. Geochimica et Cosmochimica Acta, 129: 111–124.

Jáger, V., Molnár, F., Buchs, D. and Koděra, P., 2012. The connection between iron ore formations and "mud-shrimp" colonizations around sunken wood debris and hydrothermal sediments in a Lower Cretaceous continental rift basin, Mecsek Mts., Hungary. Earth-Science Reviews, 114(3): 250–278.

Jáger, V., 2015. Hydrothermal processes and ore indication related to the Early Cretaceous volcanism in the Eastern Mecsek Mts., PhD Dissertation, Eötvös Loránd University, Budapest, 164 p.

Jones, G.D., Smart, P.L., Whitaker, F.F., Rostron, B.J. and Machel, H.G., 2003. Numerical modeling of reflux dolomitization in the Grosmont platform complex (Upper Devonian), Western Canada sedimentary basin. AAPG bulletin, 87(8): 1273–1298.

Jones, G.D., Whitaker, F.F., Smart, P.L. and Sanford, W.E., 2004. Numerical analysis of seawater circulation in carbonate platforms: II. The dynamic interaction between geothermal and brine reflux circulation. American Journal of Science, 304(3): 250–284.

Kaczmarek, S.E., Gregg, J.M., Bish, D.L., Machel, H.G. and Fouke, B.W., 2018. Dolomite, Very High–Magnesium Calcite, and Microbes—Implications for the Microbial Model of Dolomitization. In: A.J. MacNeil, J. Lonnee and R. Wood (Editors), Characterization and Modeling of Carbonates – Mountjoy Symposium 1. Special Publication. SEPM, Tulsa, pp. 7–20.

Koltai, G., Spötl, C., Shen, C.C., Wu, C.C., Rao, Z., Palcsu, L., Kele, S., Surányi, G. and Bárány-Kevei, I., 2017. A penultimate glacial climate record from southern Hungary. Journal of Quaternary Science, 32(7): 946–956.

Konrád, G., 1998. Synsedimentary tectonic events in the Middle Triassic evolution of the SE Transdanubian part of the Tisza Unit. Acta Geologica Hungarica, 41(3): 327–341.

Korte, C., Kozur, H.W., Bruckschen, P. and Veizer, J., 2003. Strontium isotope evolution of Late Permian and Triassic seawater. Geochimica et Cosmochimica Acta, 67(1): 47–62.

Korte, C., Kozur, H.W. and Veizer, J., 2005. δ 13 C and δ 18 O values of Triassic brachiopods and carbonate rocks as proxies for coeval seawater and palaeotemperature. Palaeogeography, Palaeoclimatology, Palaeoecology, 226(3): 287–306.

Kupecz, J. and Land, L., 1994. Progressive recrystallization and stabilization of early–stage dolomite: Lower Ordovician Ellenburger Group, west Texas. Dolomites: A volume in Honour of Dolomieu. B. Purser, M., Tucker, D. Zenger (eds.). International Association of Sedimentology Special Publication (21): 255–279.

Land, L.S., 1980. The Isotopic and Trace Element Geochemistry of Dolomite: The State of the Art. In: D.H. Zenger, J.B. Dunham and R.L. Ethington (Editors), Concepts and Models of Dolomitization. SEPM Special Publication (28): 87–110.

Land, L.S., 1985. The origin of massive dolomite. Journal of Geological Education, 33(2): 112–125.

Lawson, M., Shenton, B.J., Stolper, D.A., Eiler, J.M., Rasbury, E.T., Becker, T.P., Phillips-Lander, C.M., Buono, A.S., Becker, S.P., Pottorf, R., Gray, G.G., Yurewicz, D. and Gournay, J., 2018. Deciphering the diagenetic history of the El Abra Formation of eastern

Mexico using reordered clumped isotope temperatures and U-Pb dating. GSA Bulletin, 130(3-4): 617–629.

Lohmann, K.C., 1988. Geochemical Patterns of Meteoric Diagenetic Systems and Their Application to Studies of Paleokarst. In: N.P. James and P.W. Choquette (Editors), Paleokarst. Springer New York, New York, NY, pp. 58–80.

Lonnee, J. and Machel, H.G., 2006. Pervasive dolomitization with subsequent hydrothermal alteration in the Clarke Lake gas field, Middle Devonian Slave Point Formation, British Columbia, Canada. AAPG bulletin, 90(11): 1739–1761.

Loyd, S.J., Corsetti, F.A., Eagle, R.A., Hagadorn, J.W., Shen, Y., Zhang, X., Bonifacie, M. and Tripati, A.K., 2015. Evolution of Neoproterozoic Wonoka–Shuram Anomaly-aged carbonates: Evidence from clumped isotope paleothermometry. Precambrian Research, 264: 179–191.

Lukoczki, G., Budai, T. and Németh, T., 2015. Sideritic-kaolinitic and green clay layers in the Mecsek Mountains (SW Hungary): Indicators of Middle Triassic volcanism—Myth or reality? Central European Geology, 58(4): 334–355.

MacDonald, J.M., John, C.M. and Girard, J.-P., 2018. Testing clumped isotopes as a reservoir characterization tool: a comparison with fluid inclusions in a dolomitized sedimentary carbonate reservoir buried to 2–4 km. Geological Society, London, Special Publications, 468: 189–202.

Machel, H.G., 1990. Bulk solution disequilibrium in aqueous fluids as exemplified by diagenetic carbonates. In: I.D. Meshri and P.J. Ortoleva (Editors), Prediction of Reservoir Quality through Chemical Modeling. AAPG, Tulsa, pp. 71–83.

Machel, H.G., 1997. Recrystallization versus neomorphism, and the concept of 'significant recrystallization' in dolomite research. Sedimentary Geology, 113(3): 161–168.

Machel, H.G., 1999. Effects of groundwater flow on mineral diagenesis, with emphasis on carbonate aquifers. Hydrogeology Journal, 7(1): 94–107.

Machel, H.G., 2004. Concepts and models of dolomitization: a critical reappraisal. Geological Society, London, Special Publications, 235(1): 7–63.

Machel, H.G. and Burton, E.A., 1991. Factors governing cathodoluminescence in calcite and dolomite, and their implications for studies of carbonate diagenesis. In: C.E. Barker and O.C. Kopp (Editors), Luminescence Microscopy: Quantitative and Qualitative Aspects. SEPM, Tulsa, pp. 37–58.

Machel, H.G. and Buschkuehle, B.E., 2008. Diagenesis of the Devonian Southesk–Cairn Carbonate Complex, Alberta, Canada: marine cementation, burial dolomitization, thermochemical sulfate reduction, anhydritization, and squeegee fluid flow. Journal of Sedimentary Research, 78(5): 366–389.

Machel, H.G., Cavell, P.A. and Patey, K.S., 1996. Isotopic evidence for carbonate cementation and recrystallization, and for tectonic expulsion of fluids into the Western Canada Sedimentary Basin. GSA Bulletin, 108(9): 1108–1119.

Machel, H.G. and Lonnee, J., 2002. Hydrothermal dolomite—A product of poor definition and imagination. Sedimentary geology, 152(3): 163–171.

Magyar, I., Geary, D.H. and Müller, P., 1999. Paleogeographic evolution of the Late Miocene Lake Pannon in Central Europe. Paleogeography, Paleoclimatology, Paleoecology, 147(3): 151–167.

Major, R., Lloyd, R.M. and Lucia, F.J., 1992. Oxygen isotope composition of Holocene dolomite formed in a humid hypersaline setting. Geology, 20(7): 586–588.

Mangenot, X., Gasparrini, M., Rouchon, V. and Bonifacie, M., 2018. Basin-scale thermal and fluid flow histories revealed by carbonate clumped isotopes (Δ_{47}) – Middle Jurassic carbonates of the Paris Basin depocentre. Sedimentology, 65(1): 123–150.

Mazzullo, S.J., 1992. Geochemical and neomorphic alteration of dolomite: A review. Carbonates and Evaporites, 7(1): 21–37.

McArthur, J.M., Howarth, R.J. and Shields, G.A., 2012. Strontium isotope stratigraphy. In: F.M. Gradstein, J.G. Ogg, M. Schmitz and G. Ogg (Editors), The geologic time scale. Elsevier, pp. 127–144.

McKenzie, J.A., 1981. Holocene dolomitization of calcium carbonate sediments from the coastal sabkhas of Abu Dhabi, UAE: a stable isotope study. The Journal of Geology, 89(2): 185–198.

Millán, I.M., Machel, H. and Bernasconi, S.M., 2016. Constraining temperatures of formation and composition of dolomitizing fluids in the Upper Devonian Nisku Formation (Alberta, Canada) with clumped isotopes. Journal of Sedimentary Research, 86(1): 107–112.

Montanez, I.P. and Read, J.F., 1992. Fluid–rock interaction history during stabilization of early dolomites, upper Knox Group (Lower Ordovician), US Appalachians. Journal of Sedimentary Research, 62(5).

Nader, F.H., Swennen, R. and Ellam, R., 2004. Reflux stratabound dolostone and hydrothermal volcanism–associated dolostone: a two-stage dolomitization model (Jurassic, Lebanon). Sedimentology, 51(2): 339–360.

Nader, F.H., Swennen, R. and Keppens, E., 2008. Calcitization/dedolomitization of Jurassic dolostones (Lebanon): results from petrographic and sequential geochemical analyses. Sedimentology, 55(5): 1467–1485.

Nagy, E., 1968. The Triassic of the Mecsek Mountains. Annals of the Hungarian Geological Institute, 51, Budapest.

Némedi Varga, Z., 1983. Tectonics of the Mecsek Mountains in the Alpine orogenic cycle, Annual Report of the Hungarian Geological Institute from 1981, 467–484.

Némedi Varga, Z., 1995. The research history and economic geology of the bituminous coal in the Mecsek Mts. University of Miskolc, Miskolc, Hungary, 472 p.

Némedi Varga, Z., 1998. Jurassic stratigraphy of the Mecsek-Villány unit. In: I. Bérczi and Á. Jámbor (Editor), Stratigraphy of the geological formations of Hungary. MOL-MÁFI, Budapest, 319–336.

Poros, Z., Molnár, F., Koroknai, B., Lespinasse, M., Maros, G. and Benkó, Z., 2008. Application of studies on fluid inclusion planes and fracture systems in the reconstruction of the fracturing history of granitoid rocks III: Results of studies in drillcores from the radioactive waste depository site at Bátaapáti (Üveghuta). Földtani Közlöny, 138(4): 363–384.

Poros, Z., Machel, H.G., Mindszenty, A. and Molnár, F., 2013. Cryogenic powderization of Triassic dolostones in the Buda Hills, Hungary. International Journal of Earth Sciences, 102(5): 1513–1539.

Qing, H. and Mountjoy, E.W., 1994. Rare earth element geochemistry of dolomites in the Middle Devonian Presqu'ile barrier, Western Canada Sedimentary Basin: implications for fluid-rock ratios during dolomitization. Sedimentology, 41(4): 787–804.

Rustichelli, A., Iannace, A., Tondi, E., Di Celma, C., Cilona, A., Giorgioni, M., Parente, M., Girundo, M. and Invernizzi, C., 2017. Fault-controlled dolomite bodies as palaeotectonic indicators and geofluid reservoirs: New insights from Gargano Promontory outcrops. Sedimentology, 64(7): 1871–1900.

Sena, C.M., John, C.M., Jourdan, A.-L., Vandeginste, V. and Manning, C., 2014. Dolomitization of Lower Cretaceous Peritidal Carbonates By Modified Seawater: Constraints From Clumped Isotopic Paleothermometry, Elemental Chemistry, and Strontium Isotopes. Journal of Sedimentary Research, 84(7): 552–566.

Sibley, D.F. and Gregg, J.M., 1987. Classification of dolomite rock textures. Journal of Sedimentary Research, 57(6): 967–975.

Spötl, C. and Burns, S.J., 1991. Formation of 18O-depleted dolomite within a marine evaporitic sequence, Triassic Reichenhall Formation, Austria. Sedimentology, 38(6): 1041–1057.

Sun, S.Q., 1995. Dolomite reservoirs: porosity evolution and reservoir characteristics. AAPG bulletin, 79(2): 186–204.

Szulc, J., 2000. Middle Triassic evolution of the northern Peri–Tethys area as influenced by early opening of the Tethys Ocean, Annales Societatis Geologorum Poloniae, 1–48.

Török, Á., 1998a. Controls on development of Mid–Triassic ramps: examples from southern Hungary. Geological Society, London, Special Publications, 149(1): 339–367.

Török, Á., 1998b. Triassic stratigraphy of the Mecsek–Villány unit. In: I. Bérczi and Á. Jámbor (Editors), Stratigraphy of the geological formations of Hungary. MOL–MÁFI, Budapest, pp. 253–280.

Török, Á., 2000a. Muschelkalk carbonates in southern Hungary: an overview and comparison to German Muschelkalk. Zbl. Geol. Paläont. Teil I(9–10): 1085–1103.

Török, Á., 2000b. Formation of dolomite mottling in Middle Triassic ramp carbonates (Southern Hungary). Sedimentary Geology, 131(3): 131–145.

Vető, I., 1978. Reconstruction of the thermal genesis of dispersed hydrocarbons. Application of the method in the Hungarian hydrocarbon research. PhD Dissertation, Hungarian Academy of Sciences, Budapest, 66 p.

Viczián, I., 1995. Clay minerals in Mesozoic and Paleogene sedimentary rocks of Hungary. Romanian Journal of Mineralogy, 77: 35–44.

Wanless, H.R., 1979. Limestone response to stress; pressure solution and dolomitization. Journal of Sedimentary Research, 49(2): 437–462.

Wéber, B., 1978. Neuer Beitrag zur Kenntnis der anisischen und ladinischen Schichten des Mecsek–Gebirges. Földtani Közlöny, 108: 137–148.

Wéber, B., 1982. On the Neogene and Paleogene of the Mecsekalja Graben (S Hungary). Földtani Közlöny, 112(3): 209–240.

Wilson, M.E.J., Evans, M.J., Oxtoby, N.H., Nas, D.S., Donnelly, T. and Thirlwall, M., 2007. Reservoir quality, textural evolution, and origin of fault-associated dolomites. AAPG Bulletin, 91(9): 1247–1272.

Wright, W.R., 2001. Dolomitization, fluid–flow and mineralization of the Lower Carboniferous rocks of the Irish Midlands and Dublin Basin, University College Dublin, Belfield, Ireland.

Tables

Table 1: Description of sampling locations with abbreviations (Location ID) used throughout the text.

Location ID	Name	Description
AT	Árpád-tető	Partially to completely dolomitized Middle Triassic limestones exposed in an abandoned quarry, and in a road-cut (Kozár Limestone Member?)
GF-1	Gálosfa-1	Kán Dolomite Member cored by the Gf-1 borehole between 910.4 m to 1195.5 m
HR	Hetvehely road-cut	Uppermost part of the Zuhánya Limestone, and lower part of the Kán Dolomite exposed in a road-cut near the town of Hetvehely
MR	Misina road-cut	Kozár Limestone exposed in a road-cut leading up to the TV tower located on Misina-tető
RV	Rák Valley	Parts of the Kán Dolomite Member exposed in the Rák Valley near the town of Gorica
VA	Váralja	Middle Triassic fine to coarse crystalline dolomites exposed in an abandoned quarry near the town of Váralja in the area of the Northern Imbricates
VP-2	Vágotpuszta-2	Irregular alternation of very fine and medium to coarse crystalline dolomites in the core section between 79 and 188 m, Kán Dolomite Member

Table 2: List of geochemical analytical results. CAL: calcite cement, LMST: limestone, MC: medium to coarse crystalline matrix dolomite, SD: saddle dolomite, VF: very fine to fine crystalline matrix dolomite.

Sample ID	**$\delta^{18}O$ (‰ V-PDB)**	**$\delta^{13}C$ (‰ V-PDB)**	**Type**	**$^{87}Sr/^{86}Sr$**	**Δ_{47} (‰)**		**T (°C)**			**$\delta^{18}O_{fluid}$ (‰ V-SMOW)**
					mean	**SE**	**mean**	**min.**	**max.**	
AT NKF 1	–2.2	3.8	MC	0.70781						
AT NKF 3	–8.4	0.3	LMST	0.70798						
AT NKF 4	–8.9	2.7	MC							
AT NKF 6	–7.8	1.7	LMST							
AT UB 1	–6.6	3.4	MC							
AT UB 2	–7.8	2.5	SD							
AT UB 5a	–12.1	2.0	SD	0.70794						
AT UB 5a	–11.2	1.5	MC							
AT UB 5a	–10.9	0.6	SD							
GF-1 910.4 m	–6.2	2.4	MC							
GF-1 911.8 m	–5.3	2.6	MC							
GF-1 913.3	–5.1	2.5	VF							
GF-1 918.2 m 01	–5.6	2.2	MC							
GF-1 918.2 m 02	–6.7	2.4	MC							
GF-1 921.8 m	–5.8	2.6	MC							
GF-1 926.6 m	–8.0	2.2	MC							
GF-1 934.2 m	–4.7	2.3	VF							
GF-1 943.6 m	–3.5	2.9	VF							
GF-1 954.6 m	–8.4	2.3	VF							
GF-1 957.3 m	–6.9	2.1	MC							
GF-1 957.9 m 01	–7.4	1.8	MC							
GF-1 957.9 m 02	–7.4	1.8	MC							
GF-1 961.4 m	–4.9	1.7	VF							
GF-1 965.6 m 01	–5.0	2.1	VF							
GF-1 965.6 m 02	–7.7	1.8	MC							
GF-1 965.6 03	–7.8	1.0	MC							
GF-1 965.8 m	–3.4	1.9	VF							
GF-1 966.2 m	–3.8	1.4	VF							
GF-1 972 m	–2.4	2.3	VF							
GF-1 981.5 m	–2.8	2.9	VF							
GF-1 982 m	–3.9	2.6	VF							
GF-1 982.9 m	–2.9	1.9	VF							
GF-1 988.3 m	–2.6	1.8	VF							

GF-1 992 m	–4.5	1.9	VF							
GF-1 998 m	–4.0	1.7	VF							
GF-1 1002 m	–4.9	2.3	VF							
GF-1 1017 m	–6.7	2.6	MC							
GF-1 1032.3 m	–2.3	2.2	VF							
GF-1 1055 m	–4.1	2.1	VF	0.70819	0.576	0.005	67	64	69	2.6
GF-1 1109 m 01	–2.8	2.4	VF							
GF-1 1109 m 02	–2.7	2.6	VF							
GF-1 1147 m	–2.2	1.1	VF							
GF-1 1181.5 m	–12.4	-0.3	CAL							
GF-1 1195.5 m 01	–8.6	2.4	MC							
HR-HH 01	–8.5	2.5	MC							
HR-HH 03	–10.5	2.4	MC							
HR-HH 04	–6.3	3.0	MC							
HR-HH 08/1	–12.5	2.3	SD							
HR-HH 08/2	–12.6	2.1	MC	0.70797	0.482	0.007	127	121	132	1.3
HR-HH 18/1	–10.2	2.4	MC							
HR-HH 18/2	–10.4	2.2	MC		0.501	0.01	112	105	119	2.6
HR-HH 21 -01	–7.5	–8.2	CAL							
HR-HH 21 -02	–8.8	3.5	SD							
HR-HH 22	–4.9	2.7	VF							
HR-HH 26	–3.8	2.5	VF	0.70815	0.575	0.005	67	65	70	3.0
HR-HH 26 - H1	–4.5	2.7	VF							
HR-HH 2/1	–7.7	4.2	MC	0.70785						
HR-HH 2/2	–6.3	2.7	MC							
MR-DKA 01	–9.9	0.2	LMST							
MR-DKA 02	–7.2	2.2	LMST							
MR-DKA 03	–8.2	1.8	LMST							
MR-DKA 04	–7.4	1.6	LMST							
MR-DKA 05	–8.9	–2.2	LMST							
MR-DKA 06	–8.4	–1.3	LMST							
MR-DKA 07	–9.0	-1.5	LMST							
MR-DKA 08	–10.5	–0.9	SD							
MR-DKA 08	–8.8	–1.6	LMST							
MR-DKA 09	–9.0	–0.9	LMST							
MR-DKA 10	–9.2	–2.7	LMST							
MR-DKA 11	–8.4	–1.2	LMST							
MR-DKA 12	–8.8	–1.1	LMST							
MR-DKA 13	–9.6	–1.7	LMST							
MR-DKA 14	–8.9	0.1	LMST							
MR-DKA 15	–9.0	–3.3	LMST	0.70802						
RV-GO-1/1	–7.8	–8.5	CAL							

RV-GO-3/1	–3.2	1.9	VF							
RV 2	–7.2	3.2	MC							
VA 03 -01	–5.5	2.7	MC							
VA 03 -02	–10.3	0.8	SD							
VA 06	–6.5	2.4	MC							
VA 07	–10.1	1.5	MC		0.478	0.007	130	124	136	4.3
VA 09	–4.9	1.4	VF							
VA 10	–20.5	-0.9	CAL							
VA 2T/1	–13.0	0.3	SD							
VA 2T/2	–7.2	2.0	MC							
VA 3T/1	–7.5	2.4	MC	0.70780						
VA 3T/2	–15.4	1.1	SD	0.70823						
VP-2 79.3 m U1	–7.7	2.2	MC							
VP-2 79.3 m U2	–6.2	2.5	SD							
VP-2 79.3 m L	–5.3	2.3	MC							
VP-2 83.2 m	–10.3	0.1	MC	0.70790	0.508	0.012	107	99	116	1.7
VP-2 97.2 m	–9.2	1.1	MC							
VP-2 98.7 m	–6.5	0.9	MC							
VP-2 99.6 m 01	–3.2	0.4	VF							
VP-2 99.6 m 02	–10.0	1.2	SD							
VP-2 119 m 01	–6.2	–4.8	CAL							
VP-2 119 m 02	–9.0	2.6	SD							
VP-2 125.4 m	–9.4	0.9	SD							
VP-2 154.2 m	–2.0	2.4	VF	0.70813	0.611	0.006	50	48	53	2.0
VP-2 160.3 m 01	–4.2	2.5	VF							
VP-2 160.3 m 02	–7.5	3.7	SD							

Figures

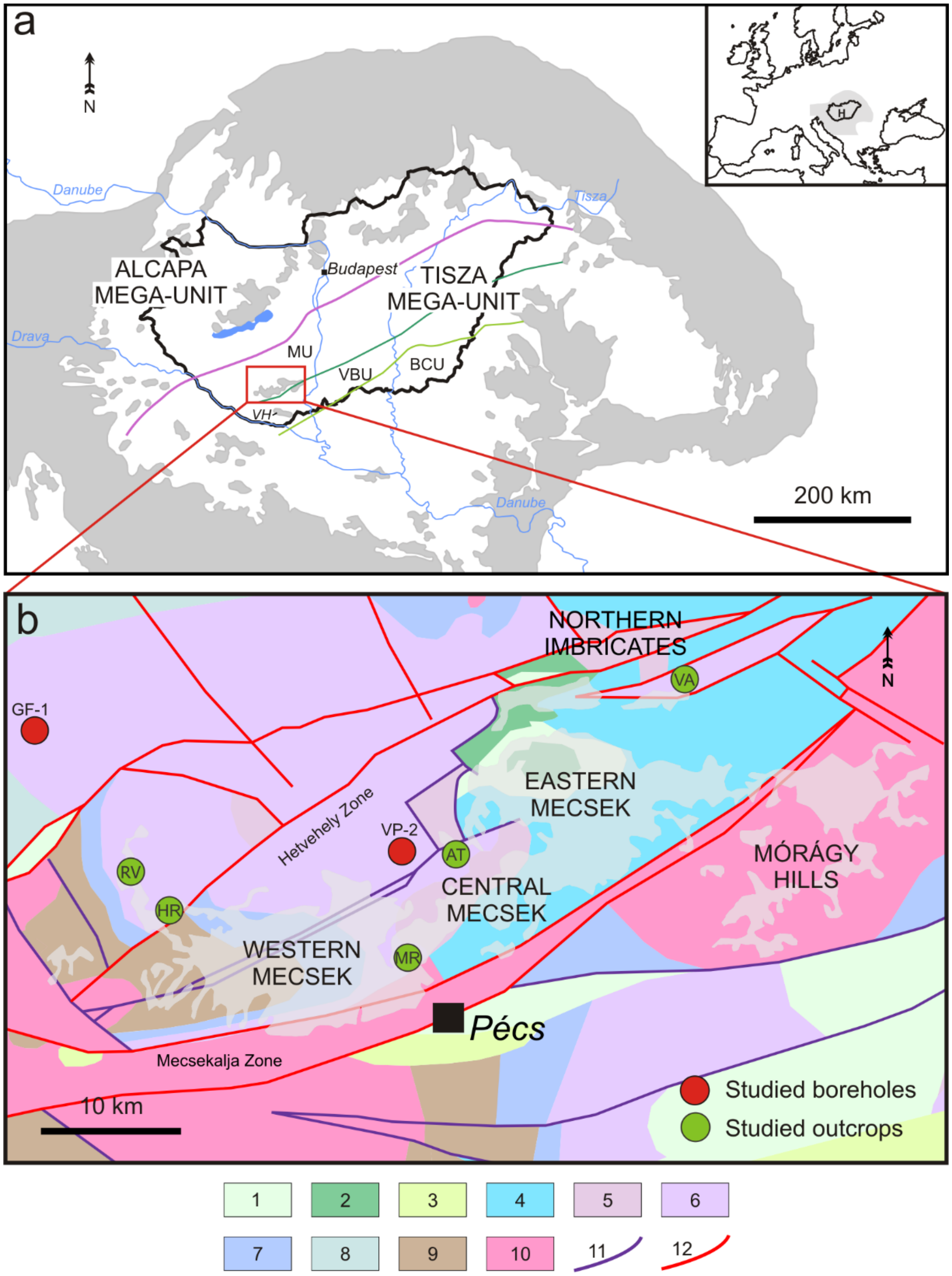

Fig. 1: Location of the study area. **(a)** The study area is situated in SW Hungary as indicated by the red rectangle. The purple line is the Mid-Hungarian Fault Zone. The green lines mark the

boundaries between the subunits of the Tisza Mega-Unit. MU: Mecsek Unit, VBU: Villány-Bihor Unit, BCU: Békés-Codru Unit (modified after Csontos et al., 1992). Grey shading indicates outcrops of Pre-Neogene formations (VH: Villány Hills). The inset shows the location of the Pannonian Basin and Hungary within Europe. **(b)** Simplified geological map of the study area showing the sampling locations (Cenozoic cover not shown). Shaded areas indicate outcrops of Pre-Cenozoic formations (modified after Haas, 2012). AT: Árpád-tető, GF-1: Gálosfa-1, HR: Hetvehely road-cut, MR: Misina road-cut, RV: Rák Valley, VA: Váralja quarry, VP-2: Vágotpuszta-2. Legend: 1: Upper Cretaceous continental and marine formations, 2: Lower Cretaceous volcanic rocks, 3: Middle Jurassic to Lower Cretaceous pelagic limestones, 4: Lower and Middle Jurassic siliciclastic formations, 5: Upper Triassic to Lower Jurassic coal-bearing siliciclastic formations, 6: Middle Triassic shallow marine siliciclastic and carbonate formations, 7: Lower Triassic siliciclastic formations, 8: Mesozoic rocks in general, 9: Permian and Upper Carboniferous continental siliciclastic formations, 10: Paleozoic crystalline rocks, 11: Mesozoic fault lines, 12: Cenozoic fault lines.

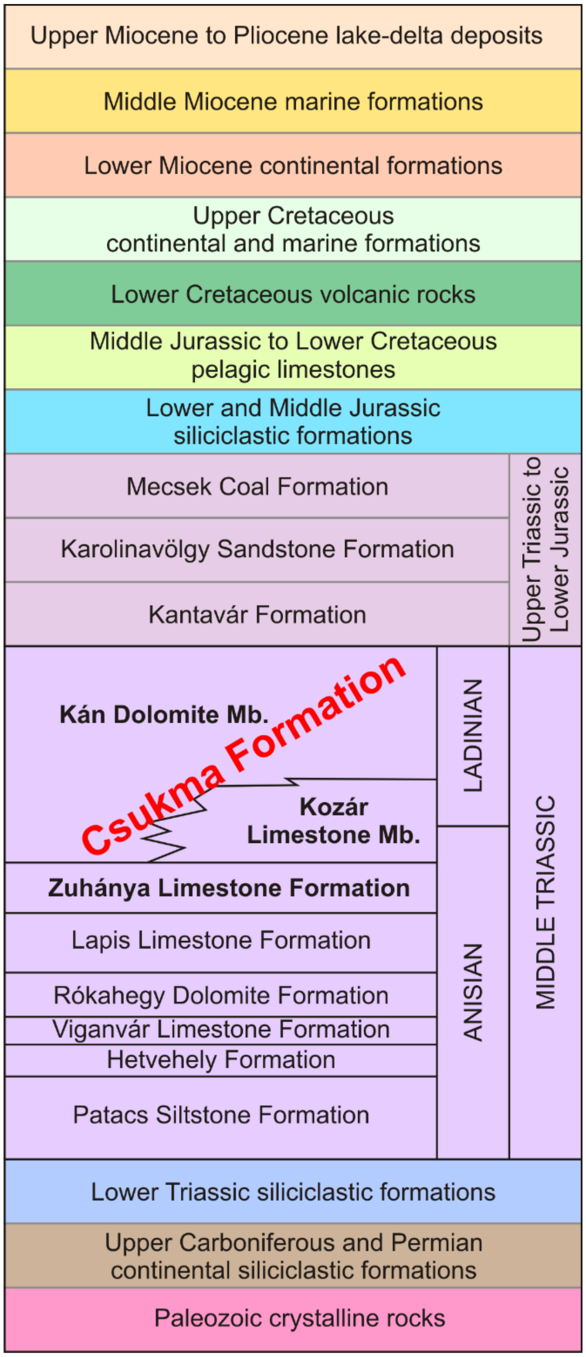

Fig. 2: Simplified stratigraphic column of the area of the Mecsek Mts. with emphasis on the Middle and Upper Triassic formations. The names of the studied formations are highlighted in bold (after Haas, 2012).

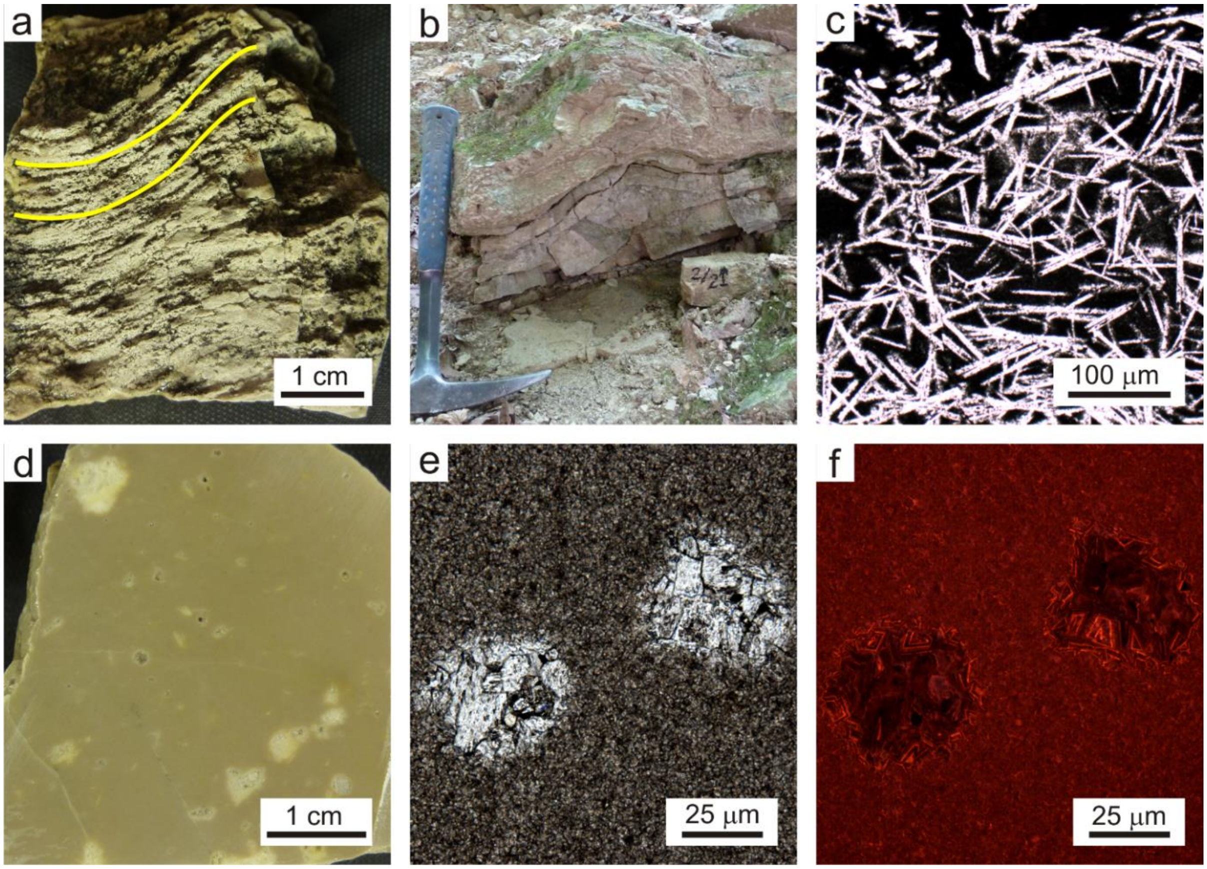

Fig. 3: Sedimentary and petrographic features of the fine to very fine crystalline dolomites. **(a)** Hand specimen of a very fine crystalline laminated dolomite. Yellow lines highlight curved lamination of uncertain origin. (Location HR) **(b)** Outcrop photograph of a teepee structure in very fine crystalline dolomite. (Location RV) **(c)** Photomicrograph of quartz pseudomorphs after gypsum encased in very fine crystalline dolomite. Plane-polarized light. (Location GF-1) **(d)** Hand specimen of very fine crystalline dolomite containing molds filled with planar dolomite. (Location HR) **(e)** Photomicrograph of very fine crystalline dolomite with dolomite-filled molds. Plane-polarized light. (Location HR) **(f)** CL image of (e) showing CL zonation of the dolomite cement.

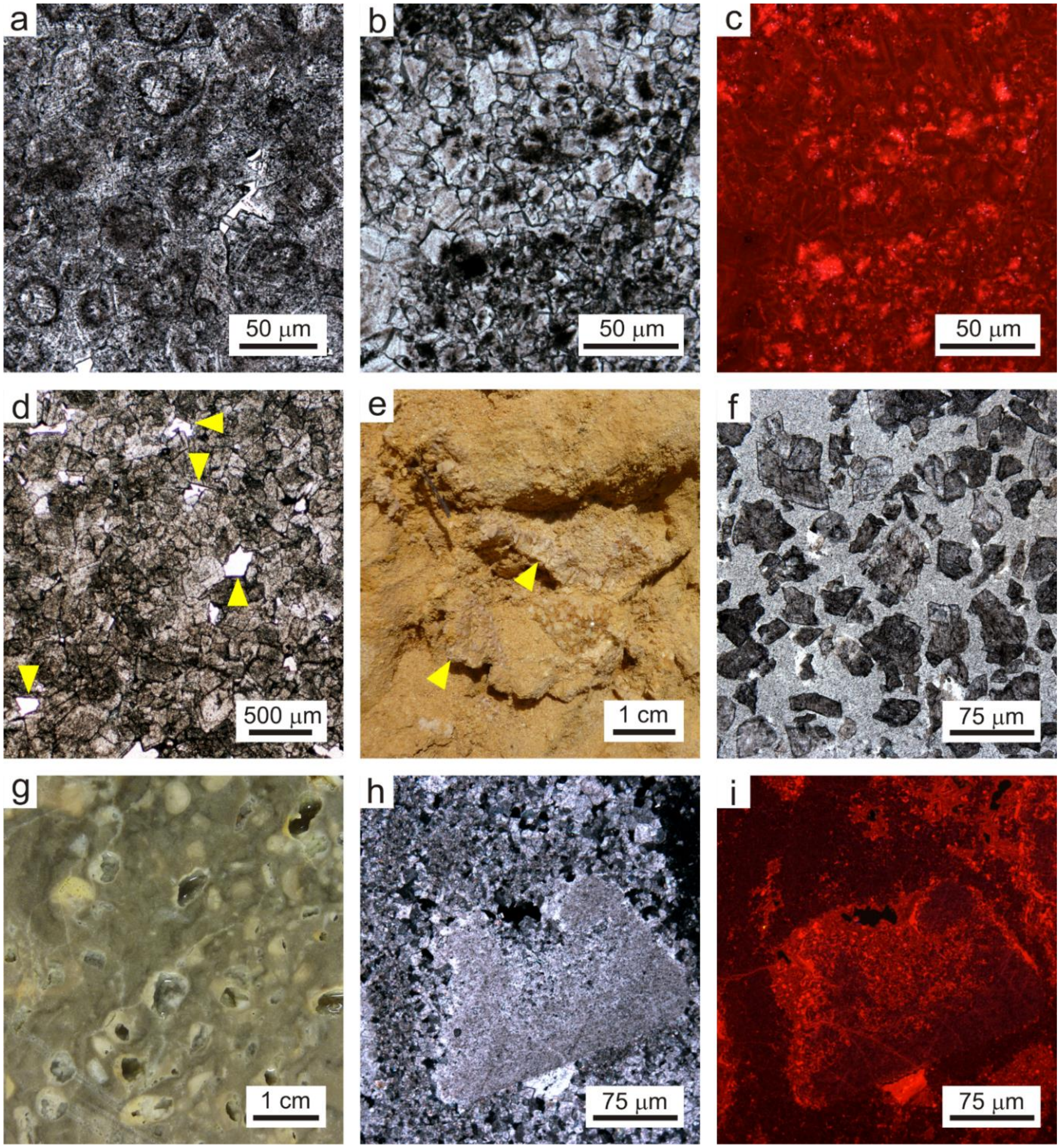

Fig. 4: Petrographic features of the medium to very coarse crystalline dolomites. **(a)** Photomicrograph of a medium crystalline, planar-s dolomite with micritic ghosts likely indicating an ooid grainstone/packstone precursor. (Location HR) **(b)** Photomicrograph of medium crystalline dolomite with cloudy core–clear rim fabric. Plane-polarized light. (Location AT) **(c)** CL image of (b) showing the mottled core and zoned rims corresponding to the cloudy cores and

clear rims, respectively. **(d)** Photomicrograph of a coarse crystalline, planar-s dolomite. Yellow arrows point to intercrystal pores. Plane-polarized light. (Location HR) **(e)** Outcrop photograph of coarse crystalline friable dolomite. Yellow arrows point to vug-filling saddle dolomite more resistant to disintegration. (Location HR) **(f)** Photomicrograph of grain mount of nonplanar dolomite crystals of the friable coarse crystalline dolomite. Plain polarized light. (Location HR) **(g)** Hand specimen of a fine to coarse crystalline dolomite with bioclastic floatstone fabric. (Location VA) **(h)** Photomicrograph of an echinoid fragment within a fine to medium crystalline planar-s to nonplanar dolomite. Cross-polarized light. (Location VA) **(i)** CL image of (h) revealing textural difference between the finer crystalline dolomite (very dull) and the coarser crystalline dolomite (brighter red, zoned or mottled CL pattern).

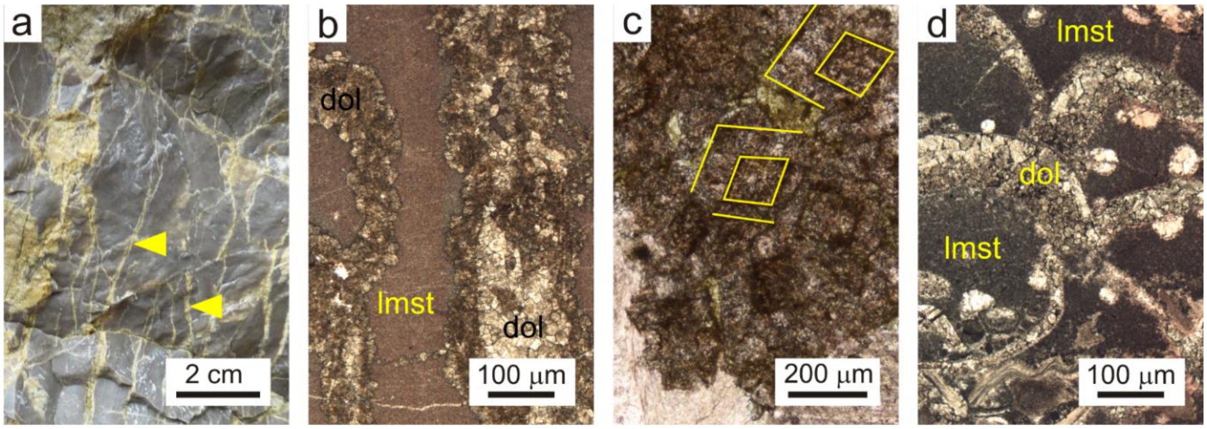

Fig. 5: Petrographic features of the dolomitic limestones. **(a)** Outcrop photograph of dark grey mudstone with ochre replacive dolomite along joints and fractures (yellow arrows). (Location AT) **(b)** Photomicrograph of fine to medium crystalline, nonplanar to planar-s dolomite (dol) partially replacing a mudstone (pink, lmst). Stained thin section, plane-polarized light. (Location AT) **(c)** Photomicrograph of calcite pseudomorphs after dolomite (dedolomite) within a bioclastic grainstone. Original dolomite mineralogy is inferred based on the dark, likely iron hydroxide-bearing zones mimicking the shape of dolomite crystals. Some of these zones are highlighted by yellow lines. Stained thin section. Plane-polarized light. (Location MR) **(d)** Photomicrograph of a dolomitic limestone. Bivalve (?) shell fragments are non-mimetically replaced by medium to coarse crystalline nonplanar dolomite (dol). Plane-polarized light. Right side of the thin section is stained. (Location HR)

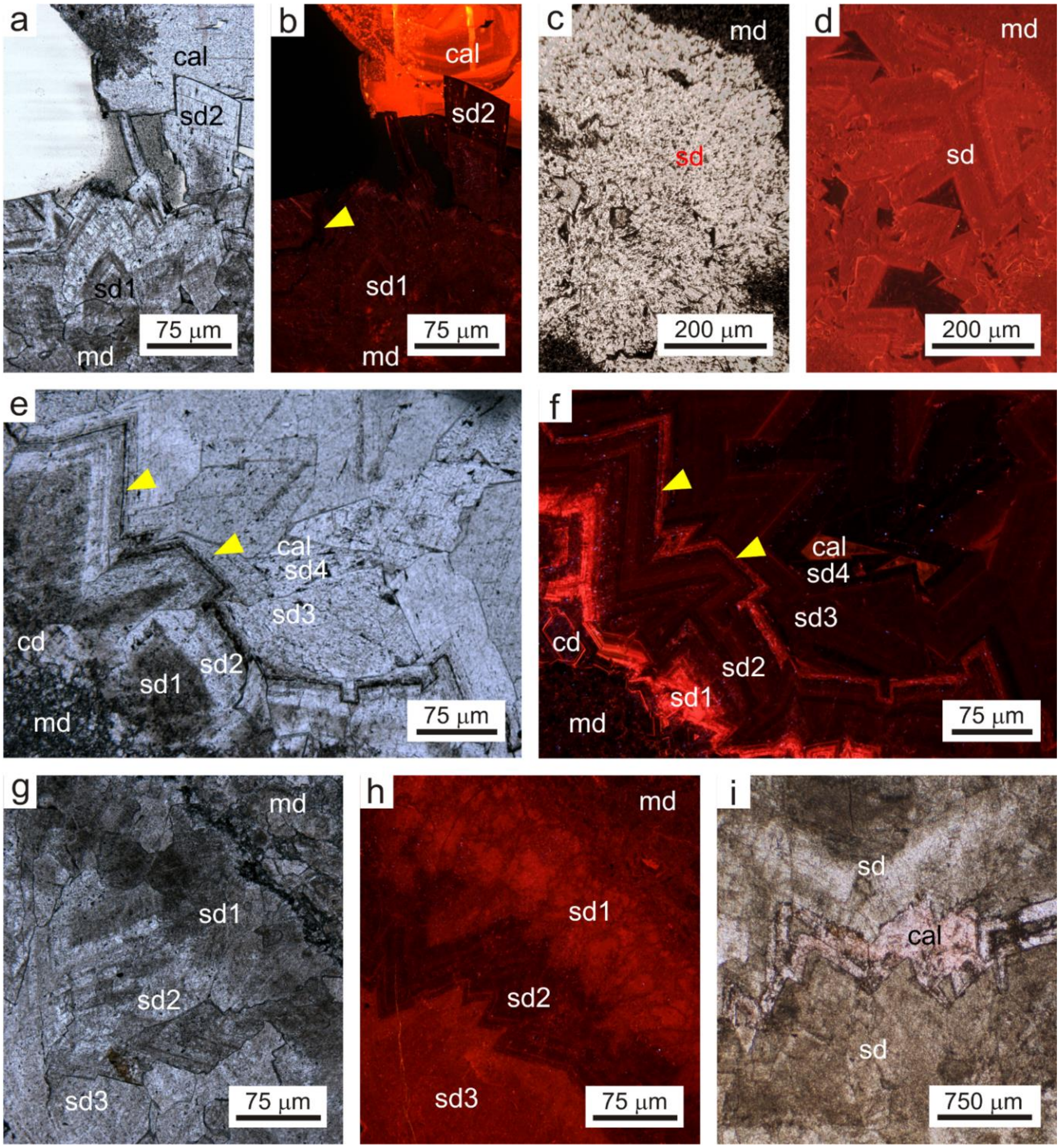

Fig. 6: Petrographic features representing a variety in saddle dolomite cements as found across the studied sedimentary succession. The numbers indicate paragenetic sequence within a given sample and do not correlate across samples. **(a)** Saddle dolomite cement with inclusion-rich zones (sd1) or clear (sd2) overgrowth filling a vug in coarse crystalline planar-s to nonplanar-a matrix dolomite (md). Final cement in the pore is calcite (cal). Plane-polarized light. (Location GF-1) **(b)**

CL image of (a). The first saddle dolomite (sd1) with dull, mottled CL is cross-cut (arrow) and overgrown by a later saddle dolomite phase (sd2) with duller CL. The calcite (cal) displays complex bright and dull orange CL zonation. **(c)** Saddle dolomite cement (sd) filling a vug in very fine crystalline matrix dolomite (md). **(d)** CL image of (c). The saddle dolomite cement displays bright red concentric CL zonation. The final dolomite phase is nonluminescent. (Location GF-1) **(e)** Fracture-filling saddle dolomite cement. (Location VP-2) **(f)** CL image of (e). The saddle dolomite cement displays simple concentric and oscillatory concentric zonation. Non-luminescent matrix dolomite (md) is overgrown by non-luminescent to bright red planar-c dolomite cement (cd). The first generation of saddle dolomite (sd1) shows bright red simple concentric zoning. The inclusion-rich zones, best visible in (e), have mottled CL appearance. The second generation of saddle dolomite (sd2) shows oscillatory zoning of mainly non- and minor red-growth bands, capped by a brightly luminescent inclusion-rich layer (yellow arrows). Sd3 shows zonation pattern similar to sd2 but with lower intensity. The final saddle dolomite cement (sd4) is non-luminescent. Small remaining pore space was filled by dull orange luminescing calcite (cal). **(g)** Fracture-filling saddle dolomite and fractured coarse crystalline, nonplanar-a dolomite matrix dolomite (md). (Location VA) **(h)** CL image of (g). The first phase of the saddle dolomite (sd1) is inclusion-rich and is characterized by bright red mottled CL (note the microfractures cross-cutting sd1). The second phase (sd2) is less turbid in transmitted light and shows simple and/or oscillatory zonation similar to sd2 in image (f). The final saddle dolomite (sd3) is similar to sd2 in transmitted light but displays bright red, homogenous CL. **(i)** Zones of saddle dolomite cement (sd) selectively replaced by calcite (cal). The dark solid inclusions along and within the calcite are likely iron hydroxides. Stained thin section. Plane-polarized light. (Location VA)

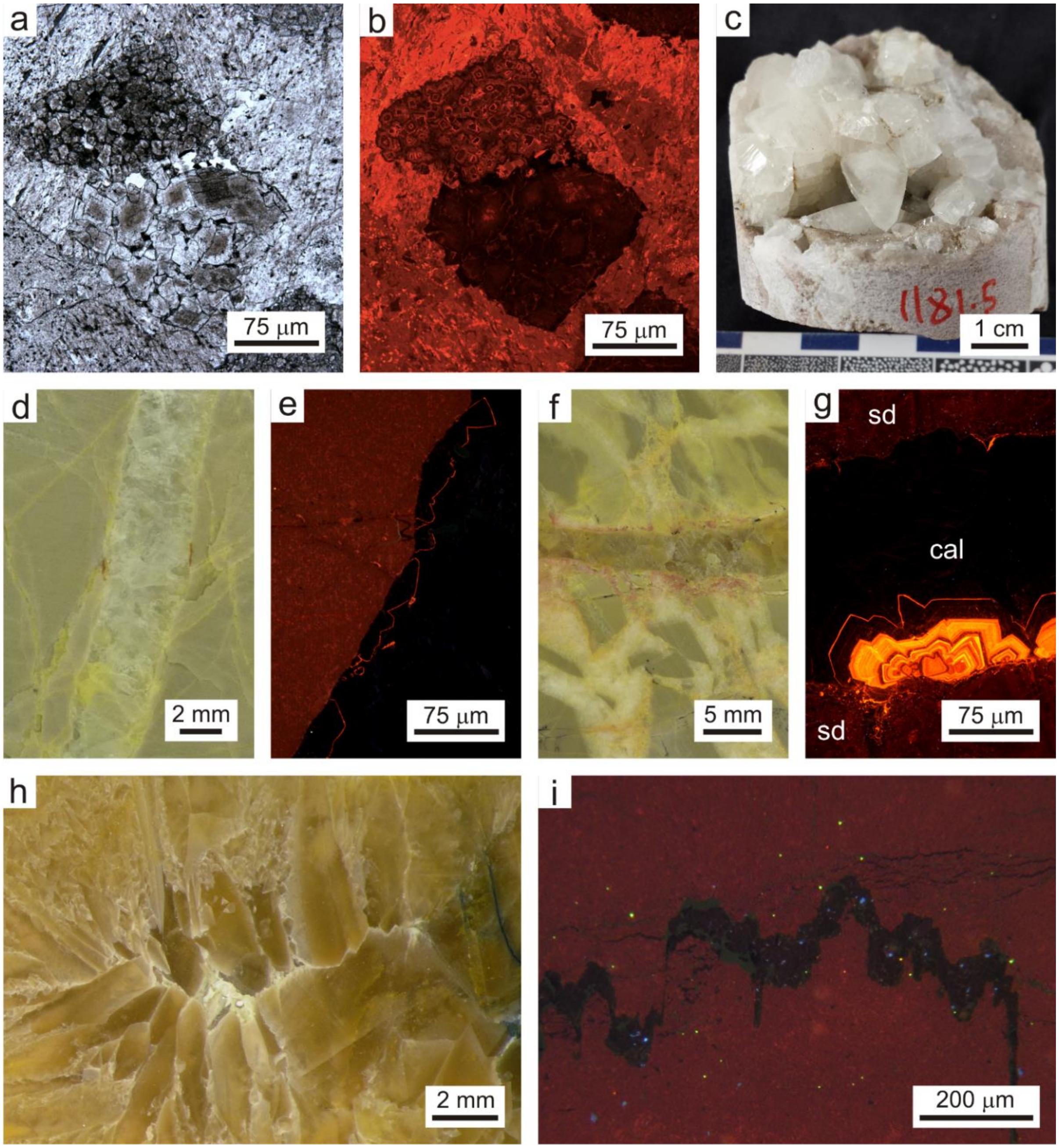

Fig. 7: Petrographic features of calcite cements. **(a)** Dolomite breccia with blocky calcite cement (CAL-2). Plane-polarized light. (Location GF-1) **(b)** CL image of (a). The blocky calcite cement displays bright orange CL. **(c)** Subhedral to euhedral, scalenohedral calcite cement in a GF-1 core sample. **(d)** Hand specimen of very fine crystalline dolomite cross-cut by whitish–transparent calcite vein. (Location VP-2) **(e)** CL photomicrograph of the sample shown in (d) displaying non-

luminescent calcite with a single thin bright orange CL zone. (Location VP-2) **(f)** Hand specimen of a dolomite breccia. Clasts are made up of very fine crystalline dolomite and the cement around the clasts is saddle dolomite. The breccia is cross-cut by a brownish calcite vein (CAL-3). (Location VP-2) **(g)** CL photomicrograph of the sample shown in (f). Dull saddle dolomite (sd) is cross-cut by a coarse crystalline, blocky calcite vein (cal). The calcite is mostly non-luminescent with bright orange/yellow oscillatory zonation likely indicating the location of nucleation. (Location VP-2) **(h)** Hand specimen of brown bladed calcite cement (CAL-3). (Location RV) **(i)** CL image of a stylolite cross-cutting a fine crystalline dolomite. The stylolite is partially filled with non-luminescent calcite. Blue and green particles are detrital silicate grains. (Location RV)

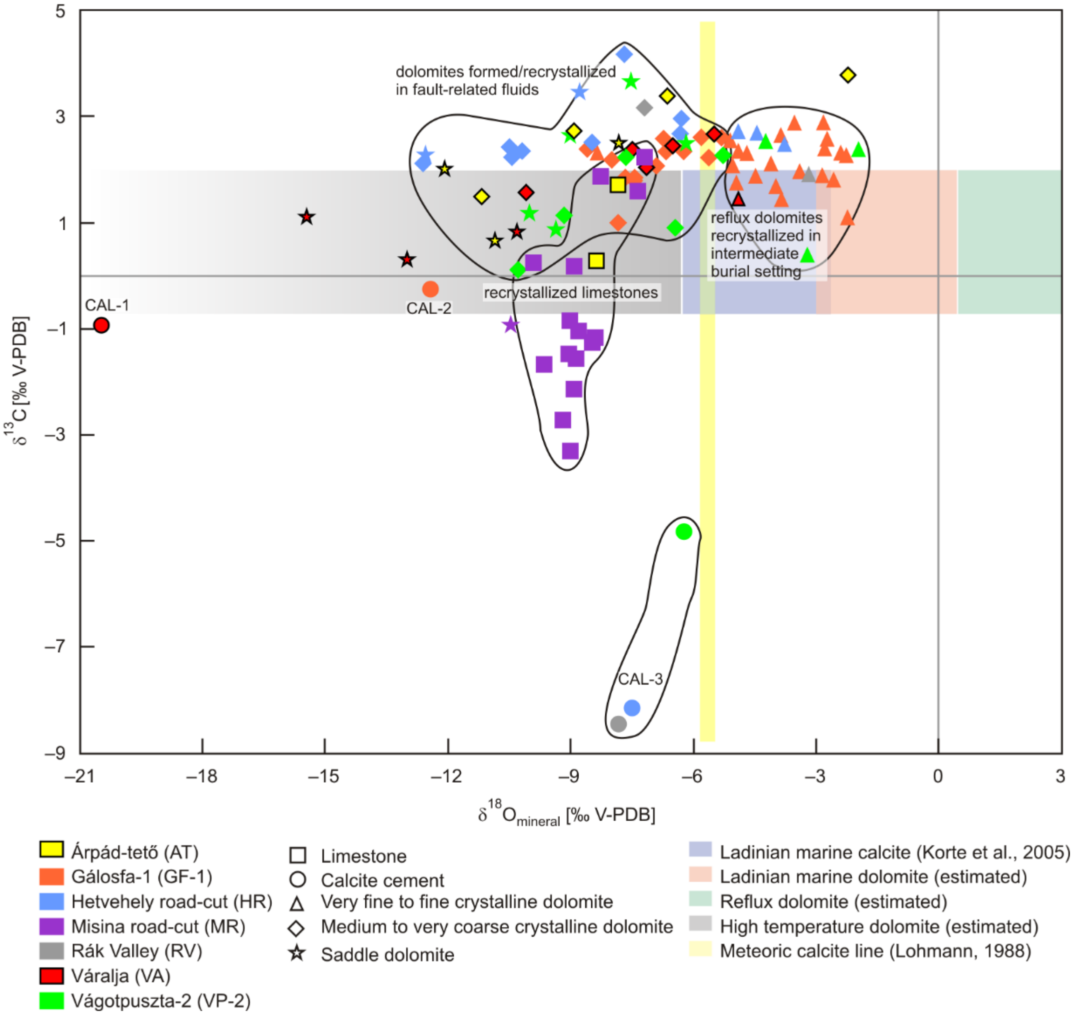

Fig. 8: Carbon and oxygen isotope plot for matrix dolomites, saddle dolomite cements, limestones and calcite cements. The colored symbols refer to the type and location of the samples, and the colored rectangles indicate the estimated composition of dolomites and calcites formed in various fluids.

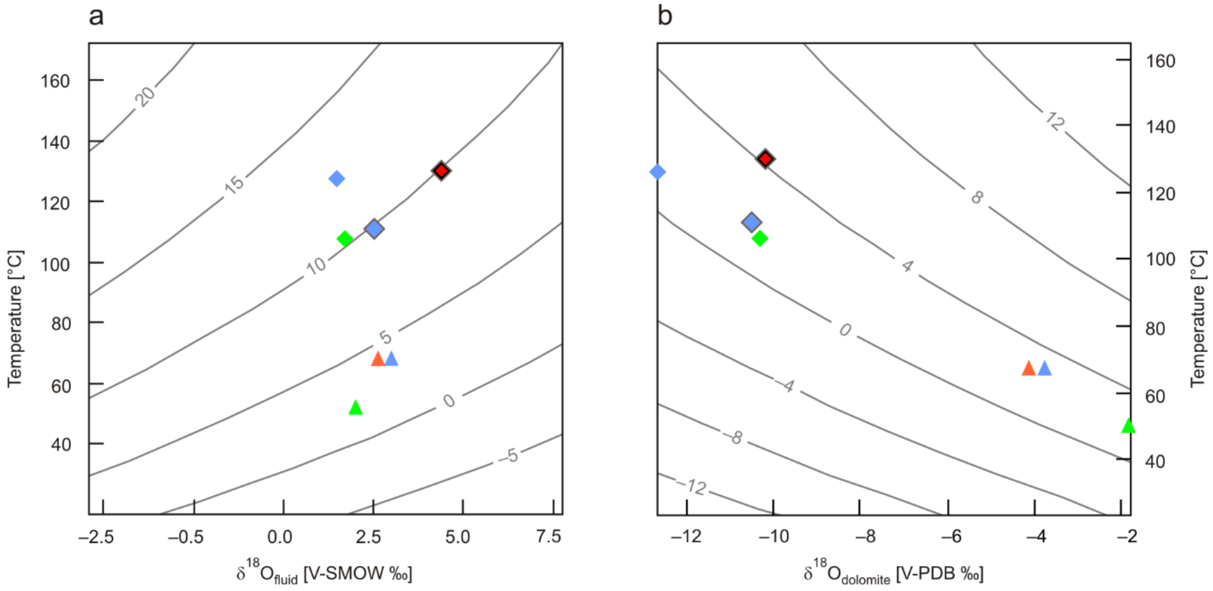

Fig. 9: Plots for clumped isotope data measured on matrix dolomite samples. Legend is the same as in Fig. 8. Symbols with brown outline mark samples for which Sr isotope data is not available (see Fig. 11b–c). **(a)** Relationship between temperatures converted from Δ_{47} and calculated $\delta^{18}O$ values of the diagenetic fluids. **(b)** Relationship between temperatures converted from Δ_{47} and measured $\delta^{18}O$ of matrix dolomites.

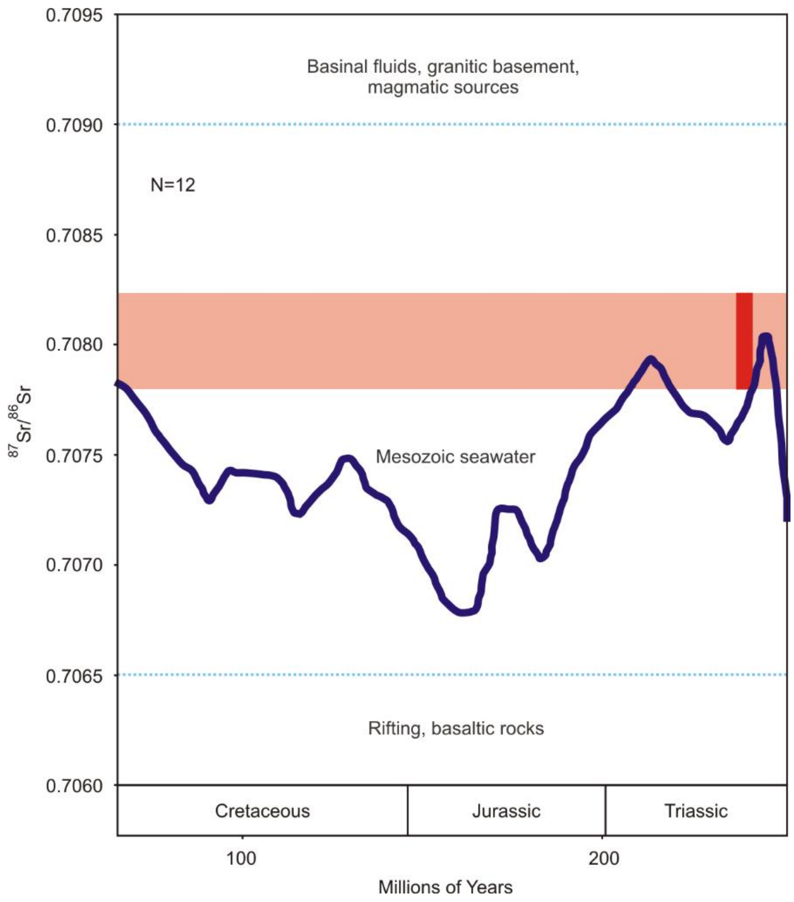

Fig. 10: Sr isotope secular curve of the Mesozoic Era (after McArthur et al., 2012) with range of values measured on the studied samples indicated by the red bar. N = number of analyzed samples.

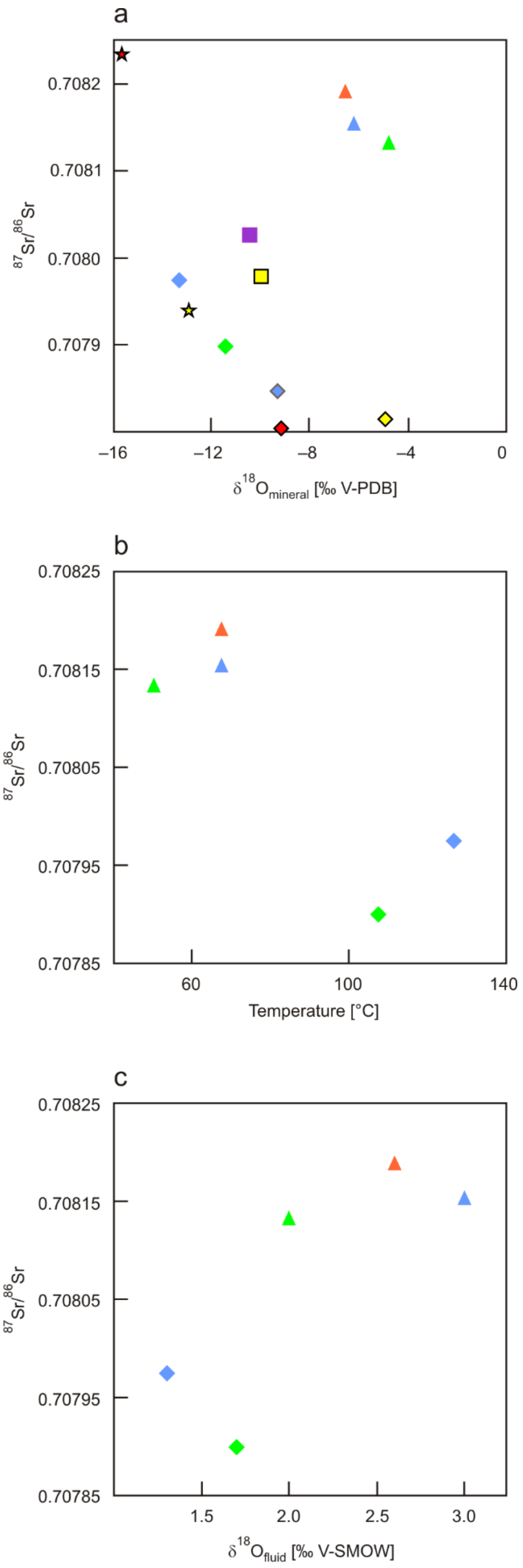
a
0.7082
0.7081
0.7080
0.7079
$^{87}Sr/^{86}Sr$
–16
–12
–8
–4
0
$\delta^{18}O_{mineral}$ [‰ V-PDB]
b
0.70825
0.70815
0.70805
0.70795
0.70785
$^{87}Sr/^{86}Sr$
60
100
140
Temperature [°C]
c
0.70825
0.70815
0.70805
0.70795
0.70785
$^{87}Sr/^{86}Sr$
1.5
2.0
2.5
3.0
$\delta^{18}O_{fluid}$ [‰ V-SMOW]

Fig. 11: Plots of Sr isotope vs. **(a)** $\delta^{18}O$ values of dolomite and limestone samples; **(b)** temperatures converted from Δ_{47} and **(c)** $\delta^{18}O$ values of diagenetic fluids. Legend is the same as in Fig. 8. Symbols with brown outline mark matrix dolomite samples for which clumped isotope data is not available. Otherwise, matrix dolomite samples are the same in (a), (b) and (c), and in Fig. 9.

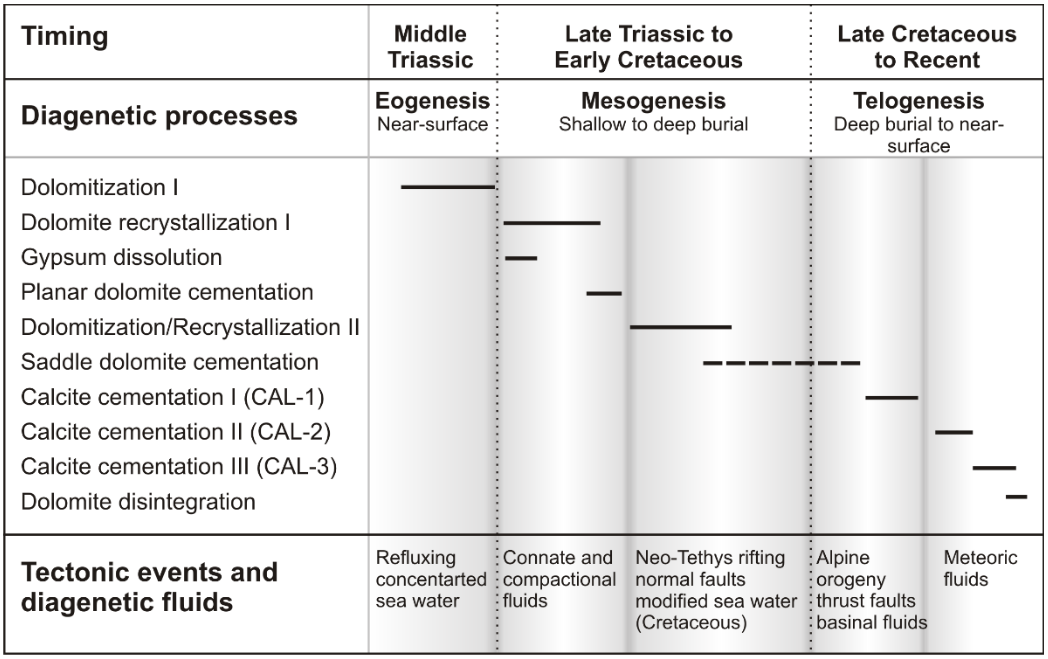

Fig. 12: Summary of the major diagenetic processes with estimated timing, burial setting, as well as inferred diagenetic fluids and tectonic events. Dashed line indicates that the saddle dolomite cementation event likely occurred in multiple episodes with evolving fluid compositions.

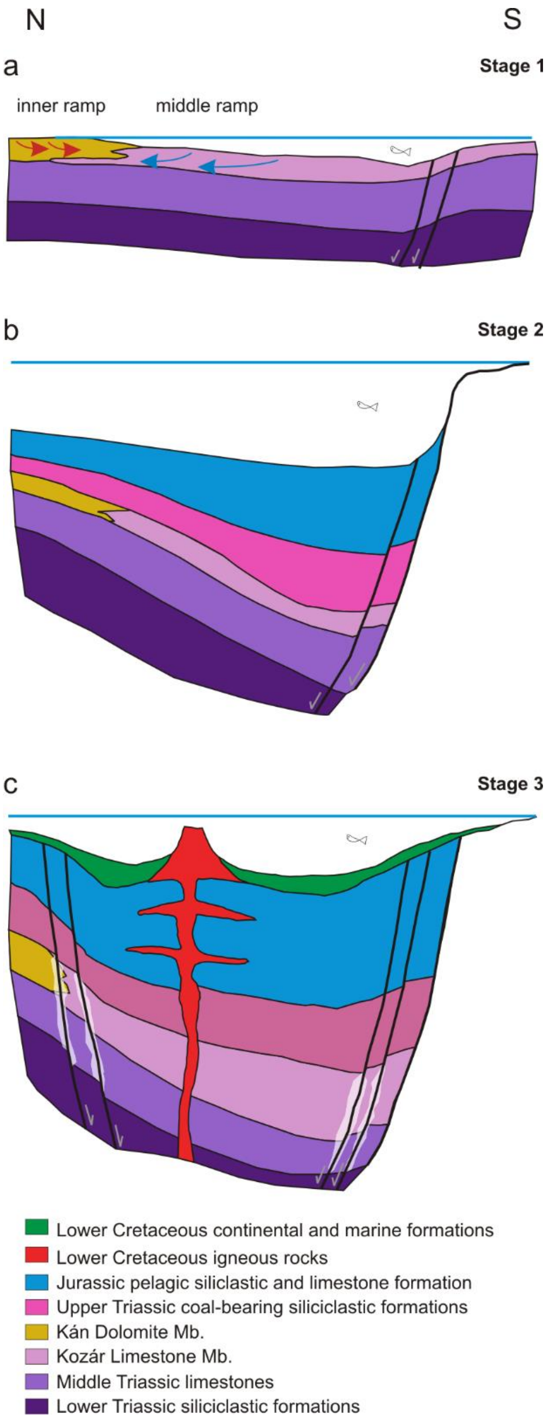

Fig. 13: Schematic evolution history of the Csukma Formation from the Middle Triassic until the Early Cretaceous. Drawings are not to scale. **(a)** Stage 1: Middle Triassic. Penecontemporaneous reflux dolomitization of the Kán Dolomite Member Geothermal circulation in the middle ramp prevents invasion of brines into the Kozár Limestone Member **(b)** Stage 2: Late Early Jurassic.

Increasing burial results in recrystallization of the Kán Dolomite Member in intermediate burial setting (ca. 1 to 2 km). **(c)** Stage 3: Early Cretaceous. Seawater is drawn down and circulated through rift-related faults (black lines) and causes recrystallization of the Kán Dolomite Member a second time, and dolomitization of the Kozár Limestone Member and the underlying limestones in the vicinity of the faults (indicated by grey shading) in a deep burial setting (ca. 5 km).

CHAPTER II

EARLY DOLOMITIZATION AND PARTIAL BURIAL RECRYSTALLIZATION: A CASE STUDY OF MIDDLE TRIASSIC PERITIDAL DOLOMITES IN THE VILLÁNY HILLS (SW HUNGARY) USING PETROGRAPHY, CARBON, OXYGEN, STRONTIUM AND CLUMPED ISOTOPE DATA

Abstract

Peritidal carbonates of the Csukma Formation (Csukma Dolomite Member) in the Villány Hills, SW Hungary, were investigated to determine the nature of the dolomitization and recrystallization processes that affected these rocks during their complex tectonic evolution, and to evaluate if the clumped isotope data preserved signals from the original dolomitization event or is indicative of the later recrystallization processes. Sedimentary and petrographic features, as well as geochemical characteristics integrated with the tectonic evolution of the area indicate that dolomitization likely occurred penecontemporaneously via geothermal convection of normal to slightly modified seawater in a near-surface to shallow burial setting, which was followed by partial recrystallization of the dolomites in an intermediate burial setting with low water to rock ratios. Results of this study suggest that the clumped isotope temperatures of partially recrystallized dolomites, via dissolution–re-precipitation, may provide a minimum estimate of the temperature of recrystallization. However, caution has to be taken when interpreting the thermal history and fluid evolution of successions that were affected by significant recrystallization.

2.1. Introduction

Dolomite rocks (also known as dolostones) have been the focus of long-term research interest due to their economic significance. Dolomitization happens in several ways and in a number of geological environments (e.g., Machel, 2004). In almost all of these Mg^{2+} is added to the calcareous sediment or limestone through hydrologic mechanisms that, under favorable circumstances, can be interpreted from the petrographic features and geochemistry of the dolomites. Perhaps the most important hindrance in deducing the paleohydrology of dolomitization is recrystallization. Recrystallization does not change the overall mineralogy of the rock; however, it may lead to alteration of various chemical, crystallographic and physical properties (cf., concept of significant vs. insignificant recrystallization; Machel, 1997). It has been demonstrated that early diagenetic dolomites are susceptible to recrystallization shortly after their formation (e.g., Gregg et al., 1992; Veillard et al., 2019). If the dolomite rock was significantly recrystallized during diagenesis, the resulting textures and geochemical parameters of the dolomites may lead to inaccurate genetic interpretations (Machel, 1997).

Carbonate clumped isotope thermometry (e.g., Ghosh et al., 2006; Eiler, 2007; Bonifacie et al., 2017) has recently been successfully applied to identify the nature and origin of diagenetic fluids (e.g., Ferry et al., 2011; Sena et al., 2014; Loyd et al., 2015; Millán et al., 2016; Came et al., 2017, Honlet et al., 2018; MacDonald et al., 2018; Mangenot et al., 2018). However, it has been shown that recrystallization at low water to rock ratios may obscure the calculated oxygen isotope composition of the diagenetic fluids, which may result in an erroneous genetic interpretation, even at shallow burial depth and low temperatures (Veillard et al., 2019). Nevertheless, clumped isotope temperatures provide an accurate estimate of the recrystallization temperature if the whole volume of the dolomite underwent microscale dissolution–re-precipitation; i.e., complete recrystallization (Veillard et al., 2019). The aim of the current study is to investigate if the clumped isotope data collected on dolomites that had undergone a complex tectonic evolution preserve signals diagnostic of the original dolomitization mechanism or if they represent the conditions of recrystallization. Furthermore, are the clumped isotope data suitable to provide accurate estimates of the recrystallization temperature and the nature of the diagenetic fluids if the recrystallization was incomplete, i.e., the dolomite rock is a mixture of recrystallized and original dolomite? To this end, dolomitized peritidal carbonates of the Middle Triassic Csukma Formation (Csukma Dolomite Member) in the Villány Hills area of southwest Hungary were investigated in detail.

The Csukma Dolomite Member (CDM) is made up of cyclic peritidal carbonates that are completely dolomitized and display varying degree of fabric preservation. The dolomitization and recrystallization history of the Mecsek Mts. occurrence of the Csukma Formation (Kán Dolomite Member) was studied in detail (Lukoczki et al., 2019). However, only limited information is available about the Villány Hills occurrence of the Csukma Formation and the available studies are mostly limited to basic lithological observations (Rakusz and Strausz, 1953; Nagy and Nagy, 1976; Rálisch-Felgenhauer, 1985, 1987; Rálisch-Felgenhauer and Török, 1993).

This paper provides a detailed interpretation of the dolomitization and dolomite recrystallization processes that affected the Middle Triassic Csukma Formation in the area of the Villány Hills. Detailed petrographic and geochemical investigation, including data from conventional stable carbon and oxygen isotope analyses, clumped stable isotopes, and strontium isotopes were applied. Our results suggest that the clumped isotope temperatures of partially recrystallized dolomites, via dissolution–re-precipitation, may provide a minimum estimate of the temperature of recrystallization, and caution has to be taken when interpreting the thermal history and fluid evolution of successions that were affected by significant recrystallization.

2.2. Geological setting

The Görcsöny Ridge and the Villány Hills comprise part of the Villány–Bihor structural unit within the Tisza Mega-Unit (Tisza MU) (Fig. 1). The Görcsöny Ridge and the Villány Hills are structurally separated by a Mesozoic overthrust zone north of the Villány Hills (Fig. 1b). In the area of the Görcsöny Ridge, the Paleozoic–Mesozoic rocks are unconformably overlain by Neogene deposits, whereas in the Villány Hills the Mesozoic succession is exposed on the surface (Fig. 2). Hereafter, the areas of the Görcsöny Ridge and the Villány Hills together will be referred to as Villány Hills area.

During the Triassic, the Villány-Bihor Unit was situated on the European shelf of the Neo-Tethys, between the near-continent Mecsek Unit, and the Békés-Codru Unit of shelf margin setting (Bleahu et al., 1994), south–southwest from the Bohemian Massif belonging to the Variscan Orogenic Belt (Pozsgai et al., 2017). The crystalline basement of the Villány-Bihor Unit is made up of Paleozoic metamorphic rocks formed during the Variscan orogeny (Haas and Péró, 2004). The late Paleozoic sedimentary succession is characterized by sandstones, shales, and claystones of molasse, fluvial and lacustrine origin that unconformably underlie the Lower Triassic fluvial Jakabhegy Sandstone Formation (Haas, 2012).

Transgression during the Middle Triassic (Anisian) resulted in the development of a mixed carbonate–siliciclastic ramp depositional environment with deposition of the Patacs Siltstone Formation, which was followed by the deposition of alternating layers of dolomite, dolomitic marl, claystone, siltstone and evaporite (anhydrite and gypsum) of the Hetvehely Formation (Fig. 3). Carbonate ramp sedimentation began during the middle Anisian and gave rise to the deposition of the inner ramp Rókahegy Dolomite, Lapis Limestone, and Zuhánya Limestone Formations (Fig. 3) (Török, 1998). Rifting of the Neotethys caused differentiation of the depositional environments in the area of the different structural units (Konrád, 1998). Deceleration of subsidence and coeval sea level fall near the end of the Middle Triassic (Ladinian) led to the deposition of the shallowing upward succession of the Csukma Dolomite

Member of the Csukma Formation the Villány Hills (Konrád, 1998) (Fig 3). Similar trend was observed in the coeval Kán Dolomite Member (KDM) in the Mecsek Mountains (Lukoczki et al., 2019) (Fig. 3).

Due to further regression and increasing humidity, terrigenous sediments (poorly lithified claystones, sandstones and marls) were interbedded, increasingly frequently upwards, within the overlying Templomhegy Dolomite Member (TDM) of the Csukma Formation (Fig. 3). The TDM was formed in peritidal environments along the ramp margin (Pozsgai, 2016, Botfalvai et al. 2019) (Fig. 3). During the Late Triassic (Carnian), the terrestrial–shallow marine Mészhegy Sandstone Formation was deposited in a coastal plain–shallow marine setting (Ősi et al., 2013, Botfalvai et al. 2019) (Fig. 3).

The burial history of the Villány Hills area records prolonged periods of subaerial exposure following the Middle Triassic (Vörös, 2009; 2010). The TDM is conformably overlain by a few meter thick Carnian succession. The Carnian age was mainly characterized by marine sedimentation with short periods of subaerial exposure when paleosols were formed. The Norian, Rhaetian, Hettangian and Sinemurian stages are missing, indicating a long erosional time interval when the entire TDM and the top of the CDM was removed across most parts of the study area. A conglomerate bed formed at the base of the Pliensbachian transgressional bed-set that contains dolomite pebbles probably derived from CDM. This is overlain by thin beds of pelagic limestones punctuated by submarine gaps. The Upper Jurassic is characterized by a ca. 200 m thick, upward shallowing pelagic carbonate sequence. Subaerial exposure at the Jurassic/Cretaceous boundary led to karstification of the Upper Jurassic carbonates.

Carbonate platforms developed on subsiding tectonic blocks during the Valanginian to early Albian ages of the Early Cretaceous (Fülöp 1966, Császár 2002). Around the end of the early Albian, the extension changed to compression due to the onset of the Alpine orogeny and stacking of thrust sheets began (Császár 2002, Haas and Péró, 2004). This Cretaceous thrusting occurred in two main stages separated by an extensional event that reactivated deep lithospheric fractures and led to the formation of igneous sills and dikes (Nédli and M. Tóth, 2007; Nédli et al., 2010). The complex tectonic evolution of the area continued during the Cenozoic (Csontos et al., 2002; Petrik 2009, 2010). The Görcsöny Ridge and Villány Hills were erosional areas until the early Miocene (Nagymarosy and Hámor, 2012). From the middle Miocene sedimentation occurred first in a terrestrial, then marine and later in a restricted brackish environment (Nagymarosy and Hámor, 2012). The Pliocene was mostly characterized by uplift and erosion, and during the Pleistocene interglacials, the Villány Hills underwent major karstification, and loess and red clays were deposited in the Görcsöny area (Jámbor, 2012).

2.3. Materials and methods

Samples of the Csukma Dolomite Member were collected from five locations in the area of the Villány Hills and the Görcsöny Ridge (four boreholes and one outcrop). The sampling locations are shown in Figure 1b and described in Table 1. A total of 257 thin sections were examined using an Olympus-BX51 petrographic microscope. The staining method of Dickson (1966) was applied to identify carbonate mineralogy using a solution of Alizarin red-S and potassium ferricyanide to discriminate calcite, Fe-calcite, dolomite, Fe-dolomite/ankerite. Dolomite textures were identified in accordance with the classification system of Sibley and Gregg (1987) as extended by Wright (2001) (see Machel, 2004). The crystal size scale of Folk (1959) was used to designate crystal size categories. Where possible, the original limestone microfacies were classified according to Dunham (1962) with modifications by Embry and Klovan (1972).

Samples for cathodoluminescence (CL) microscopy were selected based on their textures and cement contents. Fifty-two polished thin sections were analyzed with a CITL MK5-1 cold-cathode optical cathodoluminescence system at the Boone Pickens School of Geology, Oklahoma State University, under operating conditions of 8–12 keV and 0.5–0.7 mA.

Conventional stable carbon and oxygen isotope measurements were performed on 30 powder samples micro-drilled from matrix dolomite. Analyses were carried out on a Finnigan Delta Plus XP Isotope ratio mass-spectrometer (IRMS) at the Institute for Geological and Geochemical Research of the Hungarian Academy of Sciences, and on a Thermo Delta Plus IRMS coupled to a Gas Bench II at Pegasus Technical Services Inc., Cincinnati, OH, USA. NBS-18 and NBS-19 international, as well as internal laboratory standards were used at both laboratories and the reproducibility was better than ±0.1‰ in both laboratories. The differences measured on replicates of the same samples in the two laboratories were less than ±0.7‰. The results are reported as $\delta^{13}C$ and $\delta^{18}O$ relative to the Vienna Pee Dee Belemnite standard (V-PDB ‰).

Strontium isotope composition ($^{87}Sr/^{86}Sr$) of five matrix dolomite samples and one calcite cement sample were analyzed at the University of Kansas Radiogenic Isotope Laboratory and at the Canadian Centre for Isotopic Microanalysis at the University of Alberta. At the University of Kansas, the analyses were carried out on a VG Sector thermal ionization mass spectrometer with ±0.000014 error at a 95% confidence interval. At the University of Alberta a VG 354 thermal ionization mass spectrometer was used for analysis. Here the analytical precision was better than 0.000024 (2σ). The differences of the results in the two laboratories were systematic and allowed for correction of the values for comparison.

Carbonate clumped isotopes were measured on five matrix dolomite samples from the Csukma Dolomite Member in the Clumped Isotope Laboratory at Imperial College London on a Thermo Fisher MAT 253 isotope ratio mass spectrometer in dual inlet mode. The methodology is described in detail in Dale et al. (2014). Isotopic corrections and normalization was performed using the software Easotope (John and Bowen, 2016), using heated gases and the ETH carbonates

(Meckler et al. 2014) as standards. The calibration of Davies and John (2019) was used to convert the Δ_{47} values to temperatures. The results are presented in °C. The calibration of Horita (2014) was applied to calculate the $\delta^{18}O$ values of the parent fluids. The fluid $\delta^{18}O$ values are reported relative to the Vienna Standard Mean Ocean Water standard (V-SMOW ‰).

2.4. Results

2.4.1. Petrography

2.4.1.1. Matrix dolomites

The Csukma Dolomite Member (CDM) is made up of aphanocrystalline (<4 µm) to medium crystalline (up to 250 µm), planar-e to planar-s dolomites. The crystal size distribution is typically polymodal, with coarser crystals generally being limpid and the finer crystals being turbid (cloudy) due to inclusions. The degree of preservation of the sedimentary fabrics ranges from very good to none. Recognizable microfacies include mudstones, laminated mudstones (Fig. 5a–b), microbial boundstones (stromatolites) (Fig. 5c–d), micritic–pisolitic boundstones (Fig. 5e), ooid/peloid packstones or grainstones (Fig. 5f), bioclastic packstones and wackestones (typically crinoid and mollusc shell fragments and less typically green algae fragments, Fig. 5g), and peloidal–lithoclastic packstone. The grains are either mimetically or non-mimetically replaced by dolomite. Typically, inclusions form ghosts and/or micrite envelops that outline original limestone grains or, in case of leached grains, the shape of moldic pores. The transition between poorly and well preserved original limestone fabrics is either sharp (e.g., stylolitic surface) or gradual with increasing crystal size over the distance of a few mm. The micritic dolomite typically has bright red CL, whereas the limpid dolomite has dull red CL and displays compositional zoning in some samples (Fig. 5c–d). The fabric-destructive dolomites are typically medium crystalline, planar-e to planar-s with cloudy core–clear rim texture corresponding to mottled core and zoned rim in CL (Fig. 5h–i).

Both faint and sharply defined stylolites occur with amplitudes ranging from a few tens of μm to a few mm (Fig. 5j–k). Some stylolites cross-cut fractures filled with dolomite cement (described below).

Open pores include intercrystal, moldic, vug, and fracture pores. These pores are typically lined with planar-c dolomite (overgrowth) cements that display concentric zonation in CL. Some planar dolomites exhibit intracrystal porosity due to preferential dissolution of certain, likely Fe-rich, compositional zones (Fig. 5l). Fenestral pores and desiccation cracks are present in the laminated microfacies, typically filled with planar-c dolomite with very dull red CL zonation (Fig. 5c–d). Some larger vugs (up ca. 5 mm) are lined with planar dolomite cement and further filled with dolomicrite (Fig. 5m). Fractures are open or lined with planar dolomite cement and/or filled with blocky calcite cement.

Two types of breccias occur in the studied succession. In one type, coarse crystalline dolomite clasts occur in a dolomicrite matrix. In the other type, fine to medium crystalline dolomite clasts occur in medium crystalline planar-e to planar-s, zoned dolomite matrix/‘cement’ without sharp boundaries between the clasts and the matrix/‘cement’ (Fig. 5n). In such samples, some clasts are best discernible in CL (Fig. 5o).

2.4.1.2. Dolomite cements

Minor amounts of planar-c dolomite occur as cement overgrowth on medium crystalline planar-s dolomite crystals and lining and filling vugs (Fig. 6a–b), moldic pores (Fig. 6c–d), and fractures

(Fig. 6e–f). In CL, the dolomite cements display simple concentric compositional zonation (Fig. 6b, d, f). The zonation pattern is somewhat different in various parts of the sequence, which makes zone-by-zone correlation of the dolomite cements impossible. Undulatory extinction of some of the dolomite cements is revealed in cross-polarized light where the final one or two zones of the dolomite cement fill most of the pore space. Some of these crystals have slightly curved crystal faces, suggesting that they are saddle dolomite cements (Fig. 6g–j). Dolomite inclusions with dull red CL occur within very coarse crystalline (1–2 mm) calcite crystals. The dolomite inclusions are arranged in curved patterns that suggest a saddle dolomite precursor (Fig. 6f–g).

2.4.2. Geochemistry

All isotope data are tabulated in Table 2. In addition, conventional carbon and oxygen isotope data are plotted in Fig. 7, clumped isotope results are plotted Fig. 8, and Sr isotope data are plotted in Fig. 9.

2.4.2.1. Conventional carbon and oxygen isotopes

The $\delta^{13}C$ values of the matrix dolomites of the CDM range from –0.3‰ to 3.8‰. The $\delta^{13}C$ values for the very fine to fine crystalline dolomites within the CDM range from 0.3‰ to 3.8‰, and for the medium crystalline dolomites they range from –0.1‰ to 2.3‰.

The $\delta^{18}O$ values of the matrix dolomites of the CDM range from –8.7‰ to –0.3‰, with values for the very fine to fine crystalline matrix dolomites ranging from –4.0‰ to –0.3‰, and the $\delta^{18}O$ values of medium crystalline dolomite matrix dolomites within the CDM fall between –8.7‰ and –1.8‰.

2.4.2.2. Clumped isotopes

The Δ_{47} values of the very fine to medium crystalline dolomites of the Csukma Dolomite Member overlap and range from 0.589‰ to 0.637‰, with both end member values measured on fine crystalline dolomites. Corresponding temperatures range from 64 °C to 44 °C, respectively (Table 2, Fig. 8). The Δ_{47} values of the medium crystalline dolomites are 0.621‰ and 0.630‰, and the corresponding temperatures are 51 °C and 47 °C. The calculated $\delta^{18}O_{fluid}$ values for all samples range from –0.8‰$_{V\text{-}SMOW}$ to 2.7‰$_{V\text{-}SMOW}$. More specifically, the $\delta^{18}O_{fluid}$ values of the very fine to fine crystalline dolomite samples range from 0.7‰$_{V\text{-}SMOW}$ to 2.7‰$_{V\text{-}SMOW}$, whereas those of the medium crystalline dolomite samples are –0.8‰$_{V\text{-}SMOW}$ and 0.6‰$_{V\text{-}SMOW}$.

2.4.2.3. Strontium isotopes

The $^{87}Sr/^{86}Sr$ values of the very fine to medium crystalline matrix dolomites of the CDM range from 0.70779 to 0.70821 (Table 2, Fig. 9). Most values of dolomites from the CDM, regardless of crystal size, cluster closely around 0.7078 (±0.00003). An exception is one very fine crystalline dolomite sample, which has a higher value and is nearly identical to that of a very fine crystalline dolomite from the TDM around 0.7082 (±0.00002). The one analyzed calcite sample (location NK-2) has $^{87}Sr/^{86}Sr$ value of 0.70844.

2.5. Discussion

2.5.1. Dolomitization of the Csukma Dolomite Member (CDM)

The deposition of the CDM in the Villány Hills likely started on a more or less uniform carbonate ramp coevally with deposition of the Kán Dolomite Member (KDM) in the Mecsek Mountains, which is reflected in their sedimentological, petrographic and geochemical similarities (cf., Lukoczki et al., 2019, Figs. 7–9). The KDM likely was dolomitized penecontemporaneously via reflux, and the elevated Δ_{47} temperatures of the KDM dolomites likely reflect recrystallization in an intermediate burial setting (Lukoczki et al., 2019). The CDM likely also was dolomitized in a similar manner, at least initially. However, the sedimentological, petrographical and geochemical differences in the upper part of the CDM likely reflect ramp differentiation, and deviation in the burial histories of the Mecsek Mts. and the Villány Hills (Konrád, 1998; Bérczi-Makk et al., 2004). In this new setting, the dominant mechanism of dolomitization may have changed from reflux of hypersaline–mesohaline fluids to a mechanism where the dolomitizing agent was essentially normal seawater (or only insignificantly modified seawater), as suggested by the Sr isotope and the $\delta^{18}O_{fluid}$ values (Table 2), which fall close to marine values. This assumes that Triassic seawater had 0‰$_{V\text{-}SMOW}$ $\delta^{18}O_{fluid}$ and 0.7082 to 0.7075 $^{87}Sr/^{86}Sr$ isotope range during the Ladinian (Korte et al., 2003).

To achieve complete dolomitization of the CDM, large amounts of seawater are required to have circulated though this succession, with a water to rock ratio of about 650 at 100 % efficiency of dolomitization (see mass balance calculation by Land 1985). Assuming near-normal seawater as the dolomitizing agent, the Cenozoic dolomites of the Great Bahama platform may serve as a suitable analog for the CDM. Various interpretations exist to explain the hydrological system and driving forces of fluid circulation that may or might have been responsible for dolomitization in the analog Bahama platform. This includes mixing-zone induced circulation of underlying seawater (Vahrenkamp et al., 1991), a circulation system of shallow warm groundwater with elevated salinity and colder normal salinity seawater (Whitaker et al., 1994), and geothermal convection (Sanford et al., 1998). These hydrological systems may also be applicable to explain the dolomitization of the CDM. However, due to the more general applicability of the geothermal convection mechanism to “nearly all carbonate platforms independent of relative sea level” (Sanford et al., 1998, p. 803, also see Whitaker and Xiao, 2010), we postulate that the mechanism responsible for the dolomitization of the Csukma Dolomite Member was near-normal seawater circulating through the ramp due to geothermal convection. During geothermal convection (also called ‘open forced thermal convection’) in carbonate platforms, cold seawater invades the platform along its slope, advects laterally and vertically upwards, and discharges at the top of the platform due to basal heating and the thermal contrast between the cold seawater and the warm platform top. Numerical modelling results of Whitaker and Xiao (2010) showed that geothermal convection of normal seawater is capable of completely dolomitizing large carbonate bodies in millions to a few tens of millions of years typically in the temperature range of 20–30 °C. Furthermore, geothermal dolomitization may also result in complete dolomitization in narrower platforms and platforms with lower-relief than those of the Bahamas, including platforms that developed on fault blocks or shallow shelves of epeiric seas (Whitaker and Xiao, 2010). Therefore, geothermal convection of normal seawater likely caused dolomitization of the CDM carbonates of the Villány Hills area in near-surface to shallow burial setting.

The clumped isotope temperatures of the CMD, however, are higher (44–64 °C) than expected of near-surface geothermal dolomites (20–30 °C). Three scenarios will be considered to explain the higher clumped isotope temperatures: Scenario 1 – seawater dolomitization in intermediate burial setting. Scenario 2 – seawater dolomitization in a near-surface to shallow burial setting followed by hydrothermal dolomite cementation. Scenario 3 – seawater dolomitization in a near-surface to shallow burial setting followed by burial (geothermal) recrystallization.

2.5.1.1. Scenario 1: Intermediate burial dolomitization

Dolomitization of the CDM can also be interpreted as burial dolomitization in intermediate burial setting based on the temperatures calculated from the Δ_{47} data. However, considering the burial history of the area (Fig. 4), a circulation system suitable for seawater dolomitization was unlikely to have been maintained into intermediate burial settings (>600 m burial; Machel, 1999) to explain the calculated temperatures. Assuming 25 °C surface seawater temperatures (cf., Korte et al., 2005) and 25 °C /km geothermal gradient, the clumped isotope temperatures of 44–64 °C correspond to 880–1280 m burial depth. From the end of the Middle Triassic until the end of the Late Triassic the lowermost parts of the Csukma Formation remained buried at a depth of ca. 400 m (Fig. 4) while most parts of the basin were characterized by uplift, erosion and mixed siliciclastic–carbonate deposition. Moreover, dolomite clasts of the CDM are incorporated into the Lower Jurassic siliciclastics (Vörös, 2009; 2010), further indicating that dolomitization had to be a shallow burial diagenetic process. The bulk of the CDM likely reached intermediate burial depth (>~600 m; Machel, 1999) as late as the middle of the Early Cretaceous epoch, and it reached its deepest burial around the end of the Early Cretaceous, prior to the onset of the major phase of the Alpine orogeny (Fig. 4). Even though the base of the Csukma Formation might have reached a depth of ca. 1300 m at maximum burial corresponding to the clumped isotope temperature of 64 °C, the calculated >10 °C temperature difference between the lower and the upper part of the section (ca. 63 m core length difference) at location MGY-1 cannot be explained by a difference in burial depth, as such a difference would require a >200 °C/km geothermal gradient. Therefore, seawater dolomitization in an intermediate burial setting is not supported by the burial history.

2.5.1.2. Scenario 2: Shallow burial seawater dolomitization and hydrothermal cementation

The second scenario to explain the higher clumped isotope temperatures includes initial dolomitization by near-normal seawater in near-surface to shallow burial setting, as proposed in section 5.1., followed by the precipitation of dolomite cements from high(er) temperature fluids. Minor amounts of saddle dolomite cement and syntaxial cement overgrowth in the medium to coarse crystalline planar-s dolomites suggest this may be a viable scenario. According to this scenario, the Δ_{47} temperatures would represent physical mixtures of the low temperature matrix dolomites and the high(er) temperature cement dolomites. However, texturally different dolomites, such as fine crystalline and medium crystalline dolomites, yielded equal temperatures. Furthermore, the minor amounts of planar and saddle dolomite cements that occur in some of the studied samples likely formed during intermediate burial, possibly related to fluids originating from chemical compaction and dissolution of local dolomite (cf., Wanless, 1979). The multiple growth zones in dolomite cement (Fig. 6), and the lack of correlation of these growth zones across various samples even from the same location, suggest that the processes controlling the resulting CL patterns were complex and likely governed locally. According to the "restricted pore solution equilibrium" theory (see Machel, 1990, p. 81), fluids in pore spaces that are under hydrodynamic and/or diffusional restriction are not thoroughly mixed with the bulk of the diagenetic fluids in the aquifer. Within such microenvironments (pore spaces), chemical reactions between the pore fluid and the pore wall (rock/mineral) may locally alter the composition of the pore fluid. The chemical composition of such pore fluids, therefore, differ from the bulk of the aquifer. The resulting cements will differ across various locations within the same aquifer. The application of this theory is supported by the observation that the dolomite cement zones can be correlated, at most, over distances of a few mm, but not across samples taken tens of centimeters or meters apart. Further to such 'microenvironments,' solutes originating from pressure dissolution may also locally alter the composition of the pore fluids and result in the precipitation of cements that cannot be regionally correlated.

The estimated maximum burial temperature of the CDM (ca. 65 °C) and the maximum Δ_{47} temperature (64 °C) coincide with the lower limit generally considered necessary for saddle dolomite formation (above 60–80 °C; Spötl and Pitman, 1998). Thus, advection of hydrothermal fluids is not needed to explain the presence of saddle dolomite in the CDM. Also, any influx of hydrothermal fluids – presumably via faults – would have created far more saddle dolomite than the overall very small and scattered occurrences found in the study area.

The coarser crystalline dolomites, therefore, likely did not achieve the coarser crystal sizes as a result of high-temperature cement overgrowth on low-temperature dolomite cores. If this scenario was valid, higher clumped isotope temperatures would be expected to be measured on the coarser crystalline dolomites compared to those of the fine crystalline dolomites. While minor contribution of burial dolomite cements to the Δ_{47} data cannot be excluded, this scenario does not seem to be applicable to explain the clumped isotope temperatures because the very fine and the medium crystalline dolomites yielded equal clumped isotope temperatures.

2.5.1.3. Scenario 3: Shallow burial seawater dolomitization and burial recrystallization

Based on the above considerations, we suggest that the CDM underwent significant recrystallization (*sensu* Machel, 1997) with respect to at least the $\delta^{18}O$ and Δ_{47} composition in intermediate burial setting following complete dolomitization by near-normal seawater as suggested above (section 5.1.). The burial history of the area suggest that the succession did not reach the temperature domain where solid-state reordering of the C–O bonds is expected to take place (> 200–300 °C; Bonifacie et al., 2017). Therefore, recrystallization likely occurred via dissolution–re-precipitation processes (e.g., Machel, 1997) and solid-state reordering processes are not discussed further. Accordingly, both the calculated Δ_{47} temperatures and $\delta^{18}O_{dol}$ compositions likely represent a mixed signal between those indicating the conditions of the replacive dolomitization and the recrystallization processes. Recrystallization might have been induced by the invasion of a ‘new’ pore fluid in chemical disequilibrium with the pre-existing dolomite, similarly to the high-temperature recrystallization of the KDM dolomites in the Mecsek Mts. (Lukoczki et al. 2019). In the Mecsek Mts., this high-temperature recrystallization was interpreted to have occurred by Early Cretaceous seawater that was drawn down and circulated through rift-related faults (Lukoczki et al. 2019). However, in the Villány Hills area, evidence for this fault-controlled, high-temperature dolomitization and recrystallization, such as very coarse crystalline, fabric destructive, nonplanar-a matrix dolomite and larger amounts of saddle dolomite cements in the vicinity of faults, is missing. Based on the geological evolution of the Villány Hills area, therefore, the possible high-temperature fluids to cause dolomite recrystallization include (i) basin derived fluids that had interacted with the crystalline basement ascending through thrust faults during the Late Cretaceous, (ii) fluids that had interacted with Upper Cretaceous ultramafic igneous bodies, and (iii) mixed basinal–meteoric thermal waters originating from adjacent Neogene siliciclastics and Quaternary meteoric recharge. These options will be considered below.

Advection of basin derived, thrust-related fluids (option i) resulted in the precipitation of coarse crystalline calcite cement ($^{87}Sr/^{86}Sr$ value of 0.70844) and caused dedolomitization as suggested by the saddle dolomite inclusions associated with such calcite cements (Fig. 6 k–l). Therefore, significant dolomite recrystallization in this fluid is not supported. Furthermore, recrystallization in fluids that had interacted with the Upper Cretaceous ultramafic igneous intrusions of the Villány Hills (option ii) would have shifted the $^{87}Sr/^{86}Sr$ values of the CDM to lower values (cf., Burke et al., 1982; Banner, 1995). Therefore, recrystallization in such fluids is not supported either. Thermal waters (option iii) produced from fractured Triassic carbonate aquifers south from the Villány Hills, with a temperature of 62 °C from 48 m depth at the town of Harkány (Miseta et al., 2012), originate from the mixing of cold karst waters recharged in the Villány Hills with hot waters ascending from the adjacent Miocene siliciclastics of the Drava

Basin (Fig. 1b). Even though the composition of the produced water varies locally, interaction of the CDM with waters, which are sulfuric with active bacterial sulfate reduction (Miseta et al., 2012), is not supported by the $\delta^{13}C$ values of the CDM, which fall near the expected Middle Triassic marine values (Fig. 7). Furthermore, based on the tectonic evolution of the area, the Villány Hills have been in an emergent position since the early Neogene. Therefore, the outcrop samples taken for this study could not have been affected by these waters. This contention is further supported by the observation that the outcrop and subsurface samples of the CDM yielded similar geochemical data (Fig. 7, 8).

Based on the above consideration, we suggest that the recrystallization of the CDM occurred without the invasion of a new fluid. Therefore, the recrystallization must have been driven thermodynamically by high defect energy due to less than ideal stoichiometry and ordering, and/or reduction of surface free energy (Ostwald ripening) (Gregg and Shelton, 1990; Gregg et al., 1992). Furthermore, recrystallization likely was kinetically facilitated by the increased temperature associated with the burial of the succession (cf., Kaczmarek and Thornton, 2017).

2.5.2. Effect of recrystallization on the clumped isotope data

In the case of complete recrystallization the entire volume of the dolomite undergoes micro-scale dissolution and re-precipitation along a fluid film. The Δ_{47} values of such completely recrystallized dolomites would reflect the temperature at which the recrystallization occurred (e.g., Veillard et al. 2019). Therefore, a correlation between burial depth and Δ_{47} temperatures is expected for dolomites recrystallized during progressive burial.

Recently, Veillard et al. (2019) modelled low-temperature recrystallization and cementation processes of Miocene seawater dolomites using clumped isotope data. Similarly to the results of the current study, the Miocene dolomites investigated by Veillard et al. (2019) yielded $\delta^{18}O_{fluid}$ data with a range of composition that suggest that the apparent fluid composition ranged between brackish and slightly evaporitic seawater. They showed that this range of apparent fluid composition is the result of recrystallization via dissolution–re-precipitation with low water to rock ratio, and that the $\delta^{18}O_{fluid}$ values do not represent the compositions of the diagenetic fluid.

The range in the $\delta^{18}O_{fluid}$ values of the Csukma Dolomite Member likely also represent apparent, rather than real fluid composition as result of recrystallization. The correlation between clumped isotope temperatures and calculated $\delta^{18}O_{fluid}$ (Fig. 8) furthermore suggests that recrystallization of the Csukma Dolomite Member occurred at low water-rock ratio. The lack of a correlation between burial depth and Δ_{47} temperatures suggests that the range of $\delta^{18}O_{fluid}$ values may be due to incomplete recrystallization. The varying degree of recrystallization likely was controlled by a complex set of parameters, including differences in porosity and permeability, as well as chemical and crystallographic differences in the starting dolomite due to pre-dolomitization alterations. In the case of incomplete recrystallization, the Δ_{47} temperatures likely represent minimum rather than actual temperatures of recrystallization and the $\delta^{18}O_{fluid}$ values provide only a crude estimate of the nature of the dominant diagenetic fluid. The limited number of samples analyzed in this study makes it difficult to identify statistically significant correlations. Nevertheless, the calculated Δ_{47} temperatures correspond well with the burial history of the area and are accepted as reasonable estimates for the temperature of recrystallization of the CDM.

2.6. Conclusions

The peritidal carbonates of the Middle Triassic Csukma Dolomite Member of the Csukma Formation in the Villány Hills area likely underwent complete dolomitization in a near-surface to shallow burial setting via geothermally driven circulation of normal or slightly modified seawater. Elevated clumped isotope temperatures (44–64 °C) indicate recrystallization in intermediate burial setting (ca. 880–1280 m). Recrystallization was likely thermodynamically driven and kinetically facilitated by the increased temperature associated with burial of the succession. Correlation between the $\delta^{18}O_{fluid}$ values and temperatures calculated using clumped isotope data indicate low water to rock ratio during recrystallization. The lack of correlation between the burial depth and the Δ_{47} temperatures is likely due to incomplete recrystallization. Clumped isotope temperatures of partially recrystallized dolomites, therefore, likely represent minimum rather than actual temperatures of recrystallization.

Acknowledgements

This work was supported by the American Association of Petroleum Geologists Grants-in-Aid Program, the Geological Society of America Graduate Student Research Grant Program, the International Association of Sedimentologists Post-Graduate Grant Scheme, and the Hungarian Scientific Research Fund (OTKA K124313). SK was supported by the National Research, Development and Innovation Office (Hungary) (NKFIH, KH 125584). The authors are indebted to Tamás Budai and Gyula Konrád for their continued help and support.

References

Banner, J.L., 1995. Application of the trace element and isotope geochemistry of strontium to studies of carbonate diagenesis. Sedimentology, 42(5): 805–824.

Bérczi-Makk, Á., Konrád, G., Rálisch-Felgenhauer, Á. and Török, Á., 2004. Tisza Unit. In: J. Haas (Editor), Geology of Hungary. Triassic. ELTE Eötvös Kiadó, Budapest, pp. 303–360.

Bleahu, M., Mantea, G., Bordea, S., Panin, S., Stefanescu, M., Sikic, K., Haas, J., Kovács, S., Péró, C. and Bérczi-Makk, A., 1994. Triassic facies types, evolution and paleogeographic relations of the Tisza Megaunit. Acta Geologica Hungarica, 37(3–4): 187–234.

Bonifacie, M., Calmels, D., Eiler, J.M., Horita, J., Chaduteau, C., Vasconcelos, C., Agrinier, P., Katz, A., Passey, B.H. and Ferry, J.M., 2017. Calibration of the dolomite clumped isotope thermometer from 25 to 350 °C, and implications for a universal calibration for all (Ca,Mg,Fe)CO_3 carbonates. Geochimica et Cosmochimica Acta, 200: 255–279.

Botfalvai, G., Győri, O., Pozsgai, E., Farkas, I.M., Sági, T. and Szabó, M., 2019. Sedimentological characteristics and paleoenvironmental implication of Triassic vertebrate localities in Villány (Villány Hills, Southern Hungary). Geologica Carpathica, 70(2): 135–152.

Budai, T., Haas, J., Konrád, G. and Koroknai, B., 2014. Tisza Mega-unit. In: J. Haas and T. Budai (Editors), Geology of the pre-Cenozoic basement of Hungary. Explanatory notes for “Pre-Cenozoic geological map of Hungary” (1:500 000). Geological and Geophysical Institute of Hungary, Budapest.

Burke, W., Denison, R., Hetherington, E., Koepnick, R., Nelson, H. and Otto, J., 1982. Variation of seawater 87Sr/86Sr throughout Phanerozoic time. Geology, 10(10): 516–519.

Came, R.E., Azmy, K., Tripati, A. and Olanipekun, B.-J., 2017. Comparison of clumped isotope signatures of dolomite cements to fluid inclusion thermometry in the temperature range of 73–176 °C. Geochimica et Cosmochimica Acta, 199: 31–47.

Csontos, L., Benkovics, L., Bergerat, F., Mansy, J.-L. and Wórum, G., 2002. Tertiary deformation history from seismic section study and fault analysis in a former European Tethyan margin (the Mecsek–Villány area, SW Hungary). Tectonophysics, 357(1): 81–102.

Csontos, L., Nagymarosy, A., Horváth, F. and Kovác, M., 1992. Tertiary evolution of the Intra-Carpathian area: A model. Tectonophysics, 208(1): 221–241.

Dale, A., John, C.M., Mozley, P.S., Smalley, P.C. and Muggeridge, A.H., 2014. Time-capsule concretions: Unlocking burial diagenetic processes in the Mancos Shale using carbonate clumped isotopes. Earth and Planetary Science Letters, 394(Supplement C): 30–37.

Davies, A.J. and John, C.M., 2019. The clumped (^{13}C–^{18}O) isotope composition of echinoid calcite: Further evidence for “vital effects” in the clumped isotope proxy. Geochimica et Cosmochimica Acta, 245: 172–189.

Dickson, J., 1966. Carbonate identification and genesis as revealed by staining. Journal of Sedimentary Research, 36(2).

Dunham, R.J., 1962. Classification of carbonate rocks according to depositional textures. In: W.E. Ham (Editor), Classification of Carbonate Rocks - A Symposium. American Association of Petroleum Geologists, Tulsa, pp. 108–121.

Eiler, J.M., 2007. “Clumped-isotope” geochemistry—The study of naturally-occurring, multiply-substituted isotopologues. Earth and Planetary Science Letters, 262(3–4): 309–327.

Ferry, J.M., Passey, B.H., Vasconcelos, C. and Eiler, J.M., 2011. Formation of dolomite at 40–80 °C in the Latemar carbonate buildup, Dolomites, Italy, from clumped isotope thermometry. Geology, 39(6): 571–574.

Folk, R.L., 1959. Practical petrographic classification of limestones. AAPG Bulletin, 43(1): 1-38.

Ghosh, P., Adkins, J., Affek, H., Balta, B., Guo, W., Schauble, E.A., Schrag, D. and Eiler, J.M., 2006. 13C–18O bonds in carbonate minerals: A new kind of paleothermometer. Geochimica et Cosmochimica Acta, 70(6): 1439–1456.

Gregg, J.M., Howard, S.A. and Mazzullo, S., 1992. Early diagenetic recrystallization of Holocene (< 3000 years old) peritidal dolomites, Ambergris Cay, Belize. Sedimentology, 39(1): 143–160.

Gregg, J.M. and Shelton, K.L., 1990. Dolomitization and dolomite neomorphism in the back reef facies of the Bonneterre and Davis formations (Cambrian), southeastern Missouri. Journal of Sedimentary Research, 60(4).

Haas, J., 2012. Geology of Hungary. Springer Science & Business Media.

Haas, J., Budai, T. and Raucsik, B., 2012. Climatic controls on sedimentary environments in the Triassic of the Transdanubian Range (Western Hungary). Palaeogeography, Palaeoclimatology, Palaeoecology, 353: 31–44.

Haas, J. and Péró, C., 2004. Mesozoic evolution of the Tisza Mega-unit. International Journal of Earth Sciences, 93(2): 297–313.

Honlet, R., Gasparrini, M., Muchez, P., Swennen, R. and John, Cédric M., 2018. A new approach to geobarometry by combining fluid inclusion and clumped isotope thermometry in hydrothermal carbonates. Terra Nova, 30(3): 199–206.

Horita, J., 2014. Oxygen and carbon isotope fractionation in the system dolomite–water–CO2 to elevated temperatures. Geochimica et Cosmochimica Acta, 129: 111–124.

Jámbor, Á., 2012. Quaternary Evolution. In: J. Haas (Editor), Geology of Hungary. Springer, Heidelberg, pp. 201–213.

Kaczmarek, S.E. and Thornton, B.P., 2017. The effect of temperature on stoichiometry, cation ordering, and reaction rate in high-temperature dolomitization experiments. Chemical Geology, 468: 32–41.

Konrád, G., 1998. Synsedimentary tectonic events in the Middle Triassic evolution of the SE Transdanubian part of the Tisza Unit. Acta Geologica Hungarica, 41(3): 327–341.

Korte, C., Kozur, H.W., Bruckschen, P. and Veizer, J., 2003. Strontium isotope evolution of Late Permian and Triassic seawater. Geochimica et Cosmochimica Acta, 67(1): 47–62.

Korte, C., Kozur, H.W. and Veizer, J., 2005. $\delta^{13}C$ and $\delta^{18}O$ values of Triassic brachiopods and carbonate rocks as proxies for coeval seawater and palaeotemperature. Palaeogeography, Palaeoclimatology, Palaeoecology, 226(3): 287–306.

Land, L.S., 1980. The Isotopic and Trace Element Geochemistry of Dolomite: The State of the Art. In: D.H. Zenger, J.B. Dunham and R.L. Ethington (Editors), Concepts and Models of Dolomitization. SEPM, pp. 87–110.

Land, L.S., 1985. The origin of massive dolomite. Journal of Geological Education, 33(2): 112–125.

Loyd, S.J., Corsetti, F.A., Eagle, R.A., Hagadorn, J.W., Shen, Y., Zhang, X., Bonifacie, M. and Tripati, A.K., 2015. Evolution of Neoproterozoic Wonoka–Shuram Anomaly-aged carbonates: Evidence from clumped isotope paleothermometry. Precambrian Research, 264: 179–191.

Lukoczki, G., Haas, J., Gregg, J.M., Machel, H.G., Kele, S. and John, C.M., 2019. Multi-phase dolomitization and recrystallization of Middle Triassic shallow marine–peritidal carbonates from the Mecsek Mts. (SW Hungary), as inferred from petrography, carbon, oxygen, strontium and clumped isotope data. Marine and Petroleum Geology, 101: 440–458.

MacDonald, J.M., John, C.M. and Girard, J.-P., 2018. Testing clumped isotopes as a reservoir characterization tool: a comparison with fluid inclusions in a dolomitized sedimentary carbonate reservoir buried to 2–4 km. Geological Society, London, Special Publications, 468: 189–202.

Machel, H.G., 1990. Bulk solution disequilibrium in aqueous fluids as exemplified by diagenetic carbonates. In: I.D. Meshri and P.J. Ortoleva (Editors), Prediction of Reservoir Quality through Chemical Modeling. AAPG, Tulsa, pp. 71–83.

Machel, H.G., 1997. Recrystallization versus neomorphism, and the concept of ‘significant recrystallization’ in dolomite research. Sedimentary Geology, 113(3): 161–168.

Machel, H.G., 1999. Effects of groundwater flow on mineral diagenesis, with emphasis on carbonate aquifers. Hydrogeology Journal, 7(1): 94–107.

Machel, H.G., 2004. Concepts and models of dolomitization: a critical reappraisal. Geological Society, London, Special Publications, 235(1): 7–63.

Mangenot, X., Gasparrini, M., Rouchon, V. and Bonifacie, M., 2018. Basin-scale thermal and fluid flow histories revealed by carbonate clumped isotopes (Δ_{47}) – Middle Jurassic carbonates of the Paris Basin depocentre. Sedimentology, 65(1): 123–150.

Meckler, A.N., Ziegler, M., Millán, M.I., Breitenbach, S.F. and Bernasconi, S.M., 2014. Long-term performance of the Kiel carbonate device with a new correction scheme for clumped isotope measurements. Rapid Communications in Mass Spectrometry, 28(15): 1705-1715.

Millán, I.M., Machel, H. and Bernasconi, S.M., 2016. Constraining temperatures of formation and composition of dolomitizing fluids in the Upper Devonian Nisku Formation (Alberta, Canada) with clumped isotopes. Journal of Sedimentary Research, 86(1): 107–112.

Miseta, R., Palatinszky, M., Makk, J., Márialigeti, K. and Borsodi, A.K., 2012. Phylogenetic diversity of bacterial communities associated with sulfurous karstic well waters of a Hungarian spa. Geomicrobiology Journal, 29(2): 101–113.

Nagy, E. and Nagy, I., 1976. Triasbildungen des Villányer Gebirges. Geologica Hungarica, Series Geologica, 17: 111–227.

Nagymarosy, A. and Hámor, G., 2012. Genesis and Evolution of the Pannonian Basin. In: J. Haas (Editor), Geology of Hungary. Springer, Heidelberg, pp. 149–200.

Nédli, Z. and Tóth, T., 2007. Origin and geodynamic significance of Upper Cretaceous lamprophyres from the Villány Mts (S Hungary). Mineralogy and Petrology, 90(1–2): 73–107.

Nédli, Z., Tóth, T.M., Downes, H., Császár, G., Beard, A. and Szabó, C., 2010. Petrology and geodynamical interpretation of mantle xenoliths from Late Cretaceous lamprophyres, Villány Mts (S Hungary). Tectonophysics, 489(1–4): 43–54.

Ősi, A., Botfalvai, G., Prondvai, E., Hajdu, Z., Czirják, G., Szentesi, Z., Pozsgai, E., Götz, A.E., Makádi, L. and Csengődi, D., 2013. First report of Triassic vertebrate assemblages from the Villány Hills (Southern Hungary). Central European Geology, 56(4): 297–335.

Petrik, A., 2009. Interpretation of the results of microtectonic measurements performed with respect to Mesozoic formations of the Villány Hills, Hungary. Földtani Közlöny, 139: 217–236.

Petrik, A., 2010. Microtectonic measurements and interpretation of the Mesozoic formations in the Villány Hills and Görcsöny-Máriakéménd Ridge, Hungary. Central European Geology, 53(1): 21–42.

Pozsgai, E., 2016. Depositional environment of the Templomhegy Dolomite (Villány Hills) based on lithological and sedimentological observations. Modern Geográfia(II): 1–17.

Pozsgai, E., Józsa, S., Dunkl, I., Sebe, K., Thamó-Bozsó, E., Sajó, I., Dezső, J. and von Eynatten, H., 2017. Provenance of the Upper Triassic siliciclastics of the Mecsek Mountains and Villány Hills (Pannonian Basin, Hungary): constraints to the early Mesozoic paleogeography of the Tisza Megaunit. International Journal of Earth Sciences, 106(6): 2005–2024.

Rakusz, G. and Strausz, L., 1953. Geology of the Villány Mountains. Ann Rept Geol Instit Hungary, 41(2): 3–27.

Rálisch-Felgenhauer, E., 1985. Villány Hills, Villány, Templom Hill road-cut section (Villányi-hegység, Villány, Templomhegyi siklóbevágás), Magyarország geológiai alapszelvényei. Geological Institute of Hungary, Budapest, 5 p.

Rálisch-Felgenhauer, E., 1987. Villány Hills, Villány, Templom Hill lower quarry (Villányi-hegység, Villány, Templom-hegyi alsó kőfejtő), Magyarország geológiai alapszelvényei. Geological Intitute of Hungary, Budapest, 5 p.

Rálisch-Felgenhauer, E. and Török, Á., 1993. Csukma Formation (Csukmai Formáció), Magyarország litosztratigráfiai alapegységei. Geological Institute of Hungary, Budapest, pp. 248–251.

Sanford, W.E., Whitaker, F.F., Smart, P.L. and Jones, G., 1998. Numerical analysis of seawater circulation in carbonate platforms: I. Geothermal convection. American Journal of Science, 298(10): 801–828.

Sena, C.M., John, C.M., Jourdan, A.-L., Vandeginste, V. and Manning, C., 2014. Dolomitization of Lower Cretaceous Peritidal Carbonates By Modified Seawater: Constraints From Clumped Isotopic Paleothermometry, Elemental Chemistry, and Strontium Isotopes. Journal of Sedimentary Research, 84(7): 552–566.

Sibley, D.F. and Gregg, J.M., 1987. Classification of dolomite rock textures. Journal of Sedimentary Research, 57(6): 967–975.

Spötl, C. and Pitman, J., 1998. Saddle (baroque) dolomite in carbonates and sandstones: a reappraisal of a burial-diagenetic concept. Carbonate Cementation in Sandstones: Distribution Patterns and Geochemical Evolution: 437–460.

Török, Á., 1998. Controls on development of Mid-Triassic ramps: examples from southern Hungary. Geological Society, London, Special Publications, 149(1): 339–367.

Vahrenkamp, V.C., Swart, P.K. and Ruiz, J., 1991. Episodic dolomitization of late Cenozoic carbonates in the Bahamas; evidence from strontium isotopes. Journal of Sedimentary Research, 61(6): 1002–1014.

Veillard, C.M., John, C.M., Krevor, S. and Najorka, J., 2019. Rock-buffered recrystallization of Marion Plateau dolomites at low temperature evidenced by clumped isotope thermometry and X-ray diffraction analysis. Geochimica et Cosmochimica Acta, 252: 190–212.

Vörös, A., 2009. Tectonically-controlled Late Triassic and Jurassic sedimentary cycles on a peri-Tethyan ridge (Villány, southern Hungary). Central European Geology, 52(2): 125-151.

Vörös, A., 2010. The Mesozoic sedimentary sequences at Villány (southern Hungary). Földtani Közlöny, 140(1): 3–30.

Wanless, H.R., 1979. Limestone response to stress; pressure solution and dolomitization. Journal of Sedimentary Research, 49(2): 437–462.

Whitaker, F., Smart, P., Vahrenkamp, V., Nicholson, H. and Wogelius, R., 1994. Dolomitization by near-normal seawater? Field evidence from the Bahamas. Dolomites, A Volume in Honour of Dolomieu, 21: 111–132.

Whitaker, F.F. and Xiao, Y., 2010. Reactive transport modeling of early burial dolomitization of carbonate platforms by geothermal convection. AAPG bulletin, 94(6): 889–917.

Wright, W.R., 2001. Dolomitization, fluid-flow and mineralization of the Lower Carboniferous rocks of the Irish Midlands and Dublin Basin, PhD dissertation, University College Dublin, Belfield, Ireland.

Tables

Table 1: Description of sampling locations with abbreviations (Location ID) used throughout the text.

Location ID	Name	Description
MGY-1	Máriagyűd-1	The lower half of the Csukma Dolomite Member (CDM) was drilled in the depth from 153.8 m to 395.2 m within the Csukma Sliver. Thick bedded to laminated, subtidal, intertidal and supratidal, light to dark gray, or brown, typically very fine to medium crystalline dolomites. Abundant vug pores. The lowermost part is mottled dolomite with greenish brown or pinkish mottling.
ZB	Zuhánya quarry	Lower part (ca. 1/5) of the Csukma Dolomite Member exposed in the Csukma Sliver. Thick bedded to laminated, intertidal and supratidal, light gray to light pinkish, fine to medium crystalline dolomites. Abundant vug pores.
V-6	Villány-6	The complete succession of the Csukma Dolomite Member was drilled between 80 and 580 m, and the lower part of the Templomhegy Dolomite was drilled between 4 and 80 m in the Villány Sliver. The Csukma Dolomite Member is typically thick bedded, light gray or brown with abundant vug pores and chert nodules (Nagy and Nagy, 1976).
MK-3	Máriakéménd-3	Gray to brownish gray, typically massive or vuggy dolomite was drilled between 175.4 and 390.4 m in the area of the Görcsöny Ridge. The lowermost part is mottled dolomite with greenish brown or pinkish mottles.
NK-2	Nagykozár-2	Gray to brownish gray, typically very fine crystalline dolomite with tectonic breccia was drilled from 675 m to 737 m in the area of the Görcsöny Ridge.

Table 2: List of geochemical analytical results. MC: medium crystalline matrix dolomite, VF: very fine to fine crystalline matrix dolomite.

Sample ID	**$\delta^{18}O$ (‰ V-PDB)**	**$\delta^{13}C$ (‰ V-PDB)**	**Type**	**$^{87}Sr/^{86}Sr$**	**Δ_{47} (‰)**		**T (°C)**			**$\delta^{18}O_{fluid}$ (‰ V-SMOW)**
					mean	**SE**	**mean**	**min.**	**max.**	
MGY-1 161.0 m	–2.1	1.3	MC							
MGY-1 170.4 m	–3.2	1.0	VF							
MGY-1 181.5 m	–2.0	2.1	MC							
MGY-1 210.0 m	–2.3	2.1	MC							
MGY-1 253.8 m	–1.1	2.2	VF							
MGY-1 309.3 m	–1.7	2.3	VF							
MGY-1 318.7 m	–3.3	–0.3	MC	0.70779	0.621	0.005	51	48	53	0.6
MGY-1 333.5 m	–4.0	–0.1	MC		0.630	0.007	47	44	50	–0.8
MGY-1 339.7 m	–2.1	1.7	VF							
MGY-1 342.3 m	–3.8	2.2	VF							
MGY-1 346.9 m	–2.0	1.7	VF		0.637	0.011	44	40	48	0.7
MGY-1 352.1 m	–4.0	0.3	VF							
MGY-1 366.5 m	–2.6	2.0	VF							
MGY-1 374.5 m	–3.6	1.5	MC							
MGY-1 381.5 m	–3.6	1.6	VF		0.589	0.011	64	60	69	2.7
MGY-1 388.0 m	–2.2	3.8	VF							
MGY-1 392.7 m	–1.0	3.0	VF							
MK-3 182.6 m	–1.8	1.2	VF	0.70782						
MK-3 210.5 m	–0.3	2.6	VF							
MK-3 231.0 m	–1.8	2.3	MC							
MK-3 272.0 m	–1.5	2.4	VF							
MK-3 290.7 m	–2.7	1.7	MC							
MK-3 325.0 m	–5.2	1.9	MC							
MK-3 329.7 m	–7.1	0.4	MC	0.70782						
NK-2 694.5 m	–2.8	1.7	MC							
NK-2 709.0 m	–3.0	1.4	VF	0.70821						
NK-2 730.1 m	–4.0	0.5	MC							
ZB 2	–3.4	2.0	VF							
ZB 4	–2.2	2.3	VF	0.70782	0.621	0.005	51	49	53	1.6
ZB 6	–2.3	1.5	VF							

Figures

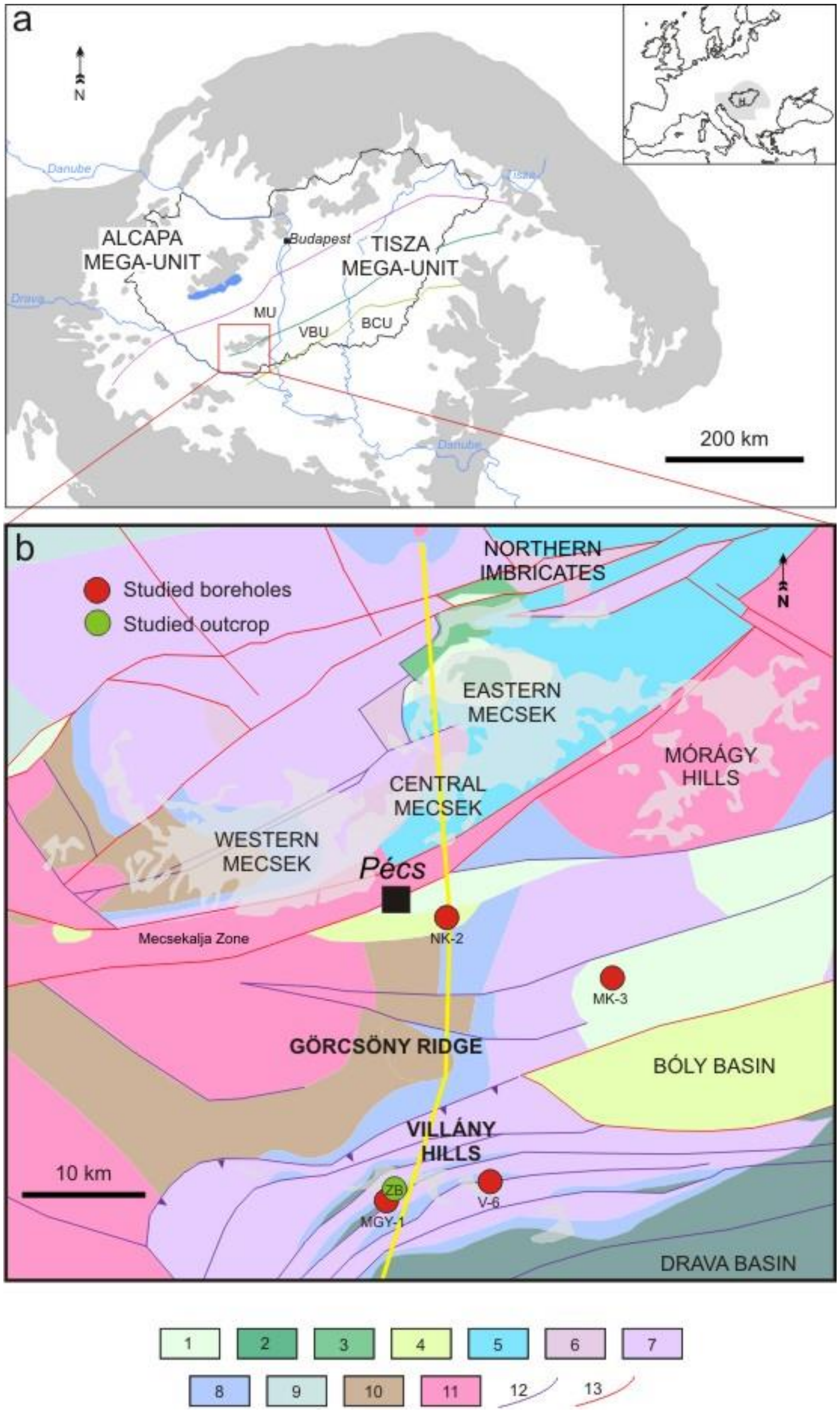

Fig. 1: Location of the study area. **(a)** The study area is situated in SW Hungary as indicated by the red rectangle. The purple line represents the Mid-Hungarian Fault Zone. The green lines mark

the boundaries between the subunits of the Tisza Mega-Unit. MU: Mecsek Unit, VBU: Villány-Bihor Unit, BCU: Békés-Codru Unit (modified after Csontos et al., 1992). Gray shading indicates outcrops of Pre-Neogene formations. The inset map shows the location of the Pannonian Basin and Hungary within Europe. **(b)** Simplified geological map of the study area showing the sampling locations (Cenozoic cover not shown). Shaded areas indicate outcrops of Pre-Cenozoic formations (modified after Haas, 2012). Yellow line marks the approximate location of the N–S cross section shown in Fig. 2. Purple triangles indicate the Mesozoic overthrust zone that separates the Villány Hills from the Görcsöny Ridge. Sampling locations: MGY-1: Máriagyűd-1, MK-3: Máriakéménd-3, NK-2: Nagykozár-2, V-6: Villány-6, ZB: Zuhánya quarry. Legend: 1: Upper Cretaceous continental and marine formations, 2: Lower Cretaceous platform limestones, 3: Lower Cretaceous volcanic rocks, 4: Middle Jurassic to Lower Cretaceous pelagic limestones, 5: Lower and Middle Jurassic siliciclastic formations, 6: Upper Triassic to Lower Jurassic coal-bearing siliciclastic formations, 7: Middle Triassic shallow marine siliciclastic and carbonate formations, 8: Lower Triassic siliciclastic formations, 9: Mesozoic rocks in general, 10: Permian and Upper Carboniferous continental siliciclastic formations, 11: Paleozoic crystalline rocks, 12: Mesozoic fault lines, 13: Cenozoic fault lines.

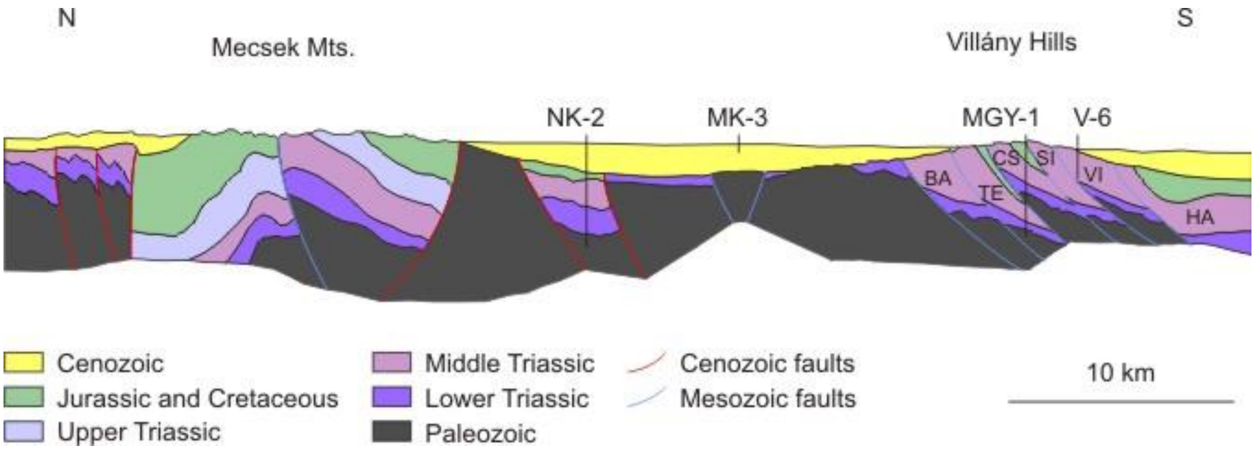

Fig. 2: Schematic N–S cross section of SW Transdanubia (after Budai et al., 2014) along the cross section line indicated in Fig. 1b. The borehole locations (black vertical lines) are approximate as only NK-2 falls on the cross section line with MK-3 being farthest off the cross section line (i.e., Mesozoic succession is missing where the cross section line is located). Abbreviations: NK-2: Nagykozár-2, MK-3: Máriakéménd-3, MGY-1: Máriagyűd-1, V-6: Villány-6, BA: Babarcszőlős Sliver, TE: Tenkes Sliver, CS: Csukma Sliver, SI: Siklós Sliver, VI: Villány Sliver, HA: Harsányhegy Sliver.

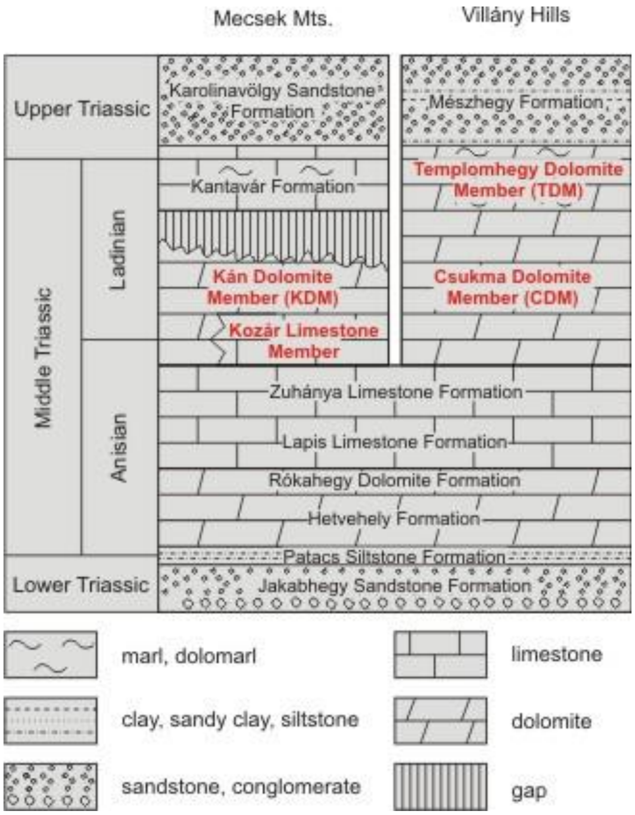

Fig. 3: Schematic stratigraphic column of the Triassic succession of the Villány Hills and the Mecsek Mts. Names highlighted in bold red are members of the Csukma Formation. Lateral (temporal) relationships are approximate.

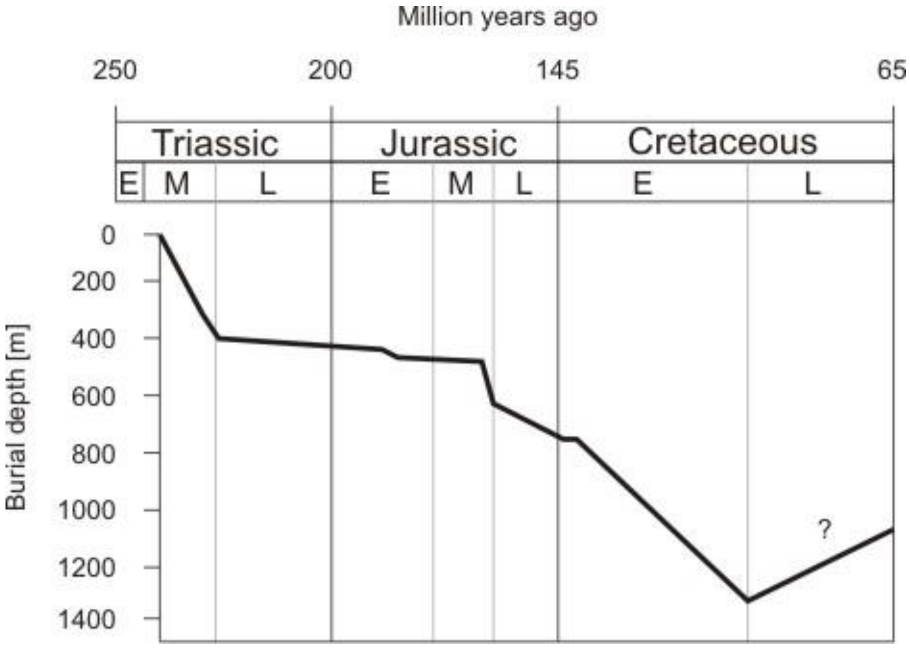

Fig. 4: Mesozoic burial curve of the Csukma Dolomite Member in the Villány Hills. The curve represents the base of the Csukma Formation (after Vörös, 2009).

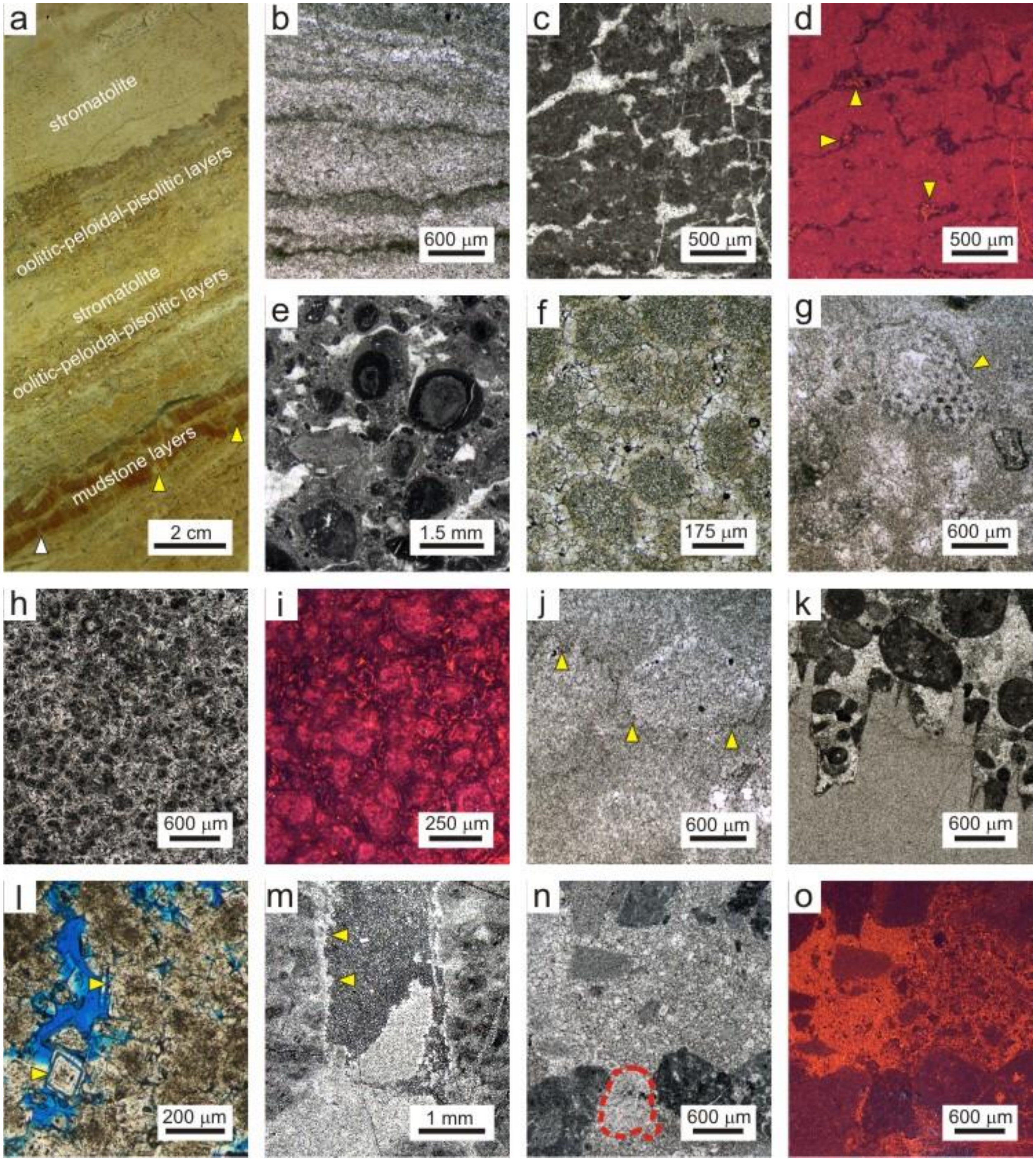

Fig. 5: Sedimentary and petrographic features of the Csukma Dolomite Member. **(a)**: Upper intertidal to lower supratidal succession with fenestral fabric (stromatolite), oolitic–peloidal–pisolitic layers, and laminated mudstone layers with desiccation cracks (arrows). Polished core slab. (Location MGY-1) **(b)** Very fine to medium crystalline planar-s dolomite with recognizable

laminated sedimentary fabric. Plane-polarized light. (Location MGY-1) **(c)** Aphanocrystalline and very fine crystalline dolomite with well-preserved stromatolite fabric. Fenestral pores are filled (replaced?) by coarse crystalline, planar-s dolomite. Plane-polarized light. (Location MGY-1) **(d)** Same as in (c) in CL. The aphanocrystalline to very fine crystalline dolomite is bright red, whereas the dolomites filling the fenestral pores are very dull, brighter towards the center of larger pores where the dolomite displays simple concentric zonation (arrows). **(e)** Pisolitic dolomite made up of very fine crystalline dolomite with excellent fabric preservation. The pisolitic grains occur in sedimentary layers with peloidal–fenestral fabric. Fenestral pores are filled (replaced?) by coarse crystalline, planar-s dolomite. Plane-polarized light. (Location MGY-1) **(f)** Fine to medium crystalline planar-s dolomite with poorly preserved sedimentary fabric. The fine crystalline ghosts suggest ooid grainstone or packstone precursor. Plane-polarized light. (Location MK-3) **(g)** Very fine to medium crystalline dolomite with poorly preserved bioclastic packstone or wackestone fabric. Large bioclast was likely a green algae fragment (arrow). Plane-polarized light. (Location V-6) **(h)** Coarse crystalline, planar-e to planar-s dolomite with cloudy core–clear rim appearance. In the clear(er) rims, solid inclusions are arranged along mostly planar growth zones. Plane-polarized light. (Location MK-3) **(i)** Same as in (h) in CL. The cloudy cores display red mottled CL, whereas the rims are mostly non-luminescent with brighter orange zones and patches. **(j)** Very fine to fine crystalline planar-s dolomite with very poor fabric preservation. Stylolite seam (arrows) is barely discernible. Plane-polarized light. (Location MK-3) **(k)** Intraclastic–peloidal/pisolitic dolograinstone juxtaposed with fine crystalline dolomudstone along sharp stylolite. Plane-polarized light. (Location MGY-1) **(l)** Fine to medium crystalline planar-s to planar-e dolomite with cloudy core–clear rim appearance and with open intercrystal and intracrystal (yellow arrows) pores. Blue-dyed epoxy. Plane-polarized light (Location ZB) **(m)** Vug pore in fine crystalline doloboundstone filled with fine crystalline dolomite and fragments of medium crystalline planar-s dolomite. Note the planar dolomite crystals along the pore. Plane-polarized light. (Location MGY-1) **(n)** Very fine to medium crystalline, planar-s to planar-e dolomite breccia. The breccia clasts are comprised of fragments of doloboundstones with good fabric preservation, fine crystalline dolomites (dolomudsontes) and medium crystalline, planar-s, fabric destructive dolomite replacing clasts (red dashed outline). Plane-polarized light. (Location NK-2) **(o)** Same as in (m) in CL. Breccia clasts are more easily discernible due to their dull red CL. The cement/matrix of the breccia is made up of medium crystalline planar-e to planar-s dolomite with concentric CL zonation.

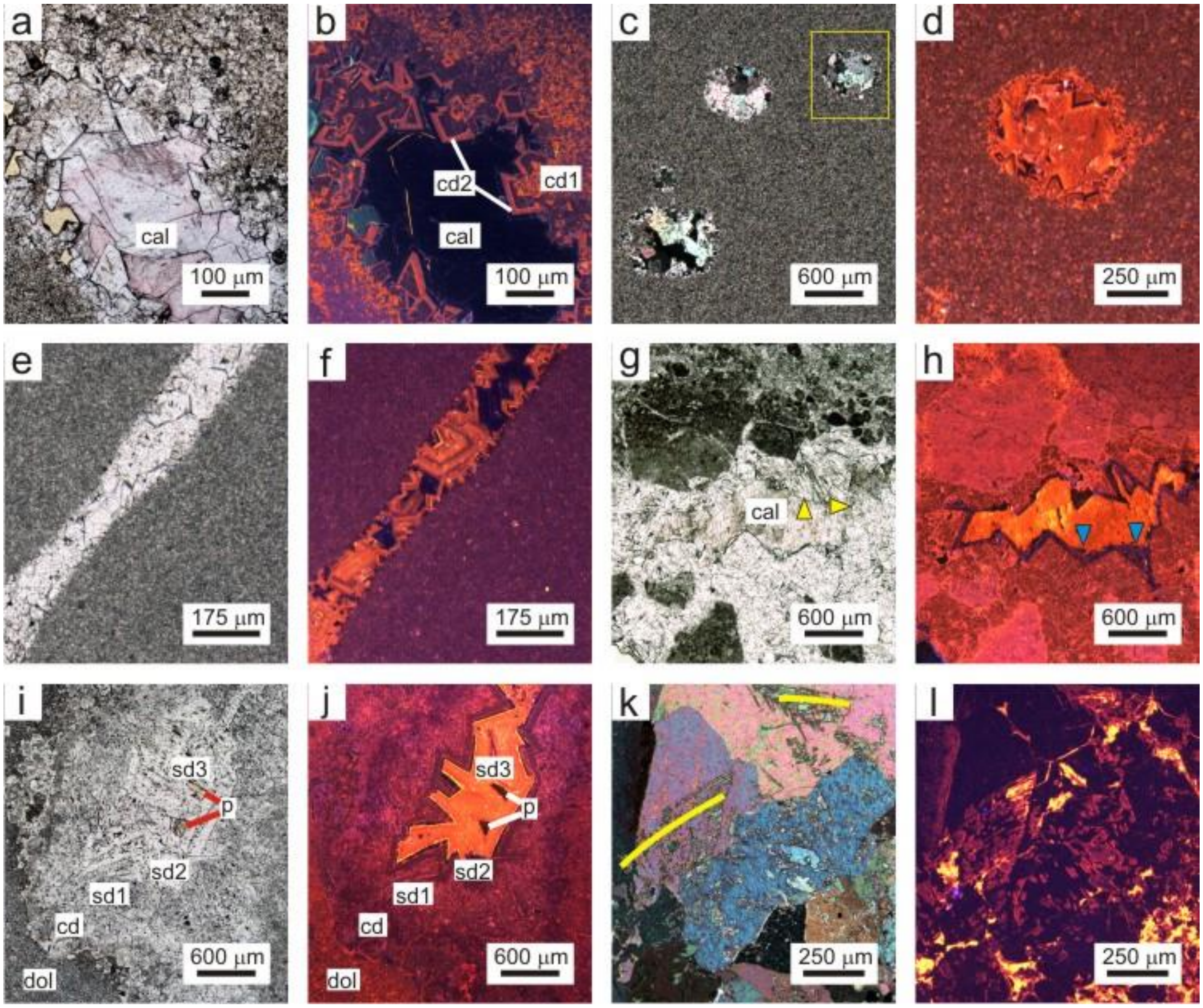

Fig. 6: Petrographic features of the dolomite cements in the studied succession. **(a)** Planar-c dolomite lining vug pore in fine crystalline dolomite. Calcite (cal) fills part of the remaining pore space. Stained thin section. Plane-polarized light. (Location MGY-1) **(b)** Same as (a) in CL. Two generations of planar dolomite cement are discernible in CL (cd1 and cd2). The calcite cement is non-luminescent with a single thin bright orange zone. **(c)** Round moldic pores filled with planar-c dolomite cement. CL image of pore filling dolomite in the yellow frame is shown in (d). Cross-polarized light. (Location MK-3) **(d)** Higher magnification CL image of a portion of (c) indicated with the yellow frame. The cement dolomite is finely zoned along the rim of the pore and the bulk of the pore space is filled with a few larger crystals showing homogenous red CL. **(e)**

Dolomite-filled fracture in a fine crystalline dolomudstone. Plane-polarized light. (Location NK-2) **(f)** Same as in (e) in CL showing concentric zonation of the fracture-filling dolomite. **(g)** Dolomite cement with slightly curved crystal faces (arrows) in aphano- to very fine crystalline dolomite. The remaining pore space is filled by coarse crystalline calcite (cal). Plane-polarized light. (Location MGY-1) **(h)** Same as in (g) in CL. The saddle dolomite cement is dull red with a non-luminescent final zone (appears slightly purplish in the picture). The calcite cement displays bright orange CL. **(i)** Fine crystalline dolomite with vug pore filled with multiple generations of dolomite cement [better visible in (j)]. Plane-polarized light. (Location NK-2) **(j)** Same as in (i) in CL. The matrix dolomite (dol) is followed by planar dolomite cement (cd). The first saddle dolomite phase (sd1) is inclusion-rich and displays a mottled CL, which is followed by a less inclusion-rich dolomite cement with dull red to non-luminescent CL zonation (sd2). The final saddle dolomite phase (sd3) is bright orange with faint concentric compositional zonation. P indicates open pores. **(k)** Dolomite inclusions within coarse crystalline calcite. The slightly curved arrangement of the dolomite inclusions, highlighted by the yellow lines, suggest a saddle dolomite precursor. Cross-polarized light. (Location MK-3) **(l)** Same as in (k) in CL. The dolomite inclusions are dull brown to red whereas the calcite is mostly non-luminescent with bright orange-yellow zones and irregular patches.

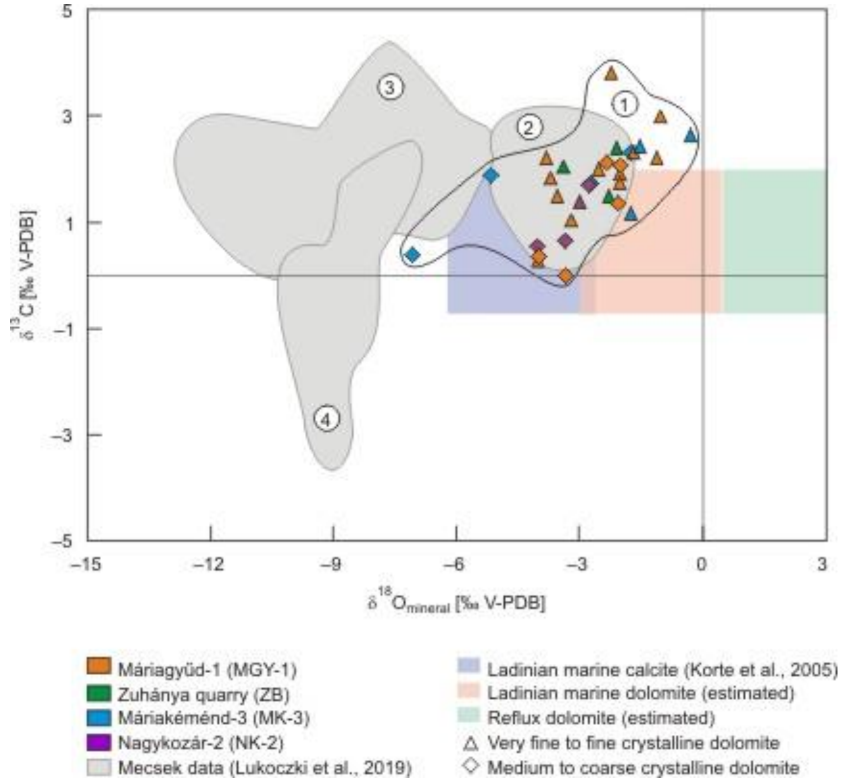

Fig. 7: Carbon and oxygen isotope plot for matrix dolomites. The colored symbols refer to the type and location of the samples. The colored rectangles display the composition of dolomites as estimated on the basis of literature data (Land, 1980; Korte et al., 2005) representing various precipitating fluids (see legend). The gray shading covers data from the Mecsek Mts. (Lukoczki et al., 2019). 1: Csukma Dolomite Member, 2: Reflux dolomites recrystallized in an intermediate burial setting (Kán Dolomite Member, Mecsek Mts.), 3: Dolomites formed and/or recrystallized in fault-related fluids (Kán Dolomite and Kozár Limestone Members, Zuhánya Limestone Formation, Mecsek Mts.), 4: Recrystallized limestones (Kozár Limestone Member).

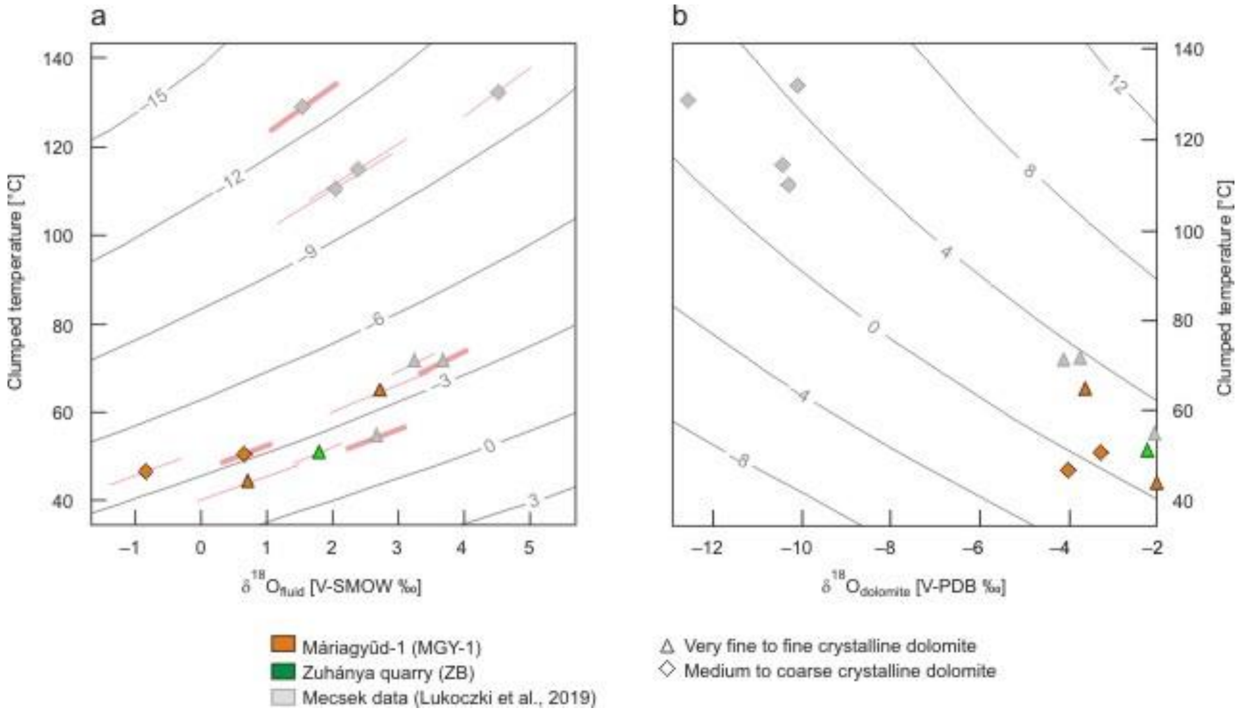

Fig. 8: Plots for clumped isotope data measured on matrix dolomite samples and the corresponding temperatures. **(a)** Relationship between temperatures converted from Δ_{47} and calculated δ^{18}O values of the diagenetic fluids. Red bars indicate ±1SE. **(b)** Relationship between temperatures converted from Δ_{47} and measured δ^{18}O of matrix dolomites.

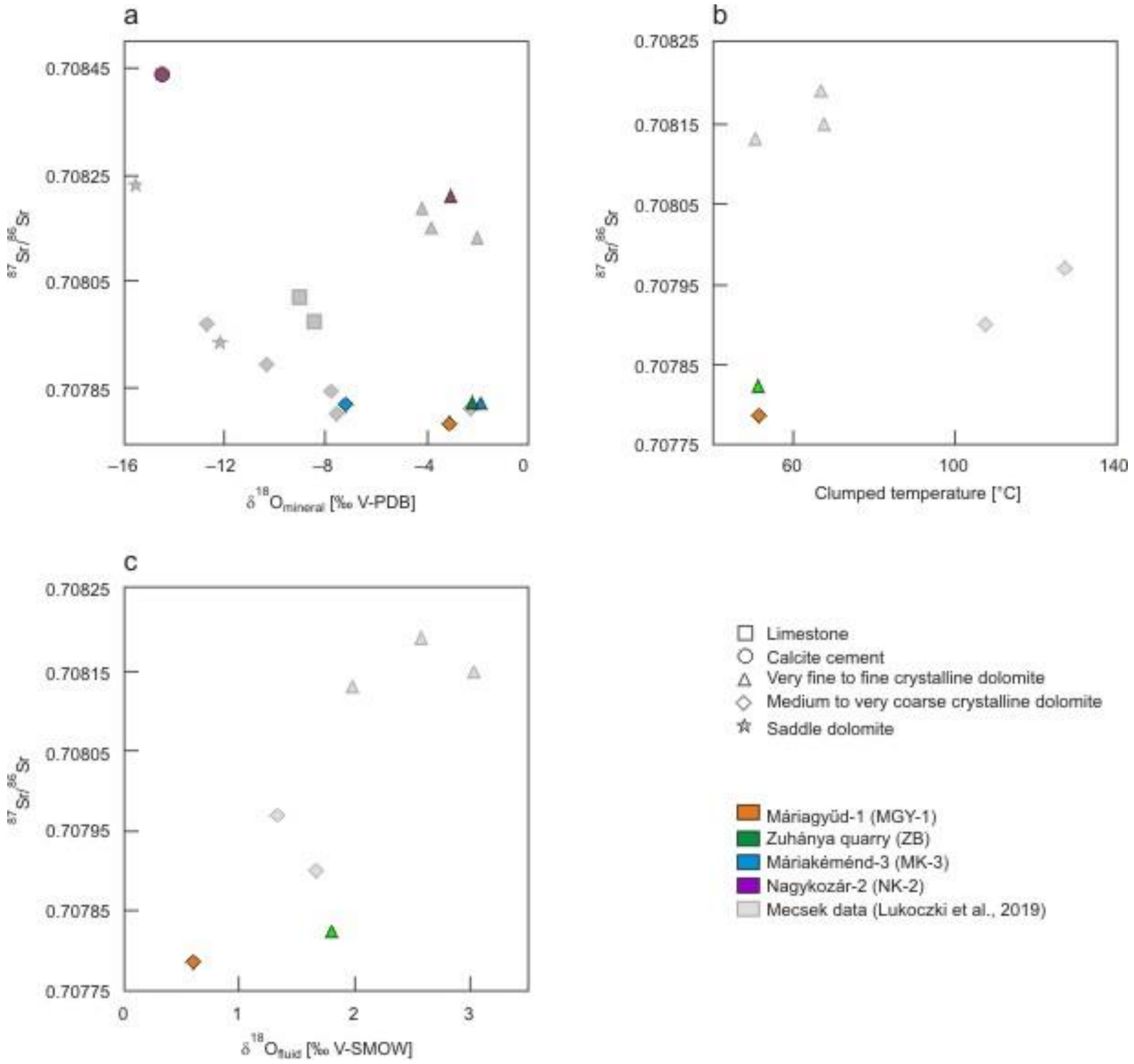

Fig. 9: Plots of Sr isotope vs. **(a)** δ^{18}O values of dolomite and calcite samples; **(b)** temperatures converted from Δ_{47} and **(c)** δ^{18}O values of diagenetic fluids.

CHAPTER III

INTERPRETATION OF RECRYSTALLIZATION PROCESSES OF SEDIMENTARY DOLOMITES AS DEDUCED FROM CRYSTAL STRUCTURAL AND GEOCHEMICAL DATA

Abstract

Most sedimentary dolomites are meta-stable upon formation and either transform into more stable dolomite via recrystallization, or persist as meta-stable phases over deep geological time. How recrystallization alters the crystal structure and chemistry of dolomite remains poorly understood. Geochemical data and unit cell parameters obtained by Rietveld refinement of conventional and high-resolution X-ray and neutron diffraction data collected on recrystallized Middle Triassic sedimentary dolomites (Csukma Formation) of SW Hungary suggest that recrystallization with high water to rock ratio versus recrystallization in low water to rock ratio may be reflected in the unit cell dimensions of recrystallized dolomites. Recrystallization processes with low water to rock ratio may result in a noticeable trend between crystal size and unit cell parameters that cannot be explained by Ostwald ripening. In samples recrystallized with high water to rock ratios compositionally indistinguishable overgrowth cement on the matrix dolomite may have a significant effect on the overall unit cell dimensions determined from powder diffraction analyses.

3.1. Introduction

Dolomite [$CaMg(CO_3)_2$] is a common rock-forming mineral; however, its formation in sedimentary environments is still poorly understood despite its long history of research. In the process of dolomitization limestone ($CaCO_3$) is transformed to dolomite rock (also called dolostone in order to distinguish the rock and the mineral). Dolomitization happens in several ways and in a number of diagenetic environments (e.g., Machel, 2004). In almost all of these Mg is added to limestone during local or regional flow of Mg-rich fluid, and the process can be interpreted from the geochemistry of the dolomites. However, if the rock is recrystallized, the textures and various geochemical parameters of the dolomites may lead to erroneous genetic interpretations (Land, 1980; Machel, 1997). Therefore, recognizing and understanding recrystallization of dolomite is crucial to understanding its origin.

Most dolomites formed in near-surface settings are meta-stable (poorly ordered and/or Ca-rich) upon formation, and either transform into more stable (ordered and stoichiometric) dolomite via recrystallization, or persist as a meta-stable phase over deep geological time (Gregg et al., 2015). Since solid-state reactions proceed very slowly under diagenetic conditions (up to ca. 300 °C), low-temperature recrystallization of dolomites is believed to occur through dissolution–re-precipitation processes involving a thin aqueous solution film between the dissolving and precipitating phases (Land, 1980). Limited evidence suggests correlation between the chemical composition and crystallographic properties of recrystallized dolomites; however, the relationship with the underlying geological processes is poorly understood (e.g., Gregg et al., 1992; Malone et al., 1994; Turpin et al., 2012).

Recrystallization of non-stoichiometric and/or disordered dolomite is thermodynamically driven to achieve a lower standard free energy associated with ordered, stoichiometric dolomites (Carpenter, 1980; Navrotsky and Capobianco, 1987). Dolomite recrystallization is also believed to be surface energy driven (cf., Ostwald ripening; Gregg et al., 1992; Morse and Casey, 1998). During recrystallization various rock characteristics, such as texture, and geochemical characteristics, may undergo changes to some extent (cf., the concept of ‘significant recrystallization’ of Machel, 1997).

Recrystallization of sedimentary dolomites is normally inferred by abductive reasoning based on the assumption that the original characteristics of the studied dolomite were similar to modern analogues. That is, if the observed chemical (stoichiometry, trace element content, stable isotope values), crystal structural (ordering, unit cell parameters), textural (crystal size, type of crystal boundaries), etc. characteristics of the studied dolomite differ from those typically observed in modern analogs, it is inferred that the dolomite has undergone recrystallization (cf., Kaczmarek and Sibley, 2014).

The crystal structural characteristics of natural recrystallized sedimentary dolomites have not been investigated in detail using advanced diffraction techniques. Neutron diffraction has been used to investigate various aspects of dolomite crystallography: residual stress and strain in dolomite (Scheffzük et al., 2001), high temperature decomposition of dolomite (Aza et al., 2002), and texture and structure studies on marbles (Filabozzi et al., 2006). Synchrotron X-ray studies have been used to investigate solid-state transformation processes of dolomite during in-situ high temperature and pressure experiments (Martinez et al., 1996; Antao et al., 2004; Franzolin et al., 2012; Zucchini et al., 2014).

The goal of this study is to identify any correlation between the crystal structure and the geological environment of recrystallization as inferred from petrological and geochemical data. Middle Triassic dolomites of SW Hungary that are inferred to have formed and recrystallized under various geological conditions were selected for high-resolution diffraction study to identify crystallographic variability in recrystallized dolomites. The use of synchrotron radiation is particularly advantageous to study sedimentary dolomites since most sedimentary dolomites that formed in near-surface environments are very fine crystalline and are not suitable for single crystal studies. Neutron powder diffraction is an ideal tool to study the crystal structure of dolomite because of its efficiency of scattering light elements. Joint Rietveld refinement of synchrotron X-ray and neutron diffraction data allows precise calculation of crystal structure parameters.

3.1.1. Dolomite crystal chemistry

The mineral dolomite can be represented in either the rhombohedral or the hexagonal axial system, but now it is standard to use the hexagonal system (Fig. 1.). Dolomite belongs to the $R\overline{3}$ space group (No. 148 in the International Table of Crystallography, Vol. A). The hexagonal unit cell of dolomite contains three $CaMg(CO_3)_2$ groups. The Ca and Mg atoms are situated on special positions: 3a (0, 0, 0) for Ca, and 3b (0, 0, ½) for Mg. C is on the 6c position (0, 0, z), and O is on a general position (18f: x, y, z). Unit cell parameters of a maximally ordered, stoichiometric dolomite were determined by Reeder and Wenk (1983) to be a=4.8078 Å, c=16.002 Å.

Wyckoff and Merwin (1924) were the first to determine that dolomite is not a member of a solid solution between calcite ($CaCO_3$) and magnesite ($MgCO_3$), both of which belong to the $R\overline{3}c$ space group. Dolomite has a distinct crystal structure in which separate layers of Ca and Mg alternate with layers of the CO_3 anion group (Fig. 1). The main structural difference between dolomite and calcite is this layered arrangement of the Mg atoms in dolomite, whereas in calcite, if Mg is present, it randomly substitutes for Ca. This ordered arrangement of the Mg atoms forbids the c-glide plane, which is present in the calcite structure.

The CO_3 group can be represented as an equilateral triangle, in which the oxygen atoms are situated at the corners, and the carbon atom is in the center. In calcite these four atoms are in the same plane, but in dolomite, the carbon atom is displaced from the plane formed by the oxygen triangle. This displacement is toward the Mg layer due to the difference in charge density between Ca and Mg (Reeder and Wenk, 1983). The C–O bond length is essentially the same as in calcite; however, the Ca–O and Mg–O bond lengths are different, because the oxygen is closer to the magnesium. This difference in bond length causes rotation of the CO_3 groups. The CO_3 groups are uniformly rotated by 6.6° around their three-fold axis in a given layer. This rotation is the reason for the oxygen being on a general position in the dolomite structure. The rotation of the CO_3 group forbids the three two-fold axes present in calcite (Reeder, 1983).

3.1.2. Cation order in dolomites

In a stoichiometric dolomite, the number of A sites and B sites are equal, and if the dolomite is ordered, all Ca occupies A sites, and all Mg occupies B sites. However, many natural dolomites contain excess $CaCO_3$ causing disturbance in compositional ordering (Reeder, 1983).

The degree of compositional order is given by fractional occupancies of each distinct cation site. Reeder (2000) used the following formula to determine the order parameter (S) of sedimentary dolomites:

$$S = \frac{2X_{Ca}^{A} - X_{Ca}^{B}}{2 - X_{Ca}^{T}},$$

where X_{Ca}^{A} is the refined fractional occupancy of Ca in the A site, and X_{Ca}^{T} is the total Ca atoms per formula unit. S is 0 for complete disorder, and 1 for maximum order.

Reeder (2000) found mixed Ca-Mg occupancy on A and B sites of studied excess-Ca dolomites based on Rietveld refinement of X-ray diffraction data collected on single dolomite crystals. In contrast, Drits et al. (2005) found that A sites are only occupied by Ca, and the excess Ca is located at the B sites. In their study, occupancies of the A and B sites were refined using constraints based on the Ca excess determined by inductively-coupled plasma–atomic emission spectoscropy, X-ray fluorescence spectroscopy and electron-microprobe analysis.

Positional ordering in dolomite is related to the orientation of the CO_3 groups. Since the rotation of the CO_3 group is caused by the ordered arrangement of the Ca and Mg layers, there is a relationship between rotational angle of the CO_3 group and cation disorder: with increasing cation disorder the rotation of the CO_3 group approaches 0° (Reeder and Wenk, 1983).

3.1.3. Methods of estimating dolomite stoichiometry

Goldsmith and Graf (1958) were the first to suggest that a linear relationship exist between the d-spacings and the chemical compositions of the dolomites, i.e., dolomite stoichiometry in terms of mol% excess $CaCO_3$, as a result of Ca substituting for Mg. Based on this relationship, various methods were developed to estimate dolomite stoichiometry and ordering. Lumsden (1979) derived this linear relationship, which became widely accepted to calculate dolomite stoichiometry. In the following decades, however, a number of researchers found dolomites whose composition did not fall on the Lumsden line (e.g., Reeder and Sheppard, 1984; Jones et al., 2001). Therefore, Jones et al. (2001) suggested a method based on peak-fitting that is applicable for heterogeneous samples (i.e., more than one dolomite phase is present, such as matrix dolomite and dolomite cement).

Turpin et al. (2012) suggested a new way to estimate dolomite stoichiometry based on unit cell parameters determined by Rietveld refinement. Their method is based on the linear correlation between a(=b) and c parameters and $CaCO_3$ mol% content of the dolomite. Their empirical calibration is based on a collection of dolomite cell parameters, mostly from literature, determined by various methods. The mol% of $CaCO_3$ is calculated based on the linear regression from the refined cell parameters.

3.2. Geological setting

The Csukma Formation in the Mecsek Mts. and Villány Hills in SW Hungary (Fig. 2) are made up of dolomites, limestones, and dolomitic limestones that were deposited in shallow marine to peritidal environments during the Middle Triassic (Fig. 3). These rocks display evidence of complex diagenetic processes in response to differing burial histories of the Mecsek Mts. and the Villány Hills. The peritidal Kán Dolomite Member (KDM) in the Mecsek Mts. was dolomitized penecontemporaneously by refluxing evaporatively concentrated seawater during the Middle Triassic (Lukoczki et al., 2019). The partly coeval and younger Csukma Dolomite Member (CDM) in the Villány Hills, however, was dolomitized via geothermal circulation of near-normal seawater in a near-surface to shallow burial setting (Lukoczki et al., *in prep*). The early dolomites of the Mecsek Mts. underwent burial recrystallization in intermediate burial setting with low water to rock ratios, which was followed by a second, fault-controlled recrystallization event with high water to rock ratios during the Early Cretaceous when seawater was drawn down through rift-related submarine faults. This Cretaceous seawater was likely heated up due to geothermal heat and was convected along faults resulting in recrystallization of preexisting dolomites of the KDM for a second time, and in pervasive dolomitization of the coeval middle ramp carbonates (Kozár Limestone Member) and the underlying Zuhánya Limestone (Fig. 3) in the vicinity of the faults (Lukoczki et al., 2019). Due to marked differences in the burial history of the Mecsek Mts. and the Villány Hills, evidence for this fault-controlled dolomitization and recrystallization event is missing in the Villány Hills. Here, the dolomites of the CDM were recrystallized with low water to rock ratios in intermediate burial setting without reaching complete recrystallization before uplift due to the onset of the Late Cretaceous compressional tectonics (Lukoczki et al., *in prep*.).

3.3. Materials and methods

Representative dolomite samples of the Csukma Formation were selected for crystallographic analysis based on their sedimentary, textural and chemical properties and diagenetic history (Fig. 4). The petrographic and isotope geochemical methods applied to identify the various dolomite types and to reconstruct the diagenetic history are discussed in detail in Lukoczki et al. (2019; *in prep*.). Throught the paper, the term 'matrix dolomite' is used to refer to dolomites that were formed via replacement of a precursor calcium carbonate phase. The term 'dolomite cement' refers to dolomite phases that were directly precipitated into an open void. The term 'crystal size' is used in this study to refer to the size of the dolomite crystals that make up the dolomite rock as observed in thin sections (not to be confused with the term 'crystallite size,' which refers to the size of the particles in powder diffraction samples). Mean crystal sizes were determined from 40 crystal size measurements on each matrix dolomite sample optically from thin sections using the QuickPHOTO CAMERA 3.0 software marketed by CPX-SOLUTIONS by CANIMPEX Enterprises Ltd. Due to the limited amounts of available samples and the large sample size needed for the neutron diffraction analysis, the high-resolution diffraction measurements were performed on geologically equivalent samples of those analyzed by conventional XRD and ICP-MS (Table 1).

3.3.1. Geochemical methods

Chemical homogeneity of the samples selected for the high-resolution diffraction analysis were investigated with a multi-segment solid state diode backscattered electron detector (BSED) that is manually fixed on a FEI Quanta 600F field emission environmental scanning electron microscope (ESEM) at Oklahoma State University. The rock slabs were prepared for analysis using a JEOL IB-19500CP cross section ion beam polisher at Oklahoma State University.

Elemental composition of dolomite powder samples were measured in the Canadian Centre for Isotopic Microanalysis at the University of Alberta using a Perkin-Elmer Elan 6000 quadrupole Inductively Coupled Plasma – Mass Spectrometer (ICP-MS). The samples (~50–100 mg) were dissolved in 8 N HNO_3 (~5 ml) using Savillex beakers and were placed on a hot plate (100 °C) overnight. Solutions were subsequently diluted with 1% HNO_3 to a volume of 90 ml. Prior to ICP-MS analysis, internal standards (In, Bi, and Sc) were added and sample solutions were diluted (with 1% HNO_3) by a factor of 10.

Carbonate clumped isotopes were measured in the Clumped Isotope Laboratory at Imperial College London on a Thermo Fisher MAT 253 isotope ratio mass spectrometer in dual inlet mode, using the methodology described in Dale et al. (2014). Isotopic corrections and normalization was performed using the software Easotope (John and Bowen, 2016), using heated gases and the ETH carbonates (Meckler et al., 2014) as standards. For the evaluation of geological processes, the Δ_{47} values were converted to temperature using the calibration of Davies and John (2019) and are presented in °C.

3.3.2. Diffraction methods

Conventional powder X-ray diffraction (XRD) data were obtained using a Bruker Advance D8 diffractometer equipped with a LYNXEYE detector (D8-25 ADVANCE Bruker AXS GmbH) with CuKα radiation (X-ray tube operated at 40 kV and 40 mA) filtered by a 0.02 mm Ni foil at Oklahoma State University in reflection geometry. Data were collected in the angular range of 5–140° 2θ with 0.02° step size and 2 s counting time per step.

High resolution synchrotron powder diffraction data were collected using beamline 11-BM at the Advanced Photon Source (APS), Argonne National Laboratory using an average wavelength of 0.412726 Å in transmission geometry. Discrete detectors covering an angular range from –6 to 16 º 2θ are scanned over a 34º 2θ range with data points collected every 0.001º 2θ and scan speed of 0.01º/s. The powder samples were loaded into Kapton Capillary Tube sample holders of 0.8 mm diameter. The data were collected under ambient conditions.

Neutron powder diffraction data were collected using the BT-1 32 detector neutron powder diffractometer at the NIST Center for Neutron Research reactor, NBSR, in transmission geometry. A Cu(311) monochromator with a 90° take-off angle, λ = 1.5399(2) Å, and in-pile collimation of 15 minutes of arc were used. Data were collected over the range of 3–168° 2θ with a step size of 0.05°. Ten g of dolomite powder sample was loaded in a vanadium can sample container of length 50 mm and diameter 12.4 mm. The data were collected under ambient conditions.

3.3.3. Rietveld refinement

Rietveld refinements were perfomed using GSAS-II (General Structure Analysis System) (Toby and Von Dreele, 2013) with the structure model of Reeder and Wenk (1983) (ICSD 31209). The background was fitted using the Chebyschev function (Larson & Von Dreele, 2004) with four coefficients. Rietveld refinements were performed using an axial-divergence-broadened pseudo-Voigt profile function with the analytic Hessian least-squares routine (Toby and Von Dreele, 2013). The quality of the fit was determined visually and based on the discrepancy value wR. The wR factor is calculated as the square root of the quantity being minimized and is scaled by the weighted intensities (Toby, 2012). The refined sample parameters include histogram scale factor, unit cell parameters (a, c and volume), strain and crystallite size. In addition, for the conventional XRD dataset, sample displacement and preferred orientation for the 104 reflection were also determined. The total number of parameters refined ranged between 9 and 13 for the conventional XRD data, and 16 parameters were refined for the high-resolution dataset. Stoichiometry of the samples was calculated from the refined unit cell parameters using the method of Turpin et al. (2012).

3.4. Results

Refinement discrepancy values, refined unit cell parameters obtained with Rietveld refinement of the conventional XRD, and the joint refinement of the synchrotron X-ray and neutron diffraction data are presented in Table 1 along with values of $CaCO_3$ mol%, Ca/Mg molar ratios, Fe, Mn and Sr content, average crystal sizes and clumped isotope temperatures. The content of the crystallographic information files (CIFs) obtained as the results of the Rietveld refinements are included in Appendix 1. Appendix 2 contains the full list of the results of the elemental analysis.

3.4.1. Sample composition

BSE analysis of the samples indicate that the dolomites are chemically homogenous within the limits of the method. Trace and minor amounts of calcite inclusions were found within the matrix dolomites in samples HH-2/1, and VA-7, respectively. Rietveld refinement indicate the presence of 0.04%wt. calcite in HH-2/1, and 2.12%wt. calcite in VA-7. All other samples in the high-resolution diffraction sample set are pure dolomite (Fig. 5 & 6).

3.4.2. Rietveld refinements

The quality of fit for the Rietveld refinements was evaluated visually as well as using the standard discrepancy values such as the wR factor. The visual evaluation as well as the values describing the discrepancy between the observed pattern and the modelled pattern (Table 1) indicate a moderate fit primarily due to the poor fit of the background, intensity mismatch of several peaks and, in the synchrotron dataset, a noticeable asymmetry of the peaks. The fit of the peak positions, however, is good, which allows accurate determination of the unit cell parameters.

3.4.3. Unit cell parameters

In the high-resolution dataset, the length of the a crystallographic axis ranges from 4.80870 Å to 4.81447 Å, the length of the c crystallographic axis ranges from 16.01154 Å to 16.04699 Å, and the unit cell volume ranges from 320.642 to 322.112 Å^3. In the conventional XRD dataset, the same parameters range for a from 4.80838 Å to 4.81918 Å, for c from 16.01299 Å to 16.10199 Å, and for the unit cell volume from 320.637 Å^3 to 323.859 Å^3. All studied dolomite samples have expanded unit cells compared to the reference data of Reeder and Wenk (1983).

3.4.4. Stoichiometry and minor element content

$CaCO_3$ mol% of the dolomite samples calculated from the elemental composition correspond well with the $CaCO_3$ mol% determined from the unit cell parameters using the method of Turpin et al.

(2012) (Table 1). Based on the calculations from the c unit cell parameter, all samples are excess-Ca dolomites, with $CaCO_3$ mol% ranging from 50.80 mol% to 55.32 mol%. The linear relationship between the unit cell parameters and the Ca-Mg ratio is apparent in Fig. 7 with increasingly expanded unit cell corresponding with increasing Ca content. All studied samples have low minor/trace element content (Table 1) and regression analysis did not show a statistically significant correlation between the minor/trace element content and the unit cell parameters (Fig. 8).

3.4.5. Crystal size and clumped isotope temperatures

The results of conventional XRD indicate a slight trend within the low-temperature dolomites of increasing crystal size with a slight expansion of the unit cell (Fig. 9a). However, the high-temperature, fault-controlled dolomites, which are characterized by the coarsest crystal sizes, do not follow this trend but have unit cell dimensions that fall at the lower end of the range (Fig. 9a). The low number of samples in the high-resolution dataset does not allow the identification of clear trends. However, within the dataset, the coarse crystalline dolomites are characterized by the most contracted unit cells (Fig. 9b). There is no clear trend between the clumped isotope temperature and the unit cell parameters (Fig. 10); however, the high-temperature dolomites, as also suggested by the correlation with the crystal sizes, are characterized by lower unit cell volumes within the dataset.

3.5. Discussion

It has been well documented that sedimentary dolomites typically contain Ca in excess of the ideal one to one ratio relative to Mg (e.g., Goldsmith and Graf, 1958; Reeder and Sheppard, 1984;

Reeder, 2000; Drits et al., 2004). Since the formation of excess-Ca dolomite is energetically unfavorable, its formation is likely kinetically controlled (Navrotsky and Capobianco, 1987; Chai et al., 1995) Results of high-resolution transmission electron microscopy studies suggest that the excess Ca is associated with structural modulations and other defective layer-structures on the 100 to few 100 Å scale (Wenk et al., 1983; 1993; Reeder, 1992). Reeder (2000) suggested that the poor fit of the Rietveld refinement in the case of Ca-rich dolomites might be due to these structures, which cannot be modeled properly with the Rietveld method, since diffraction data represent spatial averages of such structures. Using Rietveld refinement of conventional XRD data and simulations of the XRD patterns Drits et al. (2005), however, characterized the defective layer-structures within excess-Ca dolomites by the mixed-layer model. According to this model, calcite-like, stoichiometric dolomite, and non-stoichiometric dolomite layers are randomly interstratified. They found that dolomite phases with higher amounts of excess Ca are structurally more ordered than dolomite phases with lower amounts of excess Ca. The higher degree of regularity may be due to lower strain where increased amounts of Ca occur on the Mg site because fewer Ca on the Mg site have less pronounced structure control on the growth layers (Drits et al., 2005).

Reeder and Sheppard (1984) studied the relationship between unit cell parameters and composition, i.e., Ca excess. They found that a and c lattice parameters are relatively insensitive for low amounts of Ca excess (up to 52.5 mol% $CaCO_3$), but in the case of higher amounts of Ca excess, they observed a positive correlation, i.e., the more Ca, the more expanded the unit cell is. According to their observations, ca. 3 mol% excess Ca is needed to induce appreciable changes in the lattice parameters. The results of the current study, however, indicate that lower levels of Ca excess are sufficient to affect the size of the unit cell since only three of the analyzed samples have Ca excess more than 3% and a correlation between the unit cell parameters and the Ca-Mg ratio is apparent nevertheless (Fig. 7)

High-temperature studies indicate that the magnitude of change in the unit cell parameters of thermally disordered dolomites that underwent recrystallization in the solid state is lower than the range of unit cell parameters in natural sedimentary dolomites (Reeder and Wenk, 1983; Reeder and Sheppard, 1984). Furthermore, most sedimentary dolomites, either stoichiometric or calcian, have expanded unit cells compared to the parameters measured on ideally ordered single dolomite crystals (Reeder and Sheppard, 1984). This suggests that the scatter in the unit cell parameters of sedimentary dolomites is not only determined by cation ordering and stoichiometry but by other factors as well, such as positional disorder of the CO_3-group (Reeder and Sheppard, 1984). Such other factors may also include twinning, as suggested by transmission electron microscopy study of dolomites (Miser et al., 1987). In the case of a stoichiometric dolomite, twinning induced strain may result in unit cell expansion. Since the twin domains scatter X-rays incoherently, they do not appear in the diffraction pattern. Twins and other defective structures are typically (but not exclusively) associated with matrix dolomites. Therefore, matrix dolomites may have more expanded unit cells than cement dolomites due to the presence of such defective structures even if the composition (stoichiometry) of these dolomite types is the same.

In the case of the coarse crystalline dolomites in the Mecsek Mts., CL zonation of the rims of the dolomite crystals (Fig. 4) suggest that they were directly precipitated as cement overgrowth on the matrix dolomite cores. It is, therefore, possible that the reason why most of the finer crystalline dolomites in the Mecsek Mts. and Villány Hills have more expanded unit cells than the coarse crystalline dolomites may be due to the presence of more of such defective structures compared to the coarse crystalline dolomites where significant portions of the dolomite crystals were likely directly precipitated from the high-temperature solutions as cements rather than replacement. In matrix dolomites defective structures may be introduced into the dolomite lattice due to the anion orientation of the mineral that is being replaced (Gunderson and Wenk, 1981). It is possible that such defective structures are preserved to some degree in recrystallized dolomites.

Bimodal intensity distributions (i.e., double peaks) have been shown to indicate the presence of two dolomite phases with distinct excess-Ca content (e.g., Jones et al., 2001; Drits et al., 2005). BSE analysis of the dolomites of Jones et al. (2001) and Drits et al. (2005) confirmed the compositional heterogeneity of their samples. In the samples of the current study neither compositional zonation with BSE nor double peaks in the high-resolution dataset were observed indicating that the studied samples are compositionally homogeneous. A possible exception is sample MGY-1 381.5 m. In this sample the 018 and 116 reflections have broad shoulders towards the lower 2θ values, which may indicate the presence of two dolomite populations although BSE observations suggest a homogenous composition. This sample also has the most expanded unit cell in the high-resolution dataset, and the third largest in the conventional XRD dataset.

Fe^{2+} and Mn^{2+} are important minor elements in dolomites and are mainly responsible for quenching and activating cathodoluminescence, respectively, even when present in low concentrations (e.g., Machel et al., 1991). These minor elements, especially Fe, may be present in large enough concentrations to affect the crystal structure of dolomite. Elements with distribution coefficients >1, such as Fe^{2+} and Mn^{2+}, will be concentrated in the crystal phase during diagenesis (Veizer, 1983), thus, increasing concentration of these elements is expected with increasing crystal size during progressive recrystallization. Elements with distribution coefficients <1, such as Sr^{2+}, will be concentrated in the solution during precipitation and successive recrystallization is expected to result in depletion of these elements (Land, 1980). According to Goldschmidt's rule of substitution, Fe^{2+} and Mn^{2+} are expected to substitute for Mg in the dolomite lattice since both Fe^{2+} and Mn^{2+} have ionic radii smaller than Mg^{2+}, which in turn has smaller ionic radius than Ca^{2+}. Sr^{2+}, however, is larger than Ca^{2+}, therefore, it likely substitutes for Ca^{2+}. The concentration of these elements (Table 1), however, is too low to affect the unit cell parameters of the studied dolomites appreciably, which is indicated by the lack of correlation between the Fe, Mn and Sr content and the unit cell parameters (Fig. 8).

The clumped isotope composition of the dolomites of the Csukma Formation display a trend that indicates that recrystallization occurred at low water to rock ratios in the case of the low-temperature, fine crystalline dolomites (Lukoczki et al., *in prep*). The high-temperature, coarse crystalline dolomites, on the other hand, likely recrystallized in fluids that advected through faults, i.e., the water to rock ratios were likely much larger than in the case of the lower temperature dolomites (Lukoczki et al., 2019). This may explain why there is a slight but distinct trend in the fine crystalline (low-temperature) dolomites that indicate increasing unit cell dimensions with increasing crystal size. A study of recrystallized dolomites in the Monterey Formation (Miocene, California) suggests that progressive recrystallization resulted in increased crystal sizes and decreased unit cell dimensions (Malone et al., 1994). Based on this, the more recrystallized the dolomite, the more contracted the unit cell is expected to be. The trend, albeit not very pronounced, is opposite in the current study in the case of the low-temperature recrystallized dolomites. Recrystallization of these samples were interpreted to have been driven thermodynamically by high defect energy due to less than ideal stoichiometry and ordering, and/or reduction of surface free energy (Ostwald ripening), and kinetically facilitated by the increased temperature associated with the burial of the succession (Lukoczki et al., *in prep.*). Such processes are expected to reduce the amount of the defect structures as well as to result in more ideal stoichiometry along with increased crystal sizes (cf., Gregg and Shelton, 1990; Gregg et al., 1992). A possible explanation for the higher Ca content and accordingly more expanded unit cells in the coarser crystalline low-temperature dolomites may be that these dolomites originally formed as more stable dolomite phases compared to the finer crystalline dolomites, and therefore might have been less prone to recrystallization than their finer crystalline counterparts. This implies that the coarser crystalline dolomites within the low-temperature dolomite population may reflect more of an original Ca-Mg ratio, whereas the finer crystalline dolomites were formed originally as less stable dolomite phases that recrystallized more readily. Therefore, the lower amounts of excess Ca of the finer crystalline dolomites may reflect a “purification” process due to recrystallization.

In the case of the high-temperature, coarse crystalline dolomites, the interaction with hot fluids not only kinetically facilitated recrystallization of the precursor dolomites but also resulted in precipitation of overgrowth cements on the matrix dolomites as well as fracture and vug filling saddle dolomite cements. The homogenous composition of the matrix dolomites of these samples, as indicated by the BSE and diffraction analyses, suggests that recrystallization of the matrix dolomite and precipitation of the dolomite cements occurred in the presence of the same fluid.

3.6. Conclusions

Geochemical and crystal structure analysis of recrystallized dolomites of the Csukma Formation, SW Hungary, suggest that recrystallization with high water to rock ratio in the coarse crystalline, high-temperature dolomites versus low water to rock ratio in the fine crystalline, low-temperature dolomites may be reflected in the unit cell dimensions of such dolomites. Recrystallization processes with low water to rock ratio result in a noticeable trend between crystal size and unit cell parameters that cannot be explained by Ostwald ripening. This may be due to differences in stability of the precursor dolomite. In other words, the finest crystalline dolomites might have formed originally as less stable (more Ca-rich, less ordered) and therefore likely recrystallized more readily than the somewhat coarser crystalline dolomites that might have formed originally as more stable dolomite phases. Therefore, the lower Ca content and the more contracted unit cells of the finer crystalline dolomites likely reflect a more significant recrystallization than the coarser crystalline dolomites in the low-temperature sample set. In the high-temperature, coarse crystalline samples the most contracted unit cells may reflect the contribution of presumably well-ordered dolomite cement overgrowth on the matrix dolomites.

Acknowledgements

Use of the Advanced Photon Source at Argonne National Laboratory was supported by the U. S. Department of Energy, Office of Science, Office of Basic Energy Sciences, under Contract No. DE-AC02-06CH11357. We acknowledge the support of the National Institute of Standards and Technology, U.S. Department of Commerce, in providing the neutron research facilities used in this work. Help of David Bish with the Rietveld refinements and Brent Johnson with the SEM-BSE analysis is much appreciated.

References

Antao, S.M., Mulder, W.H., Hassan, I., Crichton, W.A. and Parise, J.B., 2004. Cation disorder in dolomite, $CaMg(CO_3)_2$, and its influence on the aragonite+ magnesite↔ dolomite reaction boundary. American Mineralogist, 89(7): 1142-1147.

Aza, A.H., Rodríguez, M.A., Rodríguez, J.L., Aza, S., Pena, P., Convert, P., Hansen, T. and Turrillas, X., 2002. Decomposition of dolomite monitored by neutron thermodiffractometry. Journal of the American Ceramic Society, 85(4): 881-888.

Carpenter, A.B., 1980. The Chemistry of Dolomite Formation I: The Stability of Dolomite. In: D.H. Zenger, J.B. Dunham and R.L. Ethington (Editors), Concepts and Models of Dolomitization. SEPM.

Chai, L., Navrotsky, A. and Reeder, R., 1995. Energetics of calcium-rich dolomite. Geochimica et Cosmochimica Acta, 59(5): 939-944.

Dale, A., John, C.M., Mozley, P.S., Smalley, P.C. and Muggeridge, A.H., 2014. Time-capsule concretions: Unlocking burial diagenetic processes in the Mancos Shale using carbonate clumped isotopes. Earth and Planetary Science Letters, 394(Supplement C): 30-37.

Davies, A.J. and John, C.M., 2019. The clumped ($^{13}C^{18}O$) isotope composition of echinoid calcite: Further evidence for “vital effects” in the clumped isotope proxy. Geochimica et Cosmochimica Acta, 245: 172-189.

Drits, V.A., McCarty, D.K., Sakharov, B. and Milliken, K.L., 2005. New insight into structural and compositional variability in some ancient excess-Ca dolomite. The Canadian Mineralogist, 43(4): 1255-1290.

Filabozzi, A., Andreani, C., De Pascale, M.P., Gorini, G., Pietropaolo, A., Cippo, E.P., Senesi, R., Tardocchi, M. and Kockelmann, W., 2006. Texture and structure studies on marbles from Villa Adriana via neutron diffraction technique. Journal of Neutron Research, 14(1): 55-58.

Franzolin, E., Merlini, M., Poli, S. and Schmidt, M.W., 2012. The temperature and compositional dependence of disordering in Fe-bearing dolomites. American Mineralogist, 97(10): 1676-1684.

Goldsmith, J. and Graf, D., 1958. Relation between lattice constants and composition of the Ca-Mg carbonates. American Mineralogist, 43(1-2): 84-101.

Gregg, J.M., Bish, D.L., Kaczmarek, S.E. and Machel, H.G., 2015. Mineralogy, nucleation and growth of dolomite in the laboratory and sedimentary environment: A review. Sedimentology, 62(6): 1749-1769.

Gregg, J.M., Howard, S.A. and Mazzullo, S., 1992. Early diagenetic recrystallization of Holocene (< 3000 years old) peritidal dolomites, Ambergris Cay, Belize. Sedimentology, 39(1): 143-160.

Gregg, J.M. and Shelton, K.L., 1990. Dolomitization and dolomite neomorphism in the back reef facies of the Bonneterre and Davis formations (Cambrian), southeastern Missouri. Journal of Sedimentary Research, 60(4).

Gunderson, S. and Wenk, H., 1981. Heterogeneous microstructures in oolitic carbonates. American Mineralogist, 66(7-8): 789-800.

International Tables for Crystallography (2016). Vol. A, Chapter 2.3, 193–687.

John, C.M. and Bowen, D., 2016. Community software for challenging isotope analysis: First applications of ‘Easotope’to clumped isotopes. Rapid Communications in Mass Spectrometry, 30(21): 2285-2300.

Jones, B., Luth, R.W. and MacNeil, A.J., 2001. Powder X-ray diffraction analysis of homogeneous and heterogeneous sedimentary dolostones. Journal of Sedimentary Research, 71(5): 790-799.

Kaczmarek, S.E. and Sibley, D.F., 2014. Direct physical evidence of dolomite recrystallization. Sedimentology, 61(6): 1862-1882.

Land, L.S., 1980. The Isotopic and Trace Element Geochemistry of Dolomite: The State of the Art. In: D.H. Zenger, J.B. Dunham and R.L. Ethington (Editors), Concepts and Models of Dolomitization. SEPM, pp. 87-110.

Larson, A. and Von Dreele, R., 2004. Los Alamos Natl. Lab. Rep. Laur, 86: 748.

Lukoczki, G., Haas, J., Gregg, J.M., Machel, H.G., Kele, S. and John, C.M., 2019. Multi-phase dolomitization and recrystallization of Middle Triassic shallow marine–peritidal carbonates from the Mecsek Mts. (SW Hungary), as inferred from petrography, carbon, oxygen, strontium and clumped isotope data. Marine and Petroleum Geology, 101: 440-458.

Lukoczki, G., Haas, J., Gregg, J.M., Machel, H.G., Kele, S. and John, C.M., in prep. Early dolomitization and partial burial recrystallization: A case study of Middle Triassic peritidal dolomites in the Villány Hills (SW Hungary) using petrography, carbon, oxygen, strontium and clumped isotope data.

Lumsden, D.N., 1979. Discrepancy between thin-section and X-ray estimates of dolomite in limestone. Journal of Sedimentary Research, 49(2).

Machel, H.G., 1997. Recrystallization versus neomorphism, and the concept of ‘significant recrystallization’in dolomite research. Sedimentary Geology, 113(3): 161-168.

Machel, H.G., 2004. Concepts and models of dolomitization: a critical reappraisal. Geological Society, London, Special Publications, 235(1): 7-63.

Machel, H.G. and Burton, E.A., 1991. Factors governing cathodoluminescence in calcite and dolomite, and their implications for studies of carbonate diagenesis. In: C.E. Barker and O.C. Kopp (Editors), Luminescence Microscopy: Quantitative and Qualitative Aspects. SEPM, Tulsa, pp. 37-58.

Malone, M.J., Baker, P.A. and Burns, S.J., 1994. Recrystallization of dolomite: evidence from the Monterey Formation (Miocene), California. Sedimentology, 41(6): 1223-1239.

Martinez, I., Zhang, J. and Reeder, R.J., 1996. In situ X-ray diffraction of aragonite and dolomite at high pressure and high temperature: Evidence for dolomite breakdown to aragonite and magnesite. American Mineralogist, 81(5-6): 611-624.

Meckler, A.N., Ziegler, M., Millán, M.I., Breitenbach, S.F. and Bernasconi, S.M., 2014. Long-term performance of the Kiel carbonate device with a new correction scheme for clumped isotope measurements. Rapid Communications in Mass Spectrometry, 28(15): 1705-1715.

Morse, J.W. and Casey, W.H., 1988. Ostwald processes and mineral paragenesis in sediments. American Journal of Science, 288(6): 537-560.

Navrotsky, A. and Capobianco, C., 1987. Enthalpies of formation of dolomite and of magnesian calcites. American Mineralogist, 72(7-8): 782-787.

Reeder, R. and Wenk, H.-R., 1983. Structure refinements of some thermally disordered dolomites. American Mineralogist, 68(7-8): 769-776.

Reeder, R.J., 1983. Crystal chemistry of the rhombohedral carbonates. Reviews in Mineralogy and Geochemistry, 11(1): 1-47.

Reeder, R.J., 1992. Carbonates; growth and alteration microstructures. Reviews in Mineralogy and Geochemistry, 27(1): 380-424.

Reeder, R.J., 2000. Constraints on cation order in calcium-rich sedimentary dolomite. Aquatic Geochemistry, 6(2): 213-226.

Reeder, R.J. and Sheppard, C.E., 1984. Variation of lattice parameters in some sedimentary dolomites. American Mineralogist, 69(5-6): 520-527.

Scheffzük, C., Siegesmund, S. and Koch, A., 2004. Strain investigations on calcite marbles using neutron time-of-flight diffraction. Environmental Geology, 46(3): 468-476.

Toby, B.H., 2012. R factors in Rietveld analysis: How good is good enough? Powder Diffraction, 21(1): 67-70.

Toby, B.H. and Von Dreele, R.B., 2013. GSAS-II: the genesis of a modern open-source all purpose crystallography software package. Journal of Applied Crystallography, 46(2): 544-549.

Turpin, M., Nader, F. and Kohler, E., 2012. Empirical calibration for dolomite stoichiometry calculation: application on Triassic Muschelkalk-Lettenkohle carbonates (French Jura). OGST-Revue d'IFP Energies nouvelles, 67(1): 77-95.

Veizer, J., 1983. Chemical diagenesis of carbonates: theory and application of trace element technique, Stable Isotopes in Sedimentary Geology. Short Course Notes. SEPM, pp. 1-100.

Wenk, H.-R., Barber, D.J. and Reeder, R.J., 1983. Microstructures in carbonates. Reviews in Mineralogy and Geochemistry, 11(1): 301-367.

Wenk, H.-R., Meisheng, H., Lindsey, T. and Morris, J.W., 1991. Superstructures in ankerite and calcite. Physics and Chemistry of Minerals, 17(6): 527-539.

Wyckoff, R.W.G. and Merwin, H.E., 1924. The crystal structure of dolomite. American Journal of Science(48): 447-461.

Zucchini, A., Comodi, P., Nazzareni, S. and Hanfland, M., 2014. The effect of cation ordering and temperature on the high-pressure behaviour of dolomite. Physics and Chemistry of Minerals, 41(10): 783-793.

Table

Table 1: List of results obtained from the Rietveld refinements, elemental analysis, crystal size measurements and calculated clumped isotope temperatures. Top samples analyzed by synchrotron X-ray and neutron diffraction, bottom samples analyzed by conventional XRD. *Stoichiometry calculated using the method of Turpin et al. (2012) based on the a and c unit cell parameters, respectively. † Results of elemental analysis. ‡ Determined optically from thin sections.

Sample	**Location**	**wR**	**a (Å)**	**a (Å) esd**	**c (Å)**	**c (Å) esd**	**volume (Å^3)**	**volume (Å^3) esd**	**CaCO$_3$ mol% (a)***	**CaCO$_3$ mol% (c)***	**CaCO$_3$ mol%†**	**Ca/Mg mol†**	**Fe (ppm)†**	**Mn (ppm)†**	**Sr (ppm)†**	**Mean crystal size (μm)‡**	**Mean clumped temperature (°C)**
H1 (HH26)	HR	18.38	4.81138	3.1E-05	16.031435	0.000072	321.397	0.002	51.80	51.52	51.63	1.07	942.57	33.32	65.96	17	87
HH2/1	HR	17.72	4.80949	2.4E-05	16.015938	0.000056	320.834	0.002	51.27	50.76	49.69	0.99	233.92	97.71	32.24	431	91
HHUB18 (HH4)	HR	16.15	4.8087	0.00002	16.011535	0.000048	320.642	0.001	51.05	50.55	51.61	1.07	998.25	53.26	53.05	309	115
MGY-1 381.5 m	MGY-1	19.32	4.81447	5.1E-05	16.046993	0.000122	322.122	0.004	52.67	52.28	53.39	1.15	255.93	22.25	82.21	51	64
VA-7 (VA 3T/1)	VA	18.43	4.8097	2.6E-05	16.017537	0.000061	320.894	0.002	51.33	50.84	51.75	1.06	790.52	85.21	72.32	394	132
ZB-4	ZB	20.44	4.8104	3.2E-05	16.021761	0.000074	321.073	0.002	51.53	51.05	51.29	1.05	364.68	22.46	73.68	24	51

Sample	**Location**	**wR**	**a (Å)**	**a (Å) esd**	**c (Å)**	**c (Å) esd**	**volume (Å^3)**	**volume (Å^3) esd**	**CaCO$_3$ mol% (a)***	**CaCO$_3$ mol% (c)***	**CaCO$_3$ mol%†**	**Ca/Mg mol†**	**Fe (ppm)†**	**Mn (ppm)†**	**Sr (ppm)†**	**Mean crystal size (μm)‡**	**Mean clumped temperature (°C)**
GF-1 918.2 m	GF-1	13.11	4.819180	0.000463	16.101990	0.001009	323.859	0.047	53.98	54.98	55.32	1.24	1340.40	49.92	98.96	76	
GF-1 998 m	GF-1	12.44	4.808380	0.000147	16.013480	0.000391	320.637	0.016	50.96	50.64	50.33	1.01	945.53	26.66	100.15	14	
GF-1 1055 m	GF-1	10.36	4.808540	0.000124	16.012990	0.000309	320.649	0.013	51.01	50.62	50.80	1.03	1440.66	32.67	71.52	17	67
GF-1 1109 m	GF-1	13.46	4.810620	0.000257	16.029660	0.000628	321.261	0.027	51.59	51.43	51.74	1.07	1818.30	50.01	96.17	13	
HH4	HR	4.58	4.809797	0.000500	16.020141	0.001450	320.960	0.056	51.36	50.97	51.61	1.07	998.25	53.26	53.05	210	
HH26	HR	10.77	4.809350	0.000150	16.020050	0.000373	320.899	0.016	51.23	50.96	51.63	1.07	942.57	33.32	65.96	17	67
MGY-1 253.8 m	MGY-1	12.99	4.809040	0.000132	16.020050	0.000348	320.857	0.014	51.15	50.96	50.72	1.03	496.01	15.24	94.35	22	
MGY-1 333.5 m	MGY-1	13.74	4.817007	0.000373	16.083414	0.000795	323.194	0.036	53.38	54.07	54.31	1.19	671.16	35.41	113.55	99	47
MGY-1 346.9 m	MGY-1	11.8	4.810480	0.000238	16.029480	0.000547	321.238	0.024	51.55	51.42	51.78	1.07	523.77	34.14	79.66	16	44
MGY-1 366.5 m	MGY-1	12.11	4.811510	0.000216	16.038970	0.000496	321.566	0.022	51.84	51.89	52.84	1.12	362.80	40.70	69.15	37	
MGY-1 381.5 m	MGY-1	18.8	4.812250	0.000339	16.040030	0.000905	321.686	0.037	52.05	51.94	53.39	1.15	255.93	22.25	82.21	51	64
VA 3T/1	VA	12.36	4.809710	0.000186	16.022450	0.000426	320.994	0.018	51.33	51.08	51.75	1.06	790.52	85.21	72.32	186	
ZB-4	ZB	11.96	4.809450	0.000193	16.021840	0.000454	320.948	0.020	51.26	51.05	51.29	1.05	364.68	22.46	73.68	24	51
ZB-6	ZB	12.29	4.808920	0.000189	16.016830	0.000450	320.776	0.019	51.11	50.80	50.68	1.03	236.65	21.09	65.92	26	

Figures

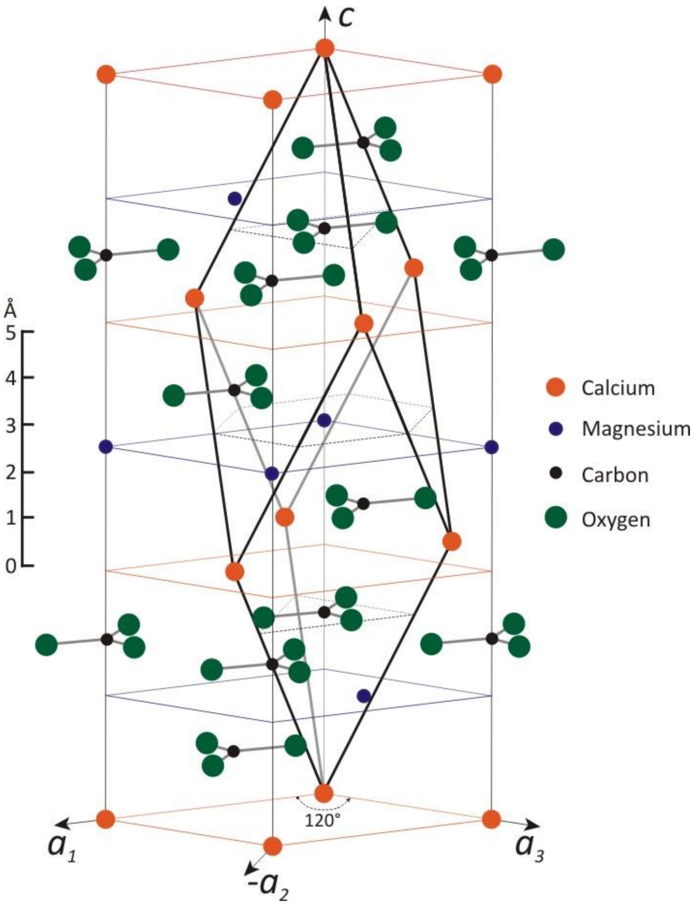

Fig. 1: The hexagonal unit cell superimposed onto the rhombohedral unit cell of dolomite (Gregg et al., 2015)

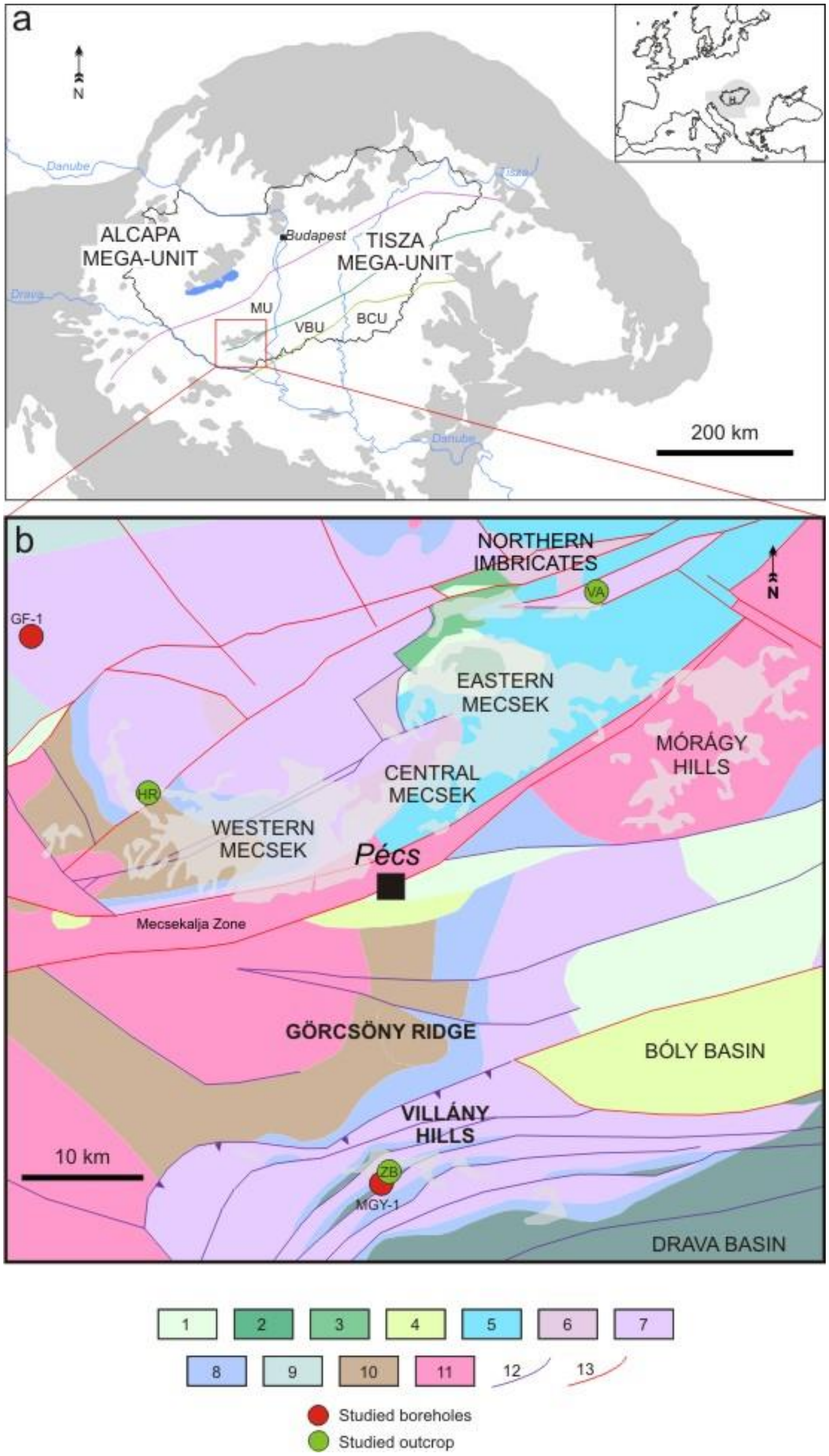

Fig. 2: Location of the study area. **(a)** The study area is situated in SW Hungary as indicated by the red rectangle. The purple line represents the Mid-Hungarian Fault Zone. The green lines mark

the boundaries between the subunits of the Tisza Mega-Unit. MU: Mecsek Unit, VBU: Villány-Bihor Unit, BCU: Békés-Codru Unit (modified after Csontos et al., 1992). Gray shading indicates outcrops of Pre-Neogene formations. The inset map shows the location of the Pannonian Basin and Hungary within Europe. **(b)** Simplified geological map of the study area showing the sampling locations (Cenozoic cover not shown). Shaded areas indicate outcrops of Pre-Cenozoic formations (modified after Haas, 2012). Purple triangles indicate the Mesozoic overthrust zone that separates the Villány Hills from the Görcsöny Ridge. Sampling locations: GF-1: Gálosfa-1, HR: Hetvehely roadcut, MGY-1: Máriagyűd-1, ZB: VA: Váralja quarry, Zuhánya quarry. Legend: 1: Upper Cretaceous continental and marine formations, 2: Lower Cretaceous platform limestones, 3: Lower Cretaceous volcanic rocks, 4: Middle Jurassic to Lower Cretaceous pelagic limestones, 5: Lower and Middle Jurassic siliciclastic formations, 6: Upper Triassic to Lower Jurassic coal-bearing siliciclastic formations, 7: Middle Triassic shallow marine siliciclastic and carbonate formations, 8: Lower Triassic siliciclastic formations, 9: Mesozoic rocks in general, 10: Permian and Upper Carboniferous continental siliciclastic formations, 11: Paleozoic crystalline rocks, 12: Mesozoic fault lines, 13: Cenozoic fault lines.

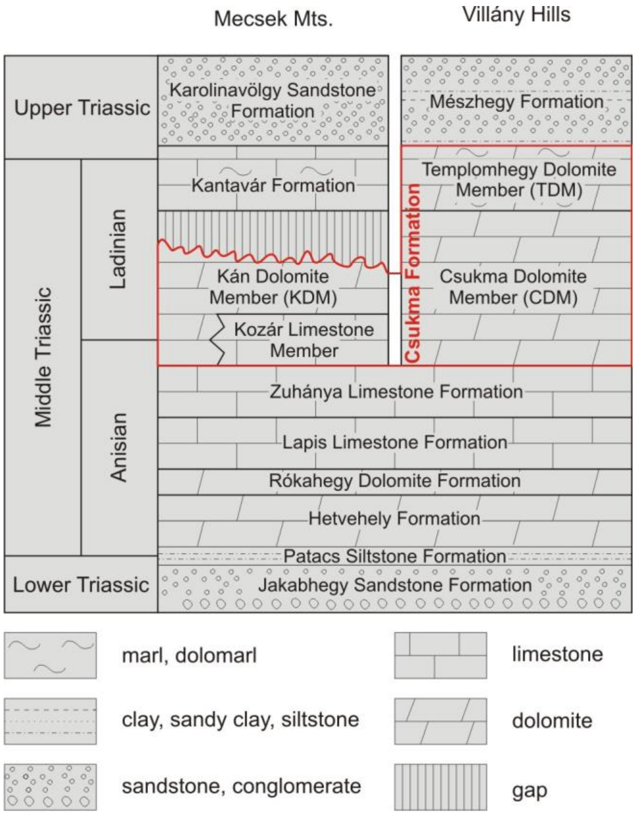

Fig. 3: Schematic stratigraphic column of the Triassic succession of the Villány Hills and the Mecsek Mts. Members of the Csukma Formation are highlighted by red frame.

DESCRIPTION	SAMPLES
Reflux dolomites recrystallized in intermediate burial setting (Csukma Formation, Western Mecsek Mts.)	GF-1 918.2 m GF-1 998 m GF-1 1055 m GF-1 1109 m HH-26 H1
Fault-controlled, doubly recrystallized reflux dolomites (Csukma Formation, Western Mecsek Mts.)	HH-4 HHUB-18
Fault-controlled, hydrothermal dolomites (Csukma Formation, Eastern Mecsek Mts.)	VA-7 VA-3T/1
Fault-controlled, burial dolomites (Zuhánya Limestone Formation, Western Mecsek Mts.)	HH-2/1
Seawater dolomites recrystallized in intermediate burial setting (Csukma Formation, Villány Hills)	MGY-1 253.8 m MGY-1 333.5 m MGY-1 346.9 m MGY-1 366.5 m MGY-1 381.5 m ZB-4 ZB-6

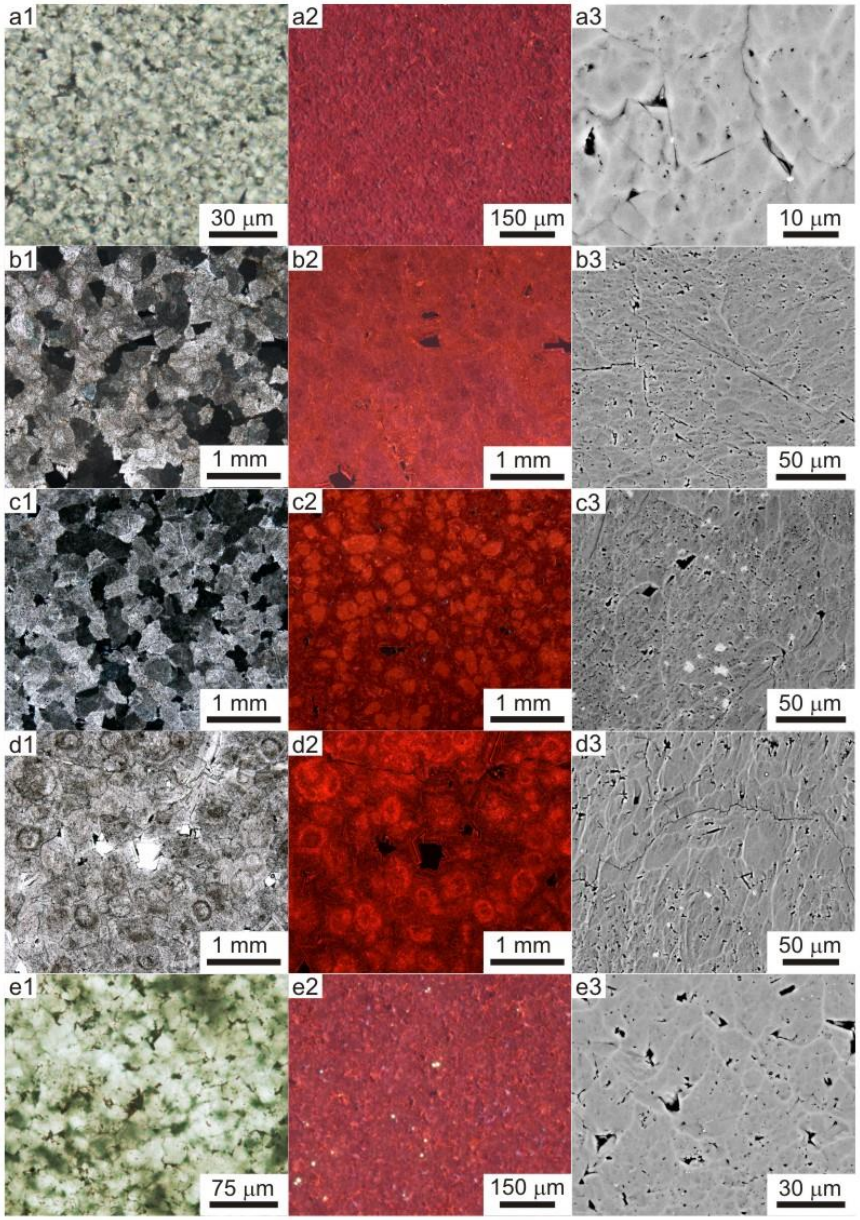

Fig. 4

Fig. 4: Description and characteristics of the studied samples according to dolomite types. **(a1)** Fine crystalline, planar-s, subordinately planar-e dolomite. Plane-polarized light. **(a2)** CL image of a fine crystalline, planar-s dolomite. **(a3)** BSE image of a fine crystalline planar-e to planar-s dolomite. **(b1)** Coarse crystalline, planar-s to nonplanar-a dolomite. Cross-polarized light. **(b2)** Same as in b1 in CL. **(b3)** BSE image of a coarse crystalline, planar-s to nonplanar-a dolomite. **(c1)** Coarse crystalline, planar-s to nonplanar-a dolomite. Cross-polarized light. **(c2)** Same as in c1 in CL. **(c3)** BSE image of a coarse crystalline, planar-s to nonplanar-a dolomite. Lighter spots are calcite inclusions. **(d1)** Coarse crystalline, planar-s, subordinately planar-e dolomite. Plane-polarized light. **(d2)** Same as in d1 in CL. **(d3)** BSE image of a coarse crystalline, planar-s dolomite. Lighter spots are calcite inclusions. **(e1)** Fine crystalline, planar-s, subordinately planar-e dolomite. Plane-polarized light. **(e2)** CL image of a fine crystalline, planar-s dolomite. **(e3)** BSE image of a fine crystalline planar-e to planar-s dolomite.

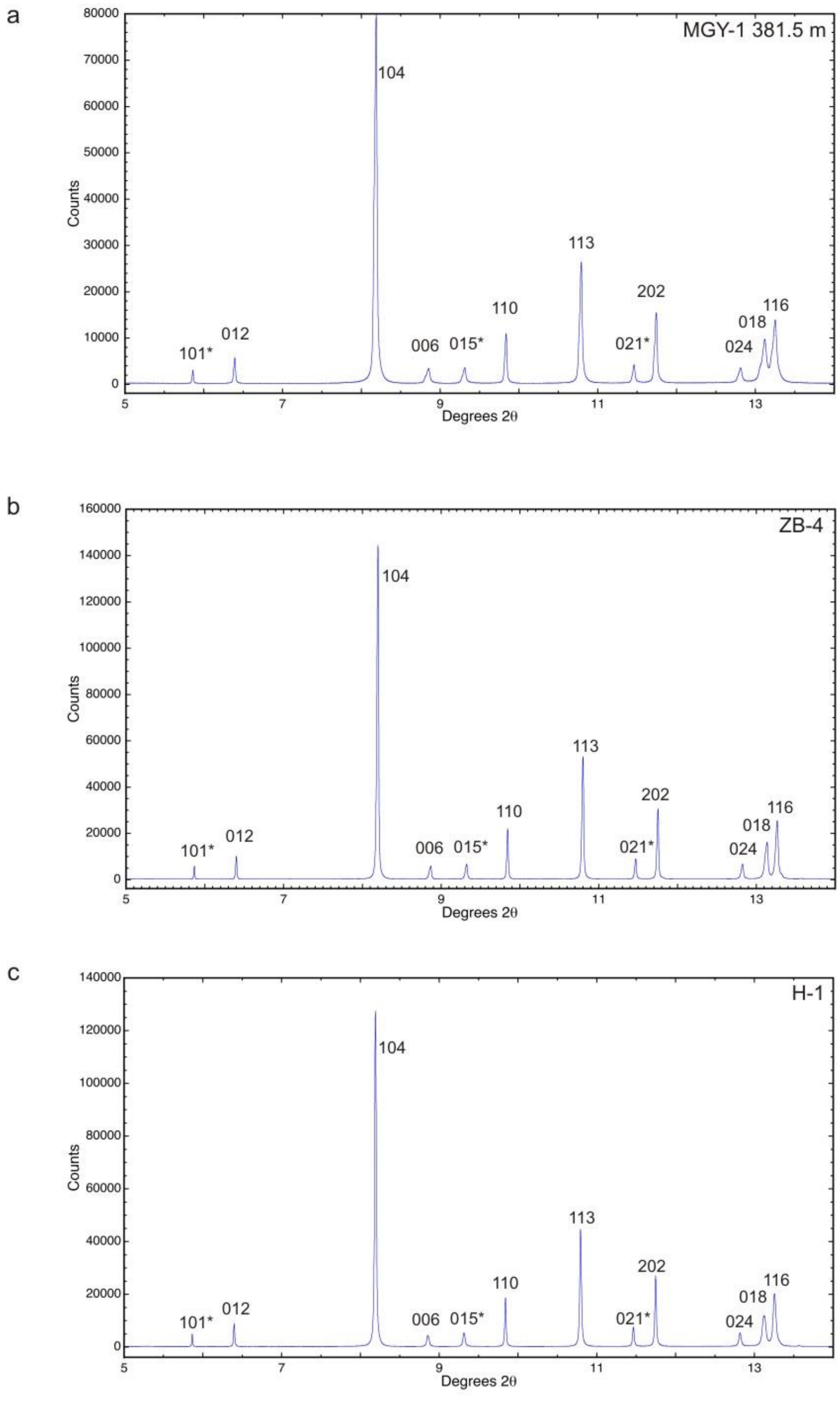

Fig. 5: Synchrotron X-ray diffractograms of the analyzed samples shown between 5 and 15° 2θ. Numbers indicate the Miller indices of the reflections. Asterisk indicates ordering reflections.

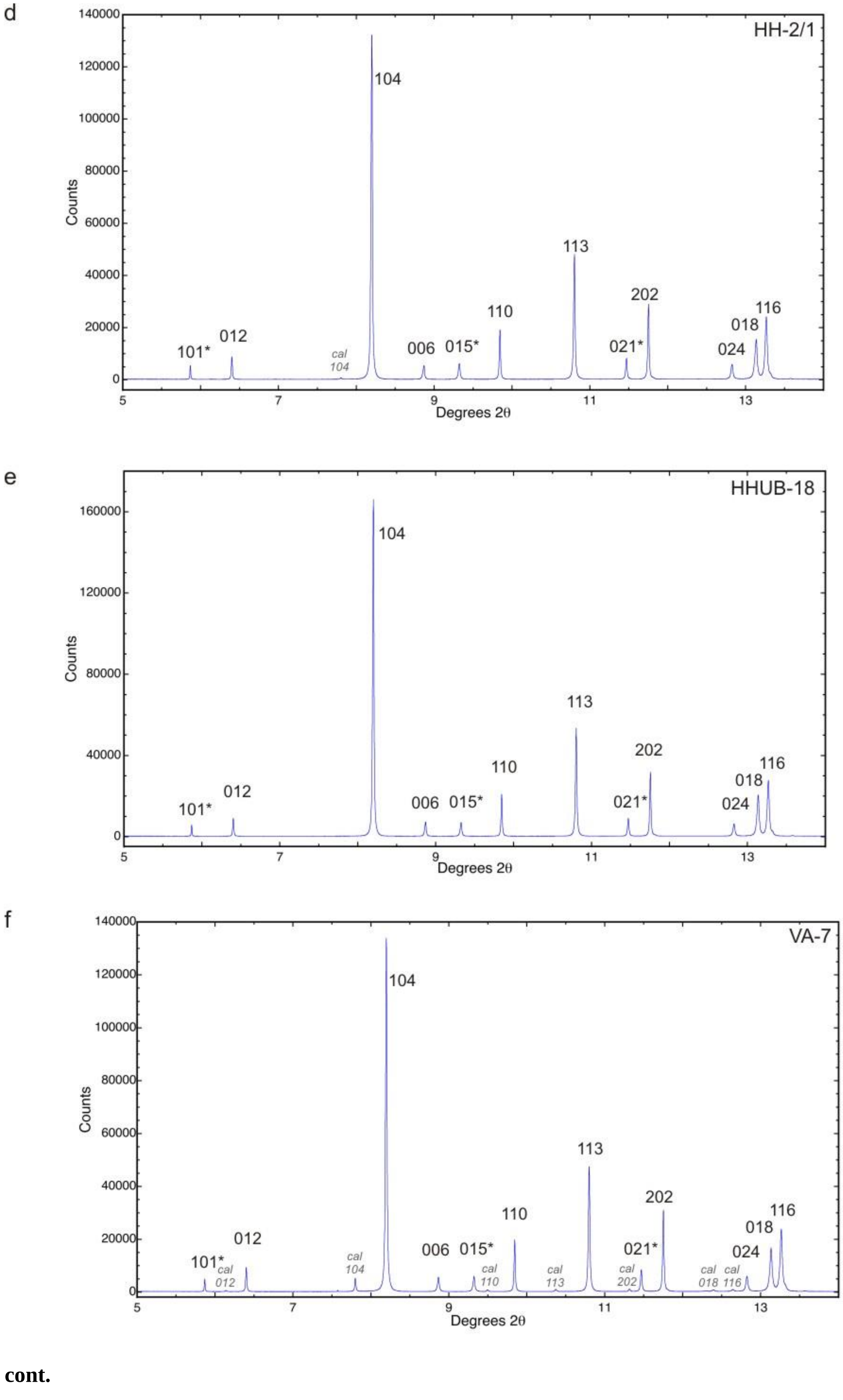
d
HH-2/1
140000
120000
100000
80000
60000
40000
20000
0
Counts
104
113
202
110
116
018
012
101*
cal 104
006
015*
021*
024
5
7
9
11
13
Degrees 2θ
e
HHUB-18
160000
120000
80000
40000
0
Counts
104
113
202
110
116
018
012
101*
006
015*
021*
024
5
7
9
11
13
Degrees 2θ
f
VA-7
140000
120000
100000
80000
60000
40000
20000
0
Counts
104
113
202
110
116
018
012
101*
cal 012
cal 104
006
015*
cal 110
cal 113
021*
cal 202
024
cal 018
cal 116
5
7
9
11
13
Degrees 2θ

Fig. 5 cont.

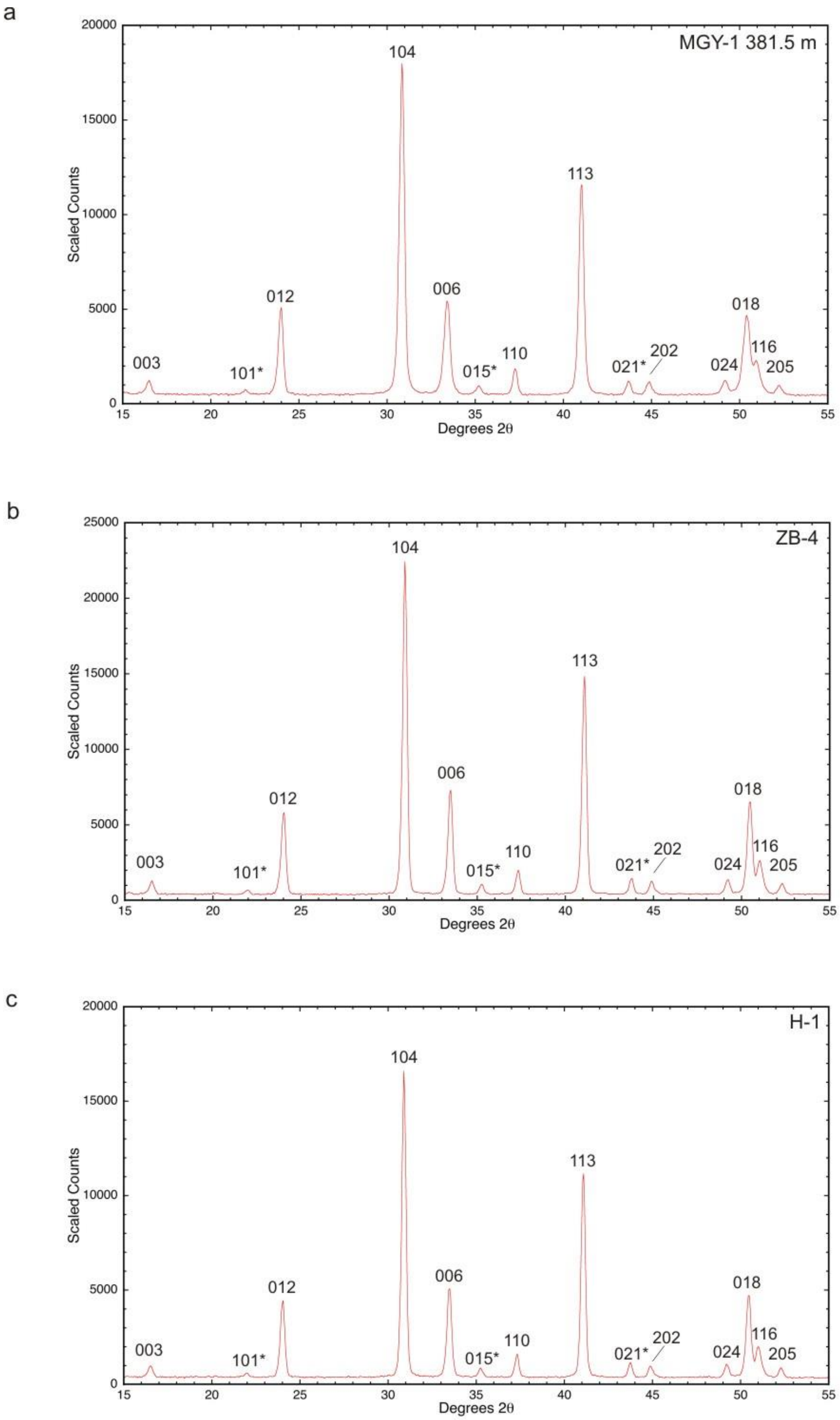

Fig. 6: Neutron diffractograms of the analyzed samples shown between 15 and 55° 2θ. Numbers indicate the Miller indices of the reflections. Asterisk indicates ordering reflections.

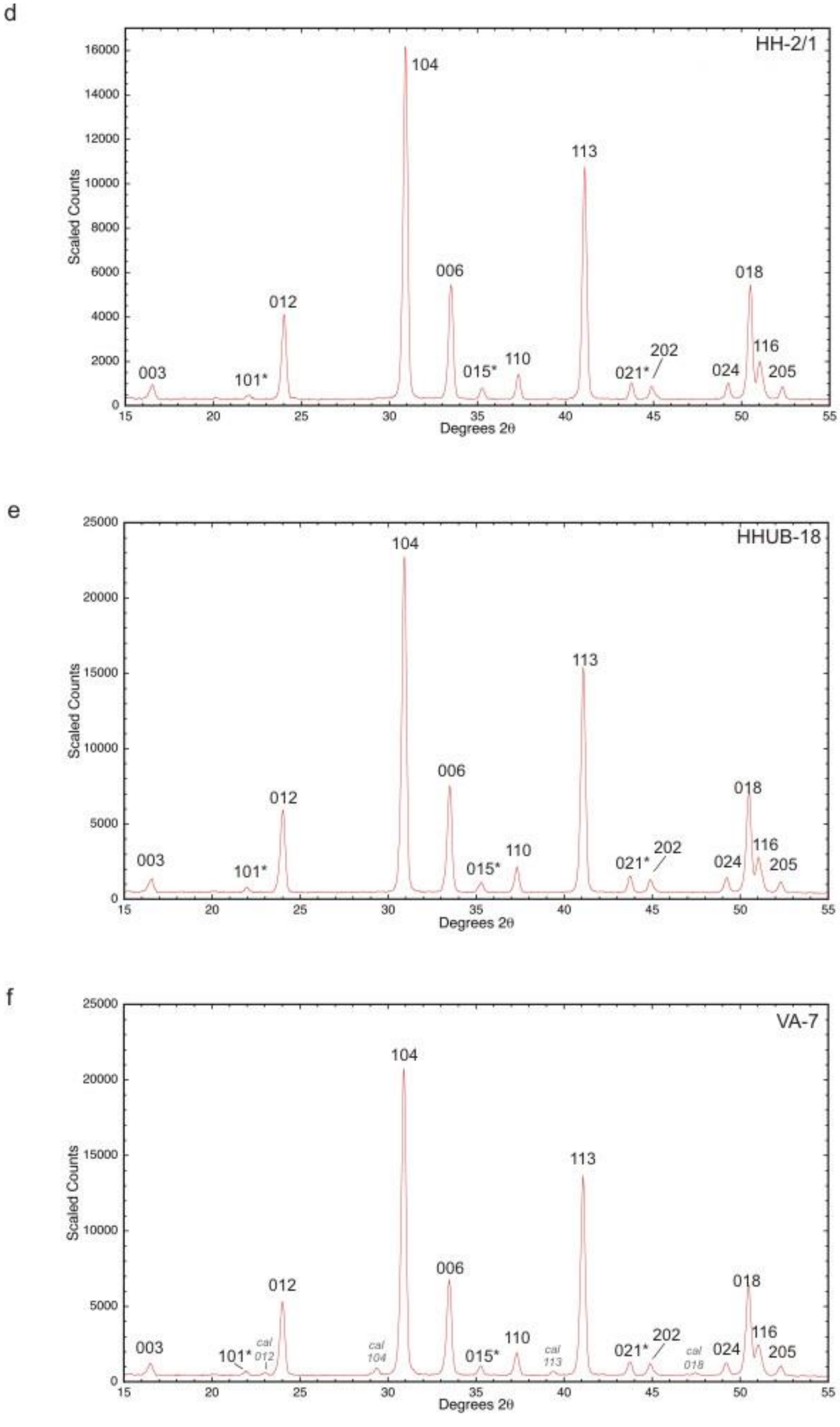
d
HH-2/1
Scaled Counts
0
2000
4000
6000
8000
10000
12000
14000
16000
15
20
25
30
35
40
45
50
55
Degrees 2θ
003
101*
012
104
006
015*
110
113
021*
202
024
018
116
205
e
HHUB-18
Scaled Counts
0
5000
10000
15000
20000
25000
15
20
25
30
35
40
45
50
55
Degrees 2θ
003
101*
012
104
006
015*
110
113
021*
202
024
018
116
205
f
VA-7
Scaled Counts
0
5000
10000
15000
20000
25000
15
20
25
30
35
40
45
50
55
Degrees 2θ
003
101*
cal 012
012
cal 104
104
006
015*
110
cal 113
113
021*
202
cal 018
024
018
116
205

Fig. 6 cont.

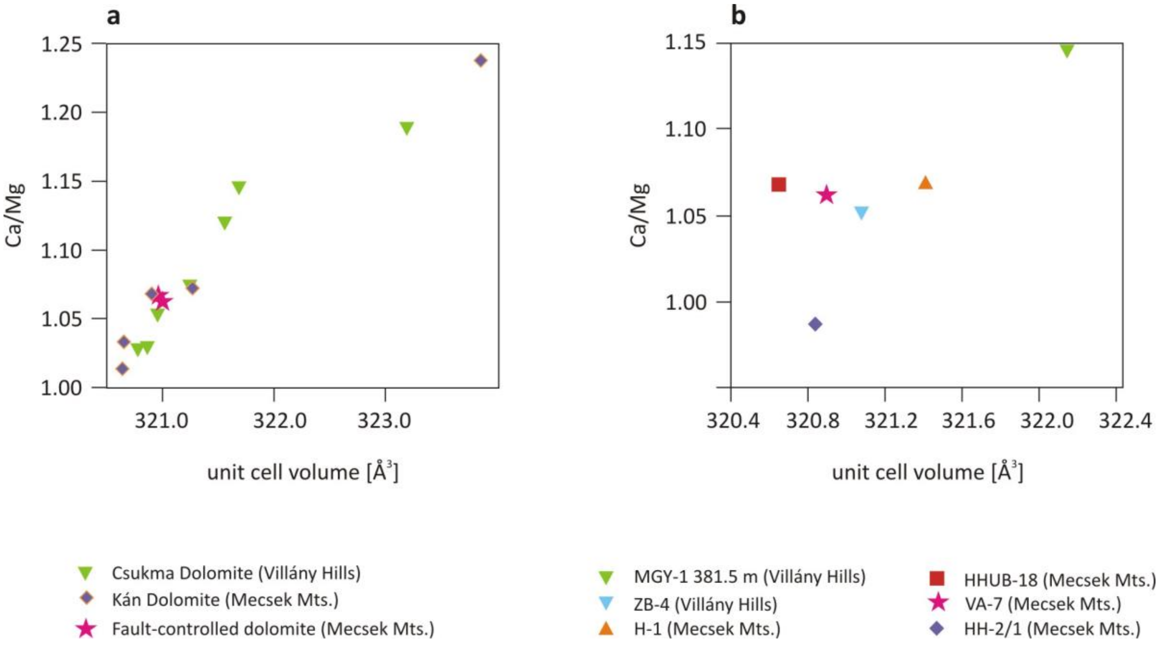

Fig. 7: Plots of Ca/Mg molar ratio vs. unit cell volume. Ca/Mg calculated from elemental composition **(a)** Unit cell volume obtained from Rietveld refinement of the conventional X-ray data. **(b)** Unit cell volume obtained from the joint Rietveld refinement of the synchrotron X-ray and neutron diffraction datasets.

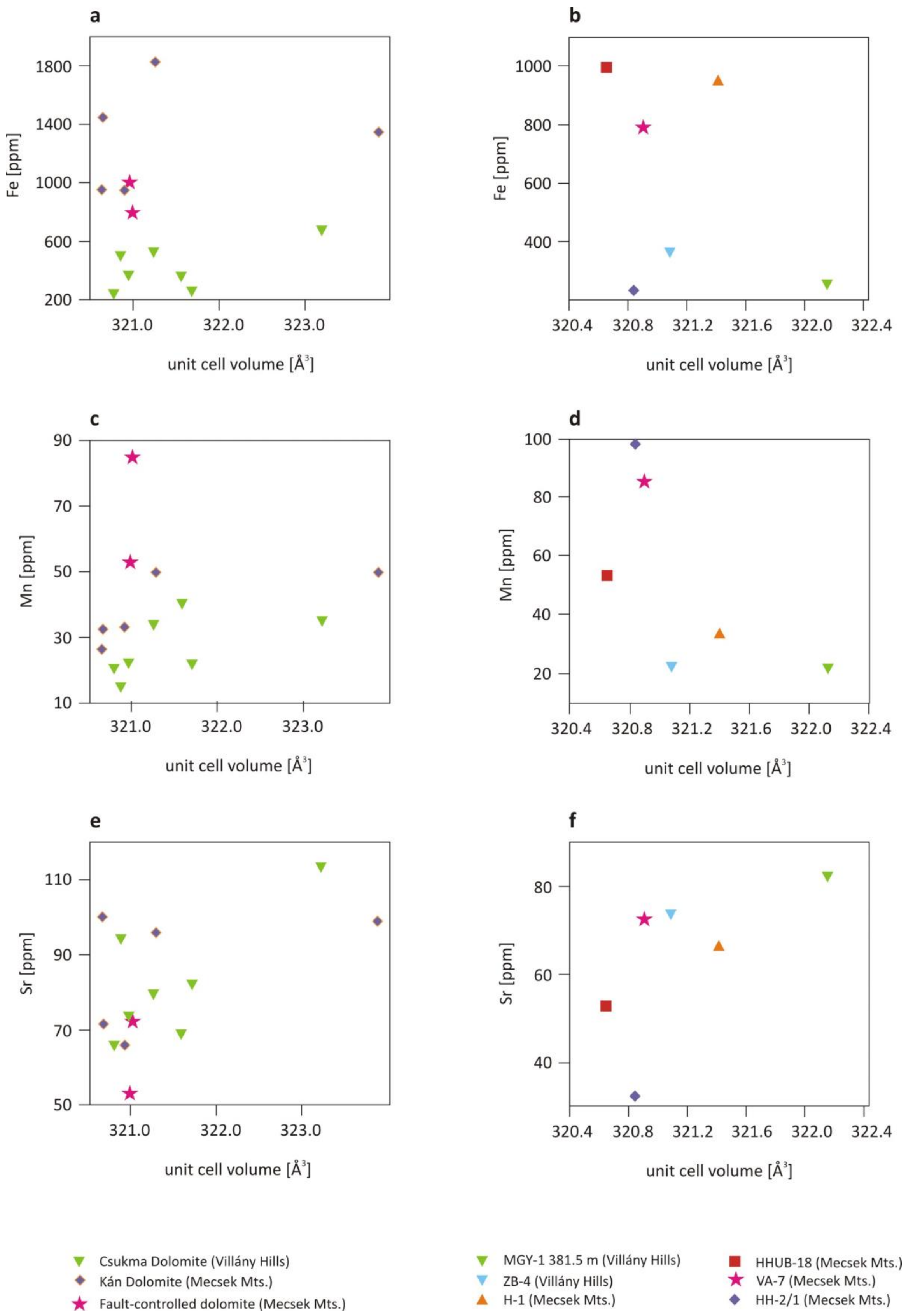
a
Fe [ppm]
1800
1400
1000
600
200
321.0
322.0
323.0
unit cell volume [Å³]
b
Fe [ppm]
1000
800
600
400
320.4
320.8
321.2
321.6
322.0
322.4
unit cell volume [Å³]
c
Mn [ppm]
90
70
50
30
10
321.0
322.0
323.0
unit cell volume [Å³]
d
Mn [ppm]
100
80
60
40
20
320.4
320.8
321.2
321.6
322.0
322.4
unit cell volume [Å³]
e
Sr [ppm]
110
90
70
50
321.0
322.0
323.0
unit cell volume [Å³]
f
Sr [ppm]
80
60
40
320.4
320.8
321.2
321.6
322.0
322.4
unit cell volume [Å³]
Csukma Dolomite (Villány Hills)
Kán Dolomite (Mecsek Mts.)
Fault-controlled dolomite (Mecsek Mts.)
MGY-1 381.5 m (Villány Hills)
ZB-4 (Villány Hills)
H-1 (Mecsek Mts.)
HHUB-18 (Mecsek Mts.)
VA-7 (Mecsek Mts.)
HH-2/1 (Mecsek Mts.)

Fig. 8: Plots of minor/trace element content vs. unit cell volume. **(a)** Fe content vs. unit cell volume obtained from Rietveld refinement of the conventional X-ray data. **(b)** Fe content vs. unit cell volume obtained from the joint Rietveld refinement of the synchrotron X-ray and neutron diffraction datasets. **(c)** Mn content vs. unit cell volume obtained from Rietveld refinement of the conventional X-ray data. **(d)** Mn content vs. unit cell volume obtained from the joint Rietveld refinement of the synchrotron X-ray and neutron diffraction datasets. **(e)** Sr content vs. unit cell volume obtained from Rietveld refinement of the conventional X-ray data. **(f)** Sr content vs. unit cell volume obtained from the joint Rietveld refinement of the synchrotron X-ray and neutron diffraction datasets.

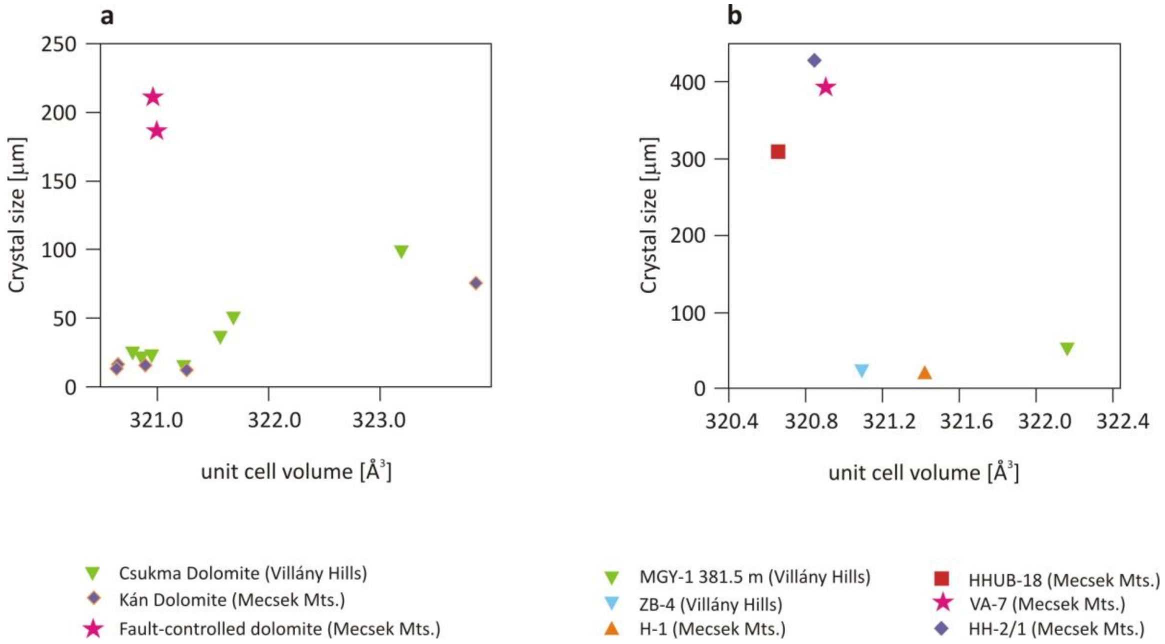

Fig. 9: Plots of crystal size vs. unit cell volume. Crystal size determined optically from thin sections. **(a)** Unit cell volume obtained from Rietveld refinement of the conventional X-ray data. **(b)** Unit cell volume obtained from the joint Rietveld refinement of the synchrotron X-ray and neutron diffraction datasets.

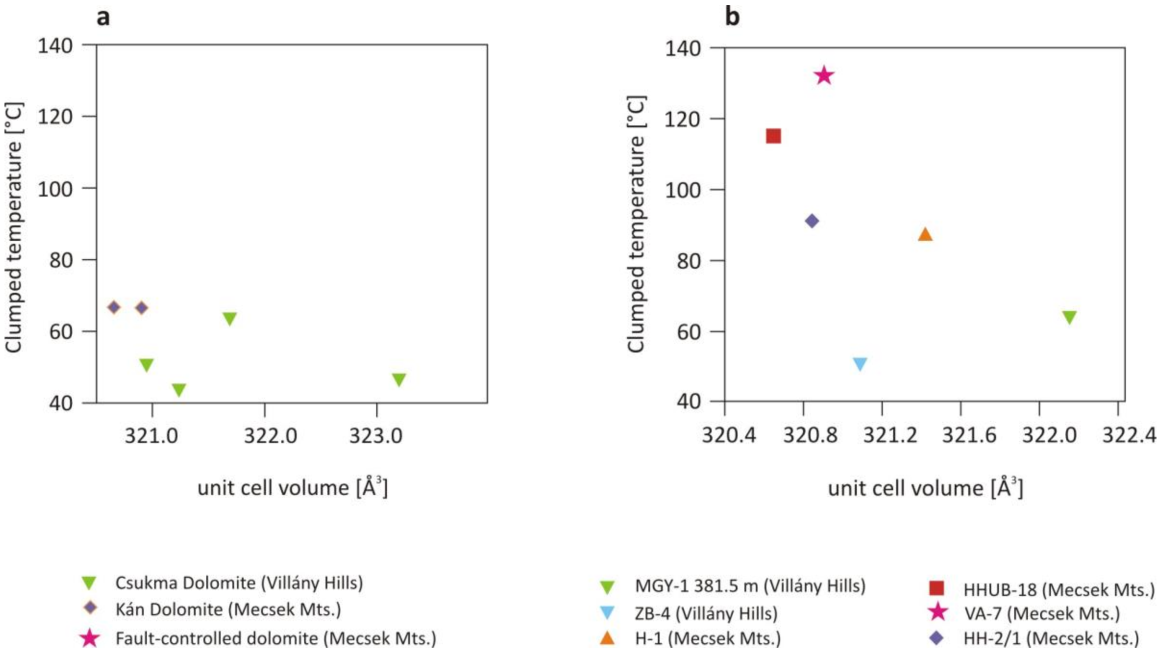

Fig. 10: Plots of clumped isotope temperatures vs. unit cell volume. **(a)** Unit cell volume obtained from Rietveld refinement of the conventional X-ray data. **(b)** Unit cell volume obtained from the joint Rietveld refinement of the synchrotron X-ray and neutron diffraction datasets.

CHAPTER IV

CONCLUSIONS

Integration of petrographic, conventional stable oxygen and carbon isotope, clumped isotope, and strontium isotope data with the paleogeography, paleoclimate, and burial history of the Triassic Csukma Formation in the Mecsek Mts. and Villány Hills of SW Hungary revealed the complex diagenetic history of these peritidal carbonates. The results of this study imply that the clumped isotope method integrated with other geochemical data can successfully be applied to identify the nature and potential sources of extra-formational diagenetic fluids responsible for dolomitization and recrystallization. This study provides conclusive evidence for multi-phase dolomitization and dolomite recrystallization over several millions of years and several thousands of meters of burial. Furthermore, this study is the first to identify fault-controlled dolomitization by circulating Cretaceous seawater within Triassic carbonates of central Europe, further supporting the viability of the interpretation of dolomitization by seawater initially drawn down and then geothermally circulated through faults in extensional basins. Results of this study suggest that the clumped isotope temperatures of partially recrystallized dolomites, via dissolution–re-precipitation, may provide a minimum estimate of the temperature of recrystallization. Furthermore, the results show that recrystallization processes with low water to rock ratio may result in a noticeable trend between crystal size and unit cell parameters that cannot be explained by Ostwald-ripening. In samples recrystallized with high water to rock ratios compositionally indistinguishable overgrowth cement on the matrix dolomite may have a significant effect on the overall unit cell dimensions determined from powder diffraction analyses.

APPENDICES

Appendix 1 – Crystallographic Information Files

A1.1. Rietveld refinement results of conventional X-ray diffraction data

```
##########################################################################
#GF-1 918.2 m

data_dolomite

# phase info for dolomite follows
_pd_phase_name  dolomite
_cell_length_a  4.819175
_cell_length_b  4.819175
_cell_length_c  16.101992
_cell_angle_alpha  90
_cell_angle_beta   90
_cell_angle_gamma  120
_cell_volume  323.859
_exptl_crystal_density_diffrn  2.8368
_symmetry_cell_setting  trigonal
_symmetry_space_group_name_H-M  "R -3"
loop_
    _space_group_symop_id
    _space_group_symop_operation_xyz
     1  x,y,z
     2  -y,x-y,z
     3  y-x,-x,z
     4  -x,-y,-z
     5  y,y-x,-z
     6  x-y,x,-z
     7  2/3+x,1/3+y,1/3+z
     8  2/3-y,1/3+x-y,1/3+z
     9  2/3+y-x,1/3-x,1/3+z
    10  2/3-x,1/3-y,1/3-z
    11  2/3+y,1/3+y-x,1/3-z
    12  2/3+x-y,1/3+x,1/3-z
    13  1/3+x,2/3+y,2/3+z
    14  1/3-y,2/3+x-y,2/3+z
    15  1/3+y-x,2/3-x,2/3+z
    16  1/3-x,2/3-y,2/3-z
    17  1/3+y,2/3+y-x,2/3-z
    18  1/3+x-y,2/3+x,2/3-z

# ATOMIC COORDINATES AND DISPLACEMENT PARAMETERS
loop_
   _atom_site_label
```

```
   _atom_site_type_symbol
   _atom_site_fract_x
   _atom_site_fract_y
   _atom_site_fract_z
   _atom_site_occupancy
   _atom_site_adp_type
   _atom_site_U_iso_or_equiv
   _atom_site_symmetry_multiplicity
Ca1    Ca2+ 0.00000     0.00000     0.00000     0.998900   Uiso 0.010      3
Mg1    Mg2+ 0.00000     0.00000     0.00000     0.00110000 Uiso 0.010      3
Ca2    Ca2+ 0.00000     0.00000     0.50000     0.00250000 Uiso 0.010      3
Mg2    Mg2+ 0.00000     0.00000     0.50000     0.997500   Uiso 0.010      3
C1     C    0.00000     0.00000     0.24266     1.000      Uiso 0.005      6
O1     O2-  0.24762     -0.03535    0.24406     1.000      Uiso 0.015      18

loop_  _atom_type_symbol _atom_type_number_in_cell
  C    6
  Ca   3.004
  Mg   2.996
  O    18

# Note that Z affects _cell_formula_sum and _weight
_cell_formula_units_Z  6
_chemical_formula_sum  "C Ca0.501 Mg0.499 O3"
_chemical_formula_weight  92.21
```

```
##############################################################################
#GF-1 998 m

data_dolomite

# phase info for dolomite follows
_pd_phase_name  dolomite
_cell_length_a  4.808379
_cell_length_b  4.808379
_cell_length_c  16.013484
_cell_angle_alpha  90
_cell_angle_beta   90
_cell_angle_gamma  120
_cell_volume  320.637
_exptl_crystal_density_diffrn  2.8545
_symmetry_cell_setting  trigonal
_symmetry_space_group_name_H-M  "R -3"
loop_
    _space_group_symop_id
    _space_group_symop_operation_xyz
     1  x,y,z
     2  -y,x-y,z
     3  y-x,-x,z
     4  -x,-y,-z
     5  y,y-x,-z
     6  x-y,x,-z
     7  2/3+x,1/3+y,1/3+z
     8  2/3-y,1/3+x-y,1/3+z
     9  2/3+y-x,1/3-x,1/3+z
    10  2/3-x,1/3-y,1/3-z
    11  2/3+y,1/3+y-x,1/3-z
    12  2/3+x-y,1/3+x,1/3-z
    13  1/3+x,2/3+y,2/3+z
    14  1/3-y,2/3+x-y,2/3+z
    15  1/3+y-x,2/3-x,2/3+z
    16  1/3-x,2/3-y,2/3-z
    17  1/3+y,2/3+y-x,2/3-z
    18  1/3+x-y,2/3+x,2/3-z

# ATOMIC COORDINATES AND DISPLACEMENT PARAMETERS
loop_
   _atom_site_label
   _atom_site_type_symbol
   _atom_site_fract_x
   _atom_site_fract_y
   _atom_site_fract_z
```

```
   _atom_site_occupancy
   _atom_site_adp_type
   _atom_site_U_iso_or_equiv
   _atom_site_symmetry_multiplicity
Ca1    Ca2+ 0.00000     0.00000     0.00000     0.923      Uiso 0.010      3
Mg1    Mg2+ 0.00000     0.00000     0.00000     0.077      Uiso 0.010      3
Ca2    Ca2+ 0.00000     0.00000     0.50000     0.034      Uiso 0.010      3
Mg2    Mg2+ 0.00000     0.00000     0.50000     0.966      Uiso 0.010      3
C1     C    0.00000     0.00000     0.24266     1.000      Uiso 0.005      6
O1     O2-  0.24762     -0.03535    0.24406     1.000      Uiso 0.015      18

loop_  _atom_type_symbol _atom_type_number_in_cell
  C    6
  Ca   2.872
  Mg   3.128
  O    18

# Note that Z affects _cell_formula_sum and _weight
_cell_formula_units_Z  6
_chemical_formula_sum  "C Ca0.479 Mg0.521 O3"
_chemical_formula_weight  91.86
```

```
################################################################################
#GF-1 1055 m

data_dolomite

# phase info for dolomite follows
_pd_phase_name  dolomite
_cell_length_a  4.808544
_cell_length_b  4.808544
_cell_length_c  16.012989
_cell_angle_alpha  90
_cell_angle_beta   90
_cell_angle_gamma  120
_cell_volume  320.649
_exptl_crystal_density_diffrn  2.8653
_symmetry_cell_setting  trigonal
_symmetry_space_group_name_H-M  "R -3"
loop_
    _space_group_symop_id
    _space_group_symop_operation_xyz
     1  x,y,z
     2  -y,x-y,z
     3  y-x,-x,z
     4  -x,-y,-z
     5  y,y-x,-z
     6  x-y,x,-z
     7  2/3+x,1/3+y,1/3+z
     8  2/3-y,1/3+x-y,1/3+z
     9  2/3+y-x,1/3-x,1/3+z
    10  2/3-x,1/3-y,1/3-z
    11  2/3+y,1/3+y-x,1/3-z
    12  2/3+x-y,1/3+x,1/3-z
    13  1/3+x,2/3+y,2/3+z
    14  1/3-y,2/3+x-y,2/3+z
    15  1/3+y-x,2/3-x,2/3+z
    16  1/3-x,2/3-y,2/3-z
    17  1/3+y,2/3+y-x,2/3-z
    18  1/3+x-y,2/3+x,2/3-z

# ATOMIC COORDINATES AND DISPLACEMENT PARAMETERS
loop_
   _atom_site_label
   _atom_site_type_symbol
   _atom_site_fract_x
   _atom_site_fract_y
   _atom_site_fract_z
```

```
   _atom_site_occupancy
   _atom_site_adp_type
   _atom_site_U_iso_or_equiv
   _atom_site_symmetry_multiplicity
Ca1    Ca2+ 0.00000     0.00000     0.00000     0.963      Uiso 0.010      3
Mg1    Mg2+ 0.00000     0.00000     0.00000     0.037      Uiso 0.010      3
Ca2    Ca2+ 0.00000     0.00000     0.50000     0.039      Uiso 0.010      3
Mg2    Mg2+ 0.00000     0.00000     0.50000     0.961      Uiso 0.010      3
C1     C    0.00000     0.00000     0.24266     1.000      Uiso 0.005      6
O1     O2-  0.24762     -0.03535    0.24406     1.000      Uiso 0.015      18

loop_  _atom_type_symbol _atom_type_number_in_cell
  C    6
  Ca   3.006
  Mg   2.994
  O    18

# Note that Z affects _cell_formula_sum and _weight
_cell_formula_units_Z  6
_chemical_formula_sum  "C Ca0.501 Mg0.499 O3"
_chemical_formula_weight  92.22
```

```
##############################################################################
#GF-1 1109 m

data_dolomite

# phase info for dolomite follows
_pd_phase_name  dolomite
_cell_length_a  4.810621
_cell_length_b  4.810621
_cell_length_c  16.029664
_cell_angle_alpha  90
_cell_angle_beta   90
_cell_angle_gamma  120
_cell_volume  321.261
_exptl_crystal_density_diffrn  2.8598
_symmetry_cell_setting  trigonal
_symmetry_space_group_name_H-M  "R -3"
loop_
    _space_group_symop_id
    _space_group_symop_operation_xyz
     1  x,y,z
     2  -y,x-y,z
     3  y-x,-x,z
     4  -x,-y,-z
     5  y,y-x,-z
     6  x-y,x,-z
     7  2/3+x,1/3+y,1/3+z
     8  2/3-y,1/3+x-y,1/3+z
     9  2/3+y-x,1/3-x,1/3+z
    10  2/3-x,1/3-y,1/3-z
    11  2/3+y,1/3+y-x,1/3-z
    12  2/3+x-y,1/3+x,1/3-z
    13  1/3+x,2/3+y,2/3+z
    14  1/3-y,2/3+x-y,2/3+z
    15  1/3+y-x,2/3-x,2/3+z
    16  1/3-x,2/3-y,2/3-z
    17  1/3+y,2/3+y-x,2/3-z
    18  1/3+x-y,2/3+x,2/3-z

# ATOMIC COORDINATES AND DISPLACEMENT PARAMETERS
loop_
   _atom_site_label
   _atom_site_type_symbol
   _atom_site_fract_x
   _atom_site_fract_y
   _atom_site_fract_z
```

```
   _atom_site_occupancy
   _atom_site_adp_type
   _atom_site_U_iso_or_equiv
   _atom_site_symmetry_multiplicity
Ca1    Ca2+ 0.00000     0.00000     0.00000     0.998900   Uiso 0.010      3
Mg1    Mg2+ 0.00000     0.00000     0.00000     0.00110000 Uiso 0.010      3
Ca2    Ca2+ 0.00000     0.00000     0.50000     0.00250000 Uiso 0.010      3
Mg2    Mg2+ 0.00000     0.00000     0.50000     0.997500   Uiso 0.010      3
C1     C    0.00000     0.00000     0.24266     1.000      Uiso 0.005      6
O1     O2-  0.24762     -0.03535    0.24406     1.000      Uiso 0.015      18

loop_  _atom_type_symbol _atom_type_number_in_cell
  C    6
  Ca   3.004
  Mg   2.996
  O    18

# Note that Z affects _cell_formula_sum and _weight
_cell_formula_units_Z  6
_chemical_formula_sum  "C Ca0.501 Mg0.499 O3"
_chemical_formula_weight  92.21
```

```
########################################################################
#HH-4

data_dolomite

# phase info for dolomite follows
_pd_phase_name  dolomite
_cell_length_a  4.809624
_cell_length_b  4.809624
_cell_length_c  16.019301
_cell_angle_alpha  90
_cell_angle_beta   90
_cell_angle_gamma  120
_cell_volume  320.92
_exptl_crystal_density_diffrn  2.8628
_symmetry_cell_setting  trigonal
_symmetry_space_group_name_H-M  "R -3"
loop_
    _space_group_symop_id
    _space_group_symop_operation_xyz
     1  x,y,z
     2  -y,x-y,z
     3  y-x,-x,z
     4  -x,-y,-z
     5  y,y-x,-z
     6  x-y,x,-z
     7  2/3+x,1/3+y,1/3+z
     8  2/3-y,1/3+x-y,1/3+z
     9  2/3+y-x,1/3-x,1/3+z
    10  2/3-x,1/3-y,1/3-z
    11  2/3+y,1/3+y-x,1/3-z
    12  2/3+x-y,1/3+x,1/3-z
    13  1/3+x,2/3+y,2/3+z
    14  1/3-y,2/3+x-y,2/3+z
    15  1/3+y-x,2/3-x,2/3+z
    16  1/3-x,2/3-y,2/3-z
    17  1/3+y,2/3+y-x,2/3-z
    18  1/3+x-y,2/3+x,2/3-z

# ATOMIC COORDINATES AND DISPLACEMENT PARAMETERS
loop_
   _atom_site_label
   _atom_site_type_symbol
   _atom_site_fract_x
   _atom_site_fract_y
   _atom_site_fract_z
```

```
   _atom_site_occupancy
   _atom_site_adp_type
   _atom_site_U_iso_or_equiv
   _atom_site_symmetry_multiplicity
Ca1    Ca2+ 0.00000     0.00000     0.00000     0.998900   Uiso 0.010      3
Mg1    Mg2+ 0.00000     0.00000     0.00000     0.00110000 Uiso 0.010      3
Ca2    Ca2+ 0.00000     0.00000     0.50000     0.00250000 Uiso 0.010      3
Mg2    Mg2+ 0.00000     0.00000     0.50000     0.997500   Uiso 0.010      3
C1     C    0.00000     0.00000     0.24266     1.000      Uiso 0.005      6
O1     O2-  0.24762     -0.03535    0.24406     1.000      Uiso 0.015      18

loop_  _atom_type_symbol _atom_type_number_in_cell
  C    6
  Ca   3.004
  Mg   2.996
  O    18

# Note that Z affects _cell_formula_sum and _weight
_cell_formula_units_Z  6
_chemical_formula_sum  "C Ca0.501 Mg0.499 O3"
_chemical_formula_weight  92.21
```

```
###########################################################################
HH-26

data_dolomite

# phase info for dolomite follows
_pd_phase_name  dolomite
_cell_length_a  4.809355
_cell_length_b  4.809355
_cell_length_c  16.020051
_cell_angle_alpha  90
_cell_angle_beta   90
_cell_angle_gamma  120
_cell_volume  320.899
_exptl_crystal_density_diffrn  2.8628
_symmetry_cell_setting  trigonal
_symmetry_space_group_name_H-M  "R -3"
loop_
    _space_group_symop_id
    _space_group_symop_operation_xyz
     1  x,y,z
     2  -y,x-y,z
     3  y-x,-x,z
     4  -x,-y,-z
     5  y,y-x,-z
     6  x-y,x,-z
     7  2/3+x,1/3+y,1/3+z
     8  2/3-y,1/3+x-y,1/3+z
     9  2/3+y-x,1/3-x,1/3+z
    10  2/3-x,1/3-y,1/3-z
    11  2/3+y,1/3+y-x,1/3-z
    12  2/3+x-y,1/3+x,1/3-z
    13  1/3+x,2/3+y,2/3+z
    14  1/3-y,2/3+x-y,2/3+z
    15  1/3+y-x,2/3-x,2/3+z
    16  1/3-x,2/3-y,2/3-z
    17  1/3+y,2/3+y-x,2/3-z
    18  1/3+x-y,2/3+x,2/3-z

# ATOMIC COORDINATES AND DISPLACEMENT PARAMETERS
loop_
   _atom_site_label
   _atom_site_type_symbol
   _atom_site_fract_x
   _atom_site_fract_y
   _atom_site_fract_z
```

```
   _atom_site_occupancy
   _atom_site_adp_type
   _atom_site_U_iso_or_equiv
   _atom_site_symmetry_multiplicity
Ca1    Ca2+ 0.00000     0.00000     0.00000     0.968      Uiso 0.010      3
Mg1    Mg2+ 0.00000     0.00000     0.00000     0.032      Uiso 0.010      3
Ca2    Ca2+ 0.00000     0.00000     0.50000     0.033      Uiso 0.010      3
Mg2    Mg2+ 0.00000     0.00000     0.50000     0.967      Uiso 0.010      3
C1     C    0.00000     0.00000     0.24266     1.000      Uiso 0.005      6
O1     O2-  0.24762     -0.03535    0.24406     1.000      Uiso 0.015      18

loop_  _atom_type_symbol _atom_type_number_in_cell
  C    6
  Ca   3.003
  Mg   2.997
  O    18

# Note that Z affects _cell_formula_sum and _weight
_cell_formula_units_Z  6
_chemical_formula_sum  "C Ca0.5 Mg0.5 O3"
_chemical_formula_weight  92.21
```

```
#############################################################################
#MGY-1 253.8 m

data_dolomite

# phase info for dolomite follows
_pd_phase_name  dolomite
_cell_length_a  4.809039
_cell_length_b  4.809039
_cell_length_c  16.020048
_cell_angle_alpha  90
_cell_angle_beta   90
_cell_angle_gamma  120
_cell_volume  320.857
_exptl_crystal_density_diffrn  2.8620
_symmetry_cell_setting  trigonal
_symmetry_space_group_name_H-M  "R -3"
loop_
    _space_group_symop_id
    _space_group_symop_operation_xyz
     1  x,y,z
     2  -y,x-y,z
     3  y-x,-x,z
     4  -x,-y,-z
     5  y,y-x,-z
     6  x-y,x,-z
     7  2/3+x,1/3+y,1/3+z
     8  2/3-y,1/3+x-y,1/3+z
     9  2/3+y-x,1/3-x,1/3+z
    10  2/3-x,1/3-y,1/3-z
    11  2/3+y,1/3+y-x,1/3-z
    12  2/3+x-y,1/3+x,1/3-z
    13  1/3+x,2/3+y,2/3+z
    14  1/3-y,2/3+x-y,2/3+z
    15  1/3+y-x,2/3-x,2/3+z
    16  1/3-x,2/3-y,2/3-z
    17  1/3+y,2/3+y-x,2/3-z
    18  1/3+x-y,2/3+x,2/3-z

# ATOMIC COORDINATES AND DISPLACEMENT PARAMETERS
loop_
   _atom_site_label
   _atom_site_type_symbol
   _atom_site_fract_x
   _atom_site_fract_y
   _atom_site_fract_z
```

```
   _atom_site_occupancy
   _atom_site_adp_type
   _atom_site_U_iso_or_equiv
   _atom_site_symmetry_multiplicity
Ca1    Ca2+ 0.00000     0.00000     0.00000     0.969      Uiso 0.010      3
Mg1    Mg2+ 0.00000     0.00000     0.00000     0.031      Uiso 0.010      3
Ca2    Ca2+ 0.00000     0.00000     0.50000     0.027      Uiso 0.010      3
Mg2    Mg2+ 0.00000     0.00000     0.50000     0.973      Uiso 0.010      3
C1     C    0.00000     0.00000     0.24266     1.000      Uiso 0.005      6
O1     O2-  0.24762     -0.03535    0.24406     1.000      Uiso 0.015      18

loop_  _atom_type_symbol _atom_type_number_in_cell
  C    6
  Ca   2.987
  Mg   3.013
  O    18

# Note that Z affects _cell_formula_sum and _weight
_cell_formula_units_Z  6
_chemical_formula_sum  "C Ca0.498 Mg0.502 O3"
_chemical_formula_weight  92.17
```

```
###########################################################################
#MGY-1 333.5 m

data_dolomite

# phase info for dolomite follows
_pd_phase_name  dolomite
_cell_length_a  4.81702
_cell_length_b  4.81702
_cell_length_c  16.083418
_cell_angle_alpha  90
_cell_angle_beta   90
_cell_angle_gamma  120
_cell_volume  323.196
_exptl_crystal_density_diffrn  2.8426
_symmetry_cell_setting  trigonal
_symmetry_space_group_name_H-M  "R -3"
loop_
    _space_group_symop_id
    _space_group_symop_operation_xyz
     1  x,y,z
     2  -y,x-y,z
     3  y-x,-x,z
     4  -x,-y,-z
     5  y,y-x,-z
     6  x-y,x,-z
     7  2/3+x,1/3+y,1/3+z
     8  2/3-y,1/3+x-y,1/3+z
     9  2/3+y-x,1/3-x,1/3+z
    10  2/3-x,1/3-y,1/3-z
    11  2/3+y,1/3+y-x,1/3-z
    12  2/3+x-y,1/3+x,1/3-z
    13  1/3+x,2/3+y,2/3+z
    14  1/3-y,2/3+x-y,2/3+z
    15  1/3+y-x,2/3-x,2/3+z
    16  1/3-x,2/3-y,2/3-z
    17  1/3+y,2/3+y-x,2/3-z
    18  1/3+x-y,2/3+x,2/3-z

# ATOMIC COORDINATES AND DISPLACEMENT PARAMETERS
loop_
   _atom_site_label
   _atom_site_type_symbol
   _atom_site_fract_x
   _atom_site_fract_y
   _atom_site_fract_z
```

```
   _atom_site_occupancy
   _atom_site_adp_type
   _atom_site_U_iso_or_equiv
   _atom_site_symmetry_multiplicity
Ca1    Ca2+ 0.00000     0.00000     0.00000     0.999      Uiso 0.010      3
Mg1    Mg2+ 0.00000     0.00000     0.00000     0.001      Uiso 0.010      3
Ca2    Ca2+ 0.00000     0.00000     0.50000     0.003      Uiso 0.010      3
Mg2    Mg2+ 0.00000     0.00000     0.50000     0.998      Uiso 0.010      3
C1     C    0.00000     0.00000     0.24266     1.000      Uiso 0.005      6
O1     O2-  0.24762     -0.03535    0.24406     1.000      Uiso 0.015      18

loop_  _atom_type_symbol _atom_type_number_in_cell
  C    6
  Ca   3.004
  Mg   2.996
  O    18

# Note that Z affects _cell_formula_sum and _weight
_cell_formula_units_Z  6
_chemical_formula_sum  "C Ca0.501 Mg0.499 O3"
_chemical_formula_weight  92.21
```

```
###########################################################################
#MGY-1 346.9 m

data_dolomite

# phase info for dolomite follows
_pd_phase_name  dolomite
_cell_length_a  4.810481
_cell_length_b  4.810481
_cell_length_c  16.029475
_cell_angle_alpha  90
_cell_angle_beta   90
_cell_angle_gamma  120
_cell_volume  321.238
_exptl_crystal_density_diffrn  2.8600
_symmetry_cell_setting  trigonal
_symmetry_space_group_name_H-M  "R -3"
loop_
    _space_group_symop_id
    _space_group_symop_operation_xyz
     1  x,y,z
     2  -y,x-y,z
     3  y-x,-x,z
     4  -x,-y,-z
     5  y,y-x,-z
     6  x-y,x,-z
     7  2/3+x,1/3+y,1/3+z
     8  2/3-y,1/3+x-y,1/3+z
     9  2/3+y-x,1/3-x,1/3+z
    10  2/3-x,1/3-y,1/3-z
    11  2/3+y,1/3+y-x,1/3-z
    12  2/3+x-y,1/3+x,1/3-z
    13  1/3+x,2/3+y,2/3+z
    14  1/3-y,2/3+x-y,2/3+z
    15  1/3+y-x,2/3-x,2/3+z
    16  1/3-x,2/3-y,2/3-z
    17  1/3+y,2/3+y-x,2/3-z
    18  1/3+x-y,2/3+x,2/3-z

# ATOMIC COORDINATES AND DISPLACEMENT PARAMETERS
loop_
   _atom_site_label
   _atom_site_type_symbol
   _atom_site_fract_x
   _atom_site_fract_y
   _atom_site_fract_z
```

```
   _atom_site_occupancy
   _atom_site_adp_type
   _atom_site_U_iso_or_equiv
   _atom_site_symmetry_multiplicity
Ca1    Ca2+ 0.00000     0.00000     0.00000     0.998900   Uiso 0.010      3
Mg1    Mg2+ 0.00000     0.00000     0.00000     0.00110000 Uiso 0.010      3
Ca2    Ca2+ 0.00000     0.00000     0.50000     0.00250000 Uiso 0.010      3
Mg2    Mg2+ 0.00000     0.00000     0.50000     0.997500   Uiso 0.010      3
C1     C    0.00000     0.00000     0.24266     1.000      Uiso 0.005      6
O1     O2-  0.24762     -0.03535    0.24406     1.000      Uiso 0.015      18

loop_  _atom_type_symbol _atom_type_number_in_cell
  C    6
  Ca   3.004
  Mg   2.996
  O    18

# Note that Z affects _cell_formula_sum and _weight
_cell_formula_units_Z  6
_chemical_formula_sum  "C Ca0.501 Mg0.499 O3"
_chemical_formula_weight  92.21
```

```
##############################################################################
#MGY-1 366.5 m

data_dolomite

# phase info for dolomite follows
_pd_phase_name  dolomite
_cell_length_a  4.811514
_cell_length_b  4.811514
_cell_length_c  16.038967
_cell_angle_alpha  90
_cell_angle_beta   90
_cell_angle_gamma  120
_cell_volume  321.566
_exptl_crystal_density_diffrn  2.8570
_symmetry_cell_setting  trigonal
_symmetry_space_group_name_H-M  "R -3"
loop_
    _space_group_symop_id
    _space_group_symop_operation_xyz
     1  x,y,z
     2  -y,x-y,z
     3  y-x,-x,z
     4  -x,-y,-z
     5  y,y-x,-z
     6  x-y,x,-z
     7  2/3+x,1/3+y,1/3+z
     8  2/3-y,1/3+x-y,1/3+z
     9  2/3+y-x,1/3-x,1/3+z
    10  2/3-x,1/3-y,1/3-z
    11  2/3+y,1/3+y-x,1/3-z
    12  2/3+x-y,1/3+x,1/3-z
    13  1/3+x,2/3+y,2/3+z
    14  1/3-y,2/3+x-y,2/3+z
    15  1/3+y-x,2/3-x,2/3+z
    16  1/3-x,2/3-y,2/3-z
    17  1/3+y,2/3+y-x,2/3-z
    18  1/3+x-y,2/3+x,2/3-z

# ATOMIC COORDINATES AND DISPLACEMENT PARAMETERS
loop_
   _atom_site_label
   _atom_site_type_symbol
   _atom_site_fract_x
   _atom_site_fract_y
   _atom_site_fract_z
```

```
   _atom_site_occupancy
   _atom_site_adp_type
   _atom_site_U_iso_or_equiv
   _atom_site_symmetry_multiplicity
Ca1    Ca2+ 0.00000     0.00000     0.00000     0.998900   Uiso 0.010      3
Mg1    Mg2+ 0.00000     0.00000     0.00000     0.00110000 Uiso 0.010      3
Ca2    Ca2+ 0.00000     0.00000     0.50000     0.00250000 Uiso 0.010      3
Mg2    Mg2+ 0.00000     0.00000     0.50000     0.997500   Uiso 0.010      3
C1     C    0.00000     0.00000     0.24266     1.000      Uiso 0.005      6
O1     O2-  0.24762     -0.03535    0.24406     1.000      Uiso 0.015      18

loop_  _atom_type_symbol _atom_type_number_in_cell
  C    6
  Ca   3.004
  Mg   2.996
  O    18

# Note that Z affects _cell_formula_sum and _weight
_cell_formula_units_Z  6
_chemical_formula_sum  "C Ca0.501 Mg0.499 O3"
_chemical_formula_weight  92.21
```

```
#########################################################################################
#MGY-1 381.5 m

data_dolomite

# phase info for dolomite follows
_pd_phase_name  dolomite
_cell_length_a  4.812253
_cell_length_b  4.812253
_cell_length_c  16.040032
_cell_angle_alpha  90
_cell_angle_beta   90
_cell_angle_gamma  120
_cell_volume  321.686
_exptl_crystal_density_diffrn  2.8560
_symmetry_cell_setting  trigonal
_symmetry_space_group_name_H-M  "R -3"
loop_
    _space_group_symop_id
    _space_group_symop_operation_xyz
     1  x,y,z
     2  -y,x-y,z
     3  y-x,-x,z
     4  -x,-y,-z
     5  y,y-x,-z
     6  x-y,x,-z
     7  2/3+x,1/3+y,1/3+z
     8  2/3-y,1/3+x-y,1/3+z
     9  2/3+y-x,1/3-x,1/3+z
    10  2/3-x,1/3-y,1/3-z
    11  2/3+y,1/3+y-x,1/3-z
    12  2/3+x-y,1/3+x,1/3-z
    13  1/3+x,2/3+y,2/3+z
    14  1/3-y,2/3+x-y,2/3+z
    15  1/3+y-x,2/3-x,2/3+z
    16  1/3-x,2/3-y,2/3-z
    17  1/3+y,2/3+y-x,2/3-z
    18  1/3+x-y,2/3+x,2/3-z

# ATOMIC COORDINATES AND DISPLACEMENT PARAMETERS
loop_
   _atom_site_label
   _atom_site_type_symbol
   _atom_site_fract_x
   _atom_site_fract_y
   _atom_site_fract_z
```

```
   _atom_site_occupancy
   _atom_site_adp_type
   _atom_site_U_iso_or_equiv
   _atom_site_symmetry_multiplicity
Ca1    Ca2+ 0.00000     0.00000     0.00000     0.998900   Uiso 0.010      3
Mg1    Mg2+ 0.00000     0.00000     0.00000     0.00110000 Uiso 0.010      3
Ca2    Ca2+ 0.00000     0.00000     0.50000     0.00250000 Uiso 0.010      3
Mg2    Mg2+ 0.00000     0.00000     0.50000     0.997500   Uiso 0.010      3
C1     C    0.00000     0.00000     0.24266     1.000      Uiso 0.005      6
O1     O2-  0.24762     -0.03535    0.24406     1.000      Uiso 0.015      18

loop_  _atom_type_symbol _atom_type_number_in_cell
  C    6
  Ca   3.004
  Mg   2.996
  O    18

# Note that Z affects _cell_formula_sum and _weight
_cell_formula_units_Z  6
_chemical_formula_sum  "C Ca0.501 Mg0.499 O3"
_chemical_formula_weight  92.21
```

```
##########################################################################
#VA-3T/1

data_dolomite

# phase info for dolomite follows
_pd_phase_name  dolomite
_cell_length_a  4.809711
_cell_length_b  4.809711
_cell_length_c  16.022453
_cell_angle_alpha  90
_cell_angle_beta   90
_cell_angle_gamma  120
_cell_volume  320.994
_exptl_crystal_density_diffrn  2.8719
_symmetry_cell_setting  trigonal
_symmetry_space_group_name_H-M  "R -3"
loop_
    _space_group_symop_id
    _space_group_symop_operation_xyz
     1  x,y,z
     2  -y,x-y,z
     3  y-x,-x,z
     4  -x,-y,-z
     5  y,y-x,-z
     6  x-y,x,-z
     7  2/3+x,1/3+y,1/3+z
     8  2/3-y,1/3+x-y,1/3+z
     9  2/3+y-x,1/3-x,1/3+z
    10  2/3-x,1/3-y,1/3-z
    11  2/3+y,1/3+y-x,1/3-z
    12  2/3+x-y,1/3+x,1/3-z
    13  1/3+x,2/3+y,2/3+z
    14  1/3-y,2/3+x-y,2/3+z
    15  1/3+y-x,2/3-x,2/3+z
    16  1/3-x,2/3-y,2/3-z
    17  1/3+y,2/3+y-x,2/3-z
    18  1/3+x-y,2/3+x,2/3-z

# ATOMIC COORDINATES AND DISPLACEMENT PARAMETERS
loop_
   _atom_site_label
   _atom_site_type_symbol
   _atom_site_fract_x
   _atom_site_fract_y
   _atom_site_fract_z
```

```
   _atom_site_occupancy
   _atom_site_adp_type
   _atom_site_U_iso_or_equiv
   _atom_site_symmetry_multiplicity
Ca1    Ca2+ 0.00000     0.00000     0.00000     0.996      Uiso 0.010      3
Mg1    Mg2+ 0.00000     0.00000     0.00000     0.004      Uiso 0.010      3
Ca2    Ca2+ 0.00000     0.00000     0.50000     0.045      Uiso 0.010      3
Mg2    Mg2+ 0.00000     0.00000     0.50000     0.955      Uiso 0.010      3
C1     C    0.00000     0.00000     0.24266     1.000      Uiso 0.005      6
O1     O2-  0.24762     -0.03535    0.24406     1.000      Uiso 0.015      18

loop_  _atom_type_symbol _atom_type_number_in_cell
  C    6
  Ca   3.124
  Mg   2.876
  O    18

# Note that Z affects _cell_formula_sum and _weight
_cell_formula_units_Z  6
_chemical_formula_sum  "C Ca0.521 Mg0.479 O3"
_chemical_formula_weight  92.53
```

```
#############################################################################
#ZB-4

data_dolomite

# phase info for dolomite follows
_pd_phase_name  dolomite
_cell_length_a  4.809453
_cell_length_b  4.809453
_cell_length_c  16.021844
_cell_angle_alpha  90
_cell_angle_beta   90
_cell_angle_gamma  120
_cell_volume  320.948
_exptl_crystal_density_diffrn  2.8856
_symmetry_cell_setting  trigonal
_symmetry_space_group_name_H-M  "R -3"
loop_
    _space_group_symop_id
    _space_group_symop_operation_xyz
     1  x,y,z
     2  -y,x-y,z
     3  y-x,-x,z
     4  -x,-y,-z
     5  y,y-x,-z
     6  x-y,x,-z
     7  2/3+x,1/3+y,1/3+z
     8  2/3-y,1/3+x-y,1/3+z
     9  2/3+y-x,1/3-x,1/3+z
    10  2/3-x,1/3-y,1/3-z
    11  2/3+y,1/3+y-x,1/3-z
    12  2/3+x-y,1/3+x,1/3-z
    13  1/3+x,2/3+y,2/3+z
    14  1/3-y,2/3+x-y,2/3+z
    15  1/3+y-x,2/3-x,2/3+z
    16  1/3-x,2/3-y,2/3-z
    17  1/3+y,2/3+y-x,2/3-z
    18  1/3+x-y,2/3+x,2/3-z

# ATOMIC COORDINATES AND DISPLACEMENT PARAMETERS
loop_
   _atom_site_label
   _atom_site_type_symbol
   _atom_site_fract_x
   _atom_site_fract_y
   _atom_site_fract_z
```

```
   _atom_site_occupancy
   _atom_site_adp_type
   _atom_site_U_iso_or_equiv
   _atom_site_symmetry_multiplicity
Ca1    Ca2+ 0.00000     0.00000     0.00000     0.999      Uiso 0.010      3
Mg1    Mg2+ 0.00000     0.00000     0.00000     0.001      Uiso 0.010      3
Ca2    Ca2+ 0.00000     0.00000     0.50000     0.096      Uiso 0.010      3
Mg2    Mg2+ 0.00000     0.00000     0.50000     0.904      Uiso 0.010      3
C1     C    0.00000     0.00000     0.24266     1.000      Uiso 0.005      6
O1     O2-  0.24762     -0.03535    0.24406     1.000      Uiso 0.015      18

loop_  _atom_type_symbol _atom_type_number_in_cell
  C    6
  Ca   3.287
  Mg   2.713
  O    18

# Note that Z affects _cell_formula_sum and _weight
_cell_formula_units_Z  6
_chemical_formula_sum  "C Ca0.548 Mg0.452 O3"
_chemical_formula_weight  92.95
```

```
########################################################################
#ZB-6

data_dolomite

# phase info for dolomite follows
_pd_phase_name  dolomite
_cell_length_a  4.808916
_cell_length_b  4.808916
_cell_length_c  16.016827
_cell_angle_alpha  90
_cell_angle_beta   90
_cell_angle_gamma  120
_cell_volume  320.776
_exptl_crystal_density_diffrn  2.8786
_symmetry_cell_setting  trigonal
_symmetry_space_group_name_H-M  "R -3"
loop_
    _space_group_symop_id
    _space_group_symop_operation_xyz
     1  x,y,z
     2  -y,x-y,z
     3  y-x,-x,z
     4  -x,-y,-z
     5  y,y-x,-z
     6  x-y,x,-z
     7  2/3+x,1/3+y,1/3+z
     8  2/3-y,1/3+x-y,1/3+z
     9  2/3+y-x,1/3-x,1/3+z
    10  2/3-x,1/3-y,1/3-z
    11  2/3+y,1/3+y-x,1/3-z
    12  2/3+x-y,1/3+x,1/3-z
    13  1/3+x,2/3+y,2/3+z
    14  1/3-y,2/3+x-y,2/3+z
    15  1/3+y-x,2/3-x,2/3+z
    16  1/3-x,2/3-y,2/3-z
    17  1/3+y,2/3+y-x,2/3-z
    18  1/3+x-y,2/3+x,2/3-z

# ATOMIC COORDINATES AND DISPLACEMENT PARAMETERS
loop_
   _atom_site_label
   _atom_site_type_symbol
   _atom_site_fract_x
   _atom_site_fract_y
   _atom_site_fract_z
```

```
   _atom_site_occupancy
   _atom_site_adp_type
   _atom_site_U_iso_or_equiv
   _atom_site_symmetry_multiplicity
Ca1    Ca2+ 0.00000     0.00000     0.00000     0.978      Uiso 0.010      3
Mg1    Mg2+ 0.00000     0.00000     0.00000     0.022      Uiso 0.010      3
Ca2    Ca2+ 0.00000     0.00000     0.50000     0.082      Uiso 0.010      3
Mg2    Mg2+ 0.00000     0.00000     0.50000     0.918      Uiso 0.010      3
C1     C    0.00000     0.00000     0.24266     1.000      Uiso 0.005      6
O1     O2-  0.24762     -0.03535    0.24406     1.000      Uiso 0.015      18

loop_  _atom_type_symbol _atom_type_number_in_cell
  C    6
  Ca   3.183
  Mg   2.817
  O    18

# Note that Z affects _cell_formula_sum and _weight
_cell_formula_units_Z  6
_chemical_formula_sum  "C Ca0.53 Mg0.47 O3"
_chemical_formula_weight  92.68
```

A1.2. Joint Rietveld refinement results of synchrotron X-ray and neutron diffraction data

```
##############################################################################
#H-1(HH-26)

data_dolomite

# phase info for dolomite follows
_pd_phase_name  dolomite
_cell_length_a  4.811375
_cell_length_b  4.811375
_cell_length_c  16.031435
_cell_angle_alpha  90
_cell_angle_beta   90
_cell_angle_gamma  120
_cell_volume  321.397
_exptl_crystal_density_diffrn  2.8585
_symmetry_cell_setting  trigonal
_symmetry_space_group_name_H-M  "R -3"
loop_
    _space_group_symop_id
    _space_group_symop_operation_xyz
     1  x,y,z
     2  -y,x-y,z
     3  y-x,-x,z
     4  -x,-y,-z
     5  y,y-x,-z
     6  x-y,x,-z
     7  2/3+x,1/3+y,1/3+z
     8  2/3-y,1/3+x-y,1/3+z
     9  2/3+y-x,1/3-x,1/3+z
    10  2/3-x,1/3-y,1/3-z
    11  2/3+y,1/3+y-x,1/3-z
    12  2/3+x-y,1/3+x,1/3-z
    13  1/3+x,2/3+y,2/3+z
    14  1/3-y,2/3+x-y,2/3+z
    15  1/3+y-x,2/3-x,2/3+z
    16  1/3-x,2/3-y,2/3-z
    17  1/3+y,2/3+y-x,2/3-z
    18  1/3+x-y,2/3+x,2/3-z

# ATOMIC COORDINATES AND DISPLACEMENT PARAMETERS
loop_
   _atom_site_label
   _atom_site_type_symbol
```

```
   _atom_site_fract_x
   _atom_site_fract_y
   _atom_site_fract_z
   _atom_site_occupancy
   _atom_site_adp_type
   _atom_site_U_iso_or_equiv
   _atom_site_symmetry_multiplicity
Ca1    Ca2+ 0.00000     0.00000     0.00000     0.999      Uiso 0.010      3
Mg1    Mg2+ 0.00000     0.00000     0.00000     0.001      Uiso 0.010      3
Ca2    Ca2+ 0.00000     0.00000     0.50000     0.003      Uiso 0.010      3
Mg2    Mg2+ 0.00000     0.00000     0.50000     0.998      Uiso 0.010      3
C1     C    0.00000     0.00000     0.24266     1.000      Uiso 0.005      6
O1     O2-  0.24762     -0.03535    0.24406     1.000      Uiso 0.015      18

loop_  _atom_type_symbol _atom_type_number_in_cell
  C    6
  Ca   3.004
  Mg   2.996
  O    18

# Note that Z affects _cell_formula_sum and _weight
_cell_formula_units_Z  6
_chemical_formula_sum  "C Ca0.501 Mg0.499 O3"
_chemical_formula_weight  92.21
```

```
###########################################################################
#HH2/1

data_dolomite

# phase info for dolomite follows
_pd_phase_name  dolomite
_cell_length_a  4.80949
_cell_length_b  4.80949
_cell_length_c  16.015938
_cell_angle_alpha  90
_cell_angle_beta   90
_cell_angle_gamma  120
_cell_volume  320.834
_exptl_crystal_density_diffrn  2.8636
_symmetry_cell_setting  trigonal
_symmetry_space_group_name_H-M  "R -3"
loop_
    _space_group_symop_id
    _space_group_symop_operation_xyz
     1  x,y,z
     2  -y,x-y,z
     3  y-x,-x,z
     4  -x,-y,-z
     5  y,y-x,-z
     6  x-y,x,-z
     7  2/3+x,1/3+y,1/3+z
     8  2/3-y,1/3+x-y,1/3+z
     9  2/3+y-x,1/3-x,1/3+z
    10  2/3-x,1/3-y,1/3-z
    11  2/3+y,1/3+y-x,1/3-z
    12  2/3+x-y,1/3+x,1/3-z
    13  1/3+x,2/3+y,2/3+z
    14  1/3-y,2/3+x-y,2/3+z
    15  1/3+y-x,2/3-x,2/3+z
    16  1/3-x,2/3-y,2/3-z
    17  1/3+y,2/3+y-x,2/3-z
    18  1/3+x-y,2/3+x,2/3-z

# ATOMIC COORDINATES AND DISPLACEMENT PARAMETERS
loop_
   _atom_site_label
   _atom_site_type_symbol
   _atom_site_fract_x
   _atom_site_fract_y
   _atom_site_fract_z
```

```
   _atom_site_occupancy
   _atom_site_adp_type
   _atom_site_U_iso_or_equiv
   _atom_site_symmetry_multiplicity
Ca1    Ca2+ 0.00000     0.00000     0.00000     0.999      Uiso 0.010      3
Mg1    Mg2+ 0.00000     0.00000     0.00000     0.001      Uiso 0.010      3
Ca2    Ca2+ 0.00000     0.00000     0.50000     0.003      Uiso 0.010      3
Mg2    Mg2+ 0.00000     0.00000     0.50000     0.998      Uiso 0.010      3
C1     C    0.00000     0.00000     0.24266     1.000      Uiso 0.005      6
O1     O2-  0.24762     -0.03535    0.24406     1.000      Uiso 0.015      18

loop_  _atom_type_symbol _atom_type_number_in_cell
  C    6
  Ca   3.004
  Mg   2.996
  O    18

# Note that Z affects _cell_formula_sum and _weight
_cell_formula_units_Z  6
_chemical_formula_sum  "C Ca0.501 Mg0.499 O3"
_chemical_formula_weight  92.21
```

```
#############################################################################
#HHUB18(HH4)

data_dolomite

# phase info for dolomite follows
_pd_phase_name  dolomite
_cell_length_a  4.808704
_cell_length_b  4.808704
_cell_length_c  16.011535
_cell_angle_alpha  90
_cell_angle_beta   90
_cell_angle_gamma  120
_cell_volume  320.642
_exptl_crystal_density_diffrn  2.8653
_symmetry_cell_setting  trigonal
_symmetry_space_group_name_H-M  "R -3"
loop_
    _space_group_symop_id
    _space_group_symop_operation_xyz
     1  x,y,z
     2  -y,x-y,z
     3  y-x,-x,z
     4  -x,-y,-z
     5  y,y-x,-z
     6  x-y,x,-z
     7  2/3+x,1/3+y,1/3+z
     8  2/3-y,1/3+x-y,1/3+z
     9  2/3+y-x,1/3-x,1/3+z
    10  2/3-x,1/3-y,1/3-z
    11  2/3+y,1/3+y-x,1/3-z
    12  2/3+x-y,1/3+x,1/3-z
    13  1/3+x,2/3+y,2/3+z
    14  1/3-y,2/3+x-y,2/3+z
    15  1/3+y-x,2/3-x,2/3+z
    16  1/3-x,2/3-y,2/3-z
    17  1/3+y,2/3+y-x,2/3-z
    18  1/3+x-y,2/3+x,2/3-z

# ATOMIC COORDINATES AND DISPLACEMENT PARAMETERS
loop_
   _atom_site_label
   _atom_site_type_symbol
   _atom_site_fract_x
   _atom_site_fract_y
   _atom_site_fract_z
```

```
   _atom_site_occupancy
   _atom_site_adp_type
   _atom_site_U_iso_or_equiv
   _atom_site_symmetry_multiplicity
Ca1    Ca2+ 0.00000     0.00000     0.00000     0.999      Uiso 0.010      3
Mg1    Mg2+ 0.00000     0.00000     0.00000     0.001      Uiso 0.010      3
Ca2    Ca2+ 0.00000     0.00000     0.50000     0.003      Uiso 0.010      3
Mg2    Mg2+ 0.00000     0.00000     0.50000     0.998      Uiso 0.010      3
C1     C    0.00000     0.00000     0.24266     1.000      Uiso 0.005      6
O1     O2-  0.24762     -0.03535    0.24406     1.000      Uiso 0.015      18

loop_  _atom_type_symbol _atom_type_number_in_cell
  C    6
  Ca   3.004
  Mg   2.996
  O    18

# Note that Z affects _cell_formula_sum and _weight
_cell_formula_units_Z  6
_chemical_formula_sum  "C Ca0.501 Mg0.499 O3"
_chemical_formula_weight  92.21
```

```
##############################################################################
#MGY-1 381.5 m

data_dolomite

# phase info for dolomite follows
_pd_phase_name  dolomite
_cell_length_a  4.814467
_cell_length_b  4.814467
_cell_length_c  16.046993
_cell_angle_alpha  90
_cell_angle_beta   90
_cell_angle_gamma  120
_cell_volume  322.122
_exptl_crystal_density_diffrn  2.8521
_symmetry_cell_setting  trigonal
_symmetry_space_group_name_H-M  "R -3"
loop_
    _space_group_symop_id
    _space_group_symop_operation_xyz
     1  x,y,z
     2  -y,x-y,z
     3  y-x,-x,z
     4  -x,-y,-z
     5  y,y-x,-z
     6  x-y,x,-z
     7  2/3+x,1/3+y,1/3+z
     8  2/3-y,1/3+x-y,1/3+z
     9  2/3+y-x,1/3-x,1/3+z
    10  2/3-x,1/3-y,1/3-z
    11  2/3+y,1/3+y-x,1/3-z
    12  2/3+x-y,1/3+x,1/3-z
    13  1/3+x,2/3+y,2/3+z
    14  1/3-y,2/3+x-y,2/3+z
    15  1/3+y-x,2/3-x,2/3+z
    16  1/3-x,2/3-y,2/3-z
    17  1/3+y,2/3+y-x,2/3-z
    18  1/3+x-y,2/3+x,2/3-z

# ATOMIC COORDINATES AND DISPLACEMENT PARAMETERS
loop_
   _atom_site_label
   _atom_site_type_symbol
   _atom_site_fract_x
   _atom_site_fract_y
   _atom_site_fract_z
```

```
   _atom_site_occupancy
   _atom_site_adp_type
   _atom_site_U_iso_or_equiv
   _atom_site_symmetry_multiplicity
Ca1    Ca2+ 0.00000     0.00000     0.00000     0.999      Uiso 0.010      3
Mg1    Mg2+ 0.00000     0.00000     0.00000     0.001      Uiso 0.010      3
Ca2    Ca2+ 0.00000     0.00000     0.50000     0.003      Uiso 0.010      3
Mg2    Mg2+ 0.00000     0.00000     0.50000     0.998      Uiso 0.010      3
C1     C    0.00000     0.00000     0.24266     1.000      Uiso 0.005      6
O1     O2-  0.24762     -0.03535    0.24406     1.000      Uiso 0.015      18

loop_  _atom_type_symbol _atom_type_number_in_cell
  C    6
  Ca   3.004
  Mg   2.996
  O    18

# Note that Z affects _cell_formula_sum and _weight
_cell_formula_units_Z  6
_chemical_formula_sum  "C Ca0.501 Mg0.499 O3"
_chemical_formula_weight  92.21
```

```
##########################################################################
#VA-7(VA 3T/1)

data_dolomite

# phase info for dolomite follows
_pd_phase_name  dolomite
_cell_length_a  4.809696
_cell_length_b  4.809696
_cell_length_c  16.017537
_cell_angle_alpha  90
_cell_angle_beta   90
_cell_angle_gamma  120
_cell_volume  320.894
_exptl_crystal_density_diffrn  2.8630
_symmetry_cell_setting  trigonal
_symmetry_space_group_name_H-M  "R -3"
loop_
    _space_group_symop_id
    _space_group_symop_operation_xyz
     1  x,y,z
     2  -y,x-y,z
     3  y-x,-x,z
     4  -x,-y,-z
     5  y,y-x,-z
     6  x-y,x,-z
     7  2/3+x,1/3+y,1/3+z
     8  2/3-y,1/3+x-y,1/3+z
     9  2/3+y-x,1/3-x,1/3+z
    10  2/3-x,1/3-y,1/3-z
    11  2/3+y,1/3+y-x,1/3-z
    12  2/3+x-y,1/3+x,1/3-z
    13  1/3+x,2/3+y,2/3+z
    14  1/3-y,2/3+x-y,2/3+z
    15  1/3+y-x,2/3-x,2/3+z
    16  1/3-x,2/3-y,2/3-z
    17  1/3+y,2/3+y-x,2/3-z
    18  1/3+x-y,2/3+x,2/3-z

# ATOMIC COORDINATES AND DISPLACEMENT PARAMETERS
loop_
   _atom_site_label
   _atom_site_type_symbol
   _atom_site_fract_x
   _atom_site_fract_y
   _atom_site_fract_z
```

```
   _atom_site_occupancy
   _atom_site_adp_type
   _atom_site_U_iso_or_equiv
   _atom_site_symmetry_multiplicity
Ca1    Ca2+ 0.00000     0.00000     0.00000     0.999      Uiso 0.010      3
Mg1    Mg2+ 0.00000     0.00000     0.00000     0.001      Uiso 0.010      3
Ca2    Ca2+ 0.00000     0.00000     0.50000     0.003      Uiso 0.010      3
Mg2    Mg2+ 0.00000     0.00000     0.50000     0.998      Uiso 0.010      3
C1     C    0.00000     0.00000     0.24266     1.000      Uiso 0.005      6
O1     O2-  0.24762     -0.03535    0.24406     1.000      Uiso 0.015      18

loop_  _atom_type_symbol _atom_type_number_in_cell
  C    6
  Ca   3.004
  Mg   2.996
  O    18

# Note that Z affects _cell_formula_sum and _weight
_cell_formula_units_Z  6
_chemical_formula_sum  "C Ca0.501 Mg0.499 O3"
_chemical_formula_weight  92.21
```

```
#########################################################################
#ZB-4

data_dolomite

# phase info for dolomite follows
_pd_phase_name  dolomite
_cell_length_a  4.810404
_cell_length_b  4.810404
_cell_length_c  16.021761
_cell_angle_alpha  90
_cell_angle_beta   90
_cell_angle_gamma  120
_cell_volume  321.073
_exptl_crystal_density_diffrn  2.8614
_symmetry_cell_setting  trigonal
_symmetry_space_group_name_H-M  "R -3"
loop_
    _space_group_symop_id
    _space_group_symop_operation_xyz
     1  x,y,z
     2  -y,x-y,z
     3  y-x,-x,z
     4  -x,-y,-z
     5  y,y-x,-z
     6  x-y,x,-z
     7  2/3+x,1/3+y,1/3+z
     8  2/3-y,1/3+x-y,1/3+z
     9  2/3+y-x,1/3-x,1/3+z
    10  2/3-x,1/3-y,1/3-z
    11  2/3+y,1/3+y-x,1/3-z
    12  2/3+x-y,1/3+x,1/3-z
    13  1/3+x,2/3+y,2/3+z
    14  1/3-y,2/3+x-y,2/3+z
    15  1/3+y-x,2/3-x,2/3+z
    16  1/3-x,2/3-y,2/3-z
    17  1/3+y,2/3+y-x,2/3-z
    18  1/3+x-y,2/3+x,2/3-z

# ATOMIC COORDINATES AND DISPLACEMENT PARAMETERS
loop_
   _atom_site_label
   _atom_site_type_symbol
   _atom_site_fract_x
   _atom_site_fract_y
   _atom_site_fract_z
```

```
   _atom_site_occupancy
   _atom_site_adp_type
   _atom_site_U_iso_or_equiv
   _atom_site_symmetry_multiplicity
Ca1    Ca2+ 0.00000     0.00000     0.00000     0.999      Uiso 0.010      3
Mg1    Mg2+ 0.00000     0.00000     0.00000     0.001      Uiso 0.010      3
Ca2    Ca2+ 0.00000     0.00000     0.50000     0.003      Uiso 0.010      3
Mg2    Mg2+ 0.00000     0.00000     0.50000     0.998      Uiso 0.010      3
C1     C    0.00000     0.00000     0.24266     1.000      Uiso 0.005      6
O1     O2-  0.24762     -0.03535    0.24406     1.000      Uiso 0.015      18

loop_  _atom_type_symbol _atom_type_number_in_cell
  C    6
  Ca   3.004
  Mg   2.996
  O    18

# Note that Z affects _cell_formula_sum and _weight
_cell_formula_units_Z  6
_chemical_formula_sum  "C Ca0.501 Mg0.499 O3"
_chemical_formula_weight  92.21
```

Appendix 2 – Results of the elemental analysis

Analyte	B	Mg	Al	Ca	Fe	Mn	Ni
Detection Limits (DL)	0.1	0.5	0.1	10	7	0.02	0.01
Unit	ppb	ppb	ppb	ppb	ppb	ppb	ppb
Gf-1 918.2 m	3825	109615718	1918513	222552241	1340402	49921	6624
Gf-1 998 m	5798	132498707	1111339	220180741	945534	26655	32985
Gf-1 1055 m	3924	131174119	1536808	222149609	1440656	32666	6176
Gf-1 1109 m	6479	126518363	2963405	222487265	1818296	50013	18993
HH4	1253	126524356	385813	221349227	998252	53264	7404
HH2/1	1691	137494078	64234	222703514	233915	97706	5603
HH26	3276	129159443	2096779	226142824	942567	33321	5920
Mgy-1 253.8 m	3515	133616734	1023805	225544059	496007	15238	10701
Mgy-1 333.5 m	1367	117252034	1679876	228589763	671164	35406	6184
Mgy-1 346.9 m	2875	125520306	1379493	221063666	523766	34144	5642
Mgy-1 366.5 m	914	124099026	655652	228054580	362804	40697	5984
Mgy-1 381.5 m	671	122359910	688156	229887671	255929	22251	6080
VA 3T/1	2264	128057650	820633	222926629	790517	85205	5999
ZB-4	3808	128794805	1020926	222396485	364677	22465	5892
ZB-6	1877	138182319	353846	232890258	236650	21094	12139

Analyte	Zn	Rb	Sr	Ba	La	Ce	Pr
Detection Limits (DL)	0.05	0.03	0.01	0.01	0.01	0.01	0.01
Unit	ppb	ppb	ppb	ppb	ppb	ppb	ppb
Gf-1 918.2 m	6448	8609	98962	3905	1321	3412	462
Gf-1 998 m	5640	1666	100154	2811	1343	2907	350
Gf-1 1055 m	4257	2466	71522	3275	954	1794	212
Gf-1 1109 m	7667	8186	96168	7788	1511	3127	421
HH4	6022	198	53054	1413	300	417	78.7
HH2/1	19067	55.4	32244	364	437	409	84.3
HH26	10300	2343	65956	3267	1175	2680	323
Mgy-1 253.8 m	11428	1669	94347	2425	467	859	106
Mgy-1 333.5 m	7439	2607	113551	3314	1200	2294	280
Mgy-1 346.9 m	5459	2142	79664	2857	795	1507	195
Mgy-1 366.5 m	4848	599	69148	1205	376	450	70.5
Mgy-1 381.5 m	4846	312	82209	1488	832	638	131
VA 3T/1	15579	618	72319	1803	390	465	75.0
ZB-4	5451	771	73678	1711	359	713	86.6
ZB-6	3399	246	65921	1054	224	368	47.8

Analyte	**Nd**	**Sm**	**Eu**	**Gd**	**Tb**	**Dy**	**Ho**
Detection Limits (DL)	0.02	0.01	0.02	0.02	0.02	0.02	0.02
Unit	ppb	ppb	ppb	ppb	ppb	ppb	ppb
Gf-1 918.2 m	1853	388	67.0	362	48.9	242	44.4
Gf-1 998 m	1360	287	47.9	275	40.4	217	43.3
Gf-1 1055 m	800	157	28.3	159	22.4	128	25.4
Gf-1 1109 m	1688	350	65.9	358	50.5	265	51.2
HH4	336	76.6	18.1	89.4	14.4	90.6	19.3
HH2/1	322	64.4	13.0	72.4	11.2	63.5	14.0
HH26	1242	262	45.5	259	35.3	184	35.1
Mgy-1 253.8 m	411	85.6	16.4	88.0	12.6	70.7	13.9
Mgy-1 333.5 m	1095	224	41.1	220	31.0	159	30.1
Mgy-1 346.9 m	799	168	37.8	192	28.9	164	34.1
Mgy-1 366.5 m	291	59.5	13.5	82.3	13.2	91.7	21.2
Mgy-1 381.5 m	545	107	25.0	149	22.3	149	35.1
VA 3T/1	307	72.8	15.7	76.1	11.8	68.4	14.7
ZB-4	337	71.3	13.9	80.5	12.0	74.4	22.3
ZB-6	187	38.0	7.66	51.4	7.99	63.9	17.0

Analyte	**Er**	**Tm**	**Yb**	**Lu**	**Pb**	**Th**	**U**
Detection Limits (DL)	0.01	0.02	0.03	0.02	0.02	0.01	0.02
Unit	ppb	ppb	ppb	ppb	ppb	ppb	ppb
Gf-1 918.2 m	125	15.6	94.0	13.1	1553	875	422
Gf-1 998 m	134	17.5	108	16.1	1219	218	1596
Gf-1 1055 m	74.0	9.16	56.5	8.22	526	165	1441
Gf-1 1109 m	152	19.4	116	16.1	2139	658	2781
HH4	61.4	8.69	50.4	7.27	2274	57.8	306
HH2/1	43.0	5.90	39.6	5.91	4714	63.9	159
HH26	105	15.0	91.9	12.4	1638	672	1205
Mgy-1 253.8 m	45.5	6.25	38.0	5.57	1570	136	2755
Mgy-1 333.5 m	93.4	12.4	78.2	11.5	913	354	6163
Mgy-1 346.9 m	106	14.2	85.2	12.2	704	268	2263
Mgy-1 366.5 m	70.1	9.33	54.7	8.53	616	62.1	1436
Mgy-1 381.5 m	113	14.3	89.6	12.7	449	52.4	1156
VA 3T/1	45.2	6.35	33.7	5.29	1048	125	2530
ZB-4	80.4	10.7	61.1	8.22	406	95.8	1584
ZB-6	58.1	7.49	41.9	6.69	393	50.8	2378

VITA

Georgina Lukoczki

Candidate for the Degree of

Doctor of Philosophy

Thesis: GEOCHEMISTRY AND CRYSTAL STRUCTURE OF RECRYSTALLIZED DOLOMITES

Major Field: Geology

Biographical:

Education:

Completed the requirements for the Doctor of Philosophy in Geology at Oklahoma State University, Stillwater, Oklahoma in July, 2019.

Completed the requirements for the Master of Science in Geology/Geography at the University of Szeged, Szeged, Hungary in 2009.

Experience:

Graduate Teaching and Research Associate, Oklahoma State University, Stillwater, OK, USA (January 2016–July 2019).

Teaching Assistant, University of Alberta, Edmonton, AB, Canada (January–December 2015).

Visiting Researcher, University of Alberta, Edmonton, AB, Canada (February–December 2014).

Research Fellow, MTA-ELTE Geological, Geophysical and Space Science Research Group, Budapest, Hungary (August 2013–January 2014).

Research Assistant, University of Pécs, Pécs, Hungary (September 2012–July 2013).

Professional Memberships:

Geological Society of America (GSA), Society for Sedimentary Geology (SEPM), International Association of Sedimentologists (IAS), American Association of Petroleum Geologists (AAPG), Association for Women Geoscientists (AWG), Hungarian Geological Society (MFT).